Exploring astrophysics-relevant magnetohydrodynamics with pulsed-power laboratory facilities

S. V. Lebedev

Blackett Laboratory, Imperial College, London, SW7 2AZ, United Kingdom

A. Frank

Department of Physics and Astronomy, University of Rochester, Rochester, New York 14627, USA

D. D. Ryutov*

Lawrence Livermore National Laboratory, P.O. Box 808, Livermore, California 94551, USA

(published 25 April 2019)

Laboratory facilities employing high pulsed currents and voltages, and called generally "pulsed-power facilities," allow experimenters to produce a variety of hydrodynamical structures replicating, often in a scalable fashion, a broad range of dynamical astrophysical phenomena. Among these are astrophysical jets and outflows, astrophysical blast waves, magnetized radiatively dominated flows, and, more recently, aspects of simulated accretion disks. The magnetic field thought to play a significant role in most of the aforementioned objects is naturally present and controllable in pulsed-power environments. The size of the objects produced in pulsed-power experiments ranges from a centimeter to tens of centimeters, thereby allowing the use of a variety of diagnostic techniques. In a number of situations astrophysical morphologies can be replicated down to the finest structures. The configurations and their parameters are highly reproducible; one can vary them to isolate the most important phenomena and thereby help in developing astrophysical models. This approach has emerged as a useful tool in the quest to better understand magnetohydrodynamical effects in astronomical environments. The present review summarizes the progress made during the last decade and is designed to help readers identify and, perhaps, implement new experiments in this growing research area. Techniques used for the generation and characterization of the flows are described.

DOI: 10.1103/RevModPhys.91.025002

CONTENTS

I. INTRODUCTION

This Introduction starts with a brief discussion of the unique elements pulsed-power facilities bring to laboratory simulations of astrophysical magnetohydrodynamic phenomena. Especially impressive is a high degree of control of the flow parameters and resultant structures that can be achieved at these facilities. We then proceed to articulate specific examples of objects which have been or can be explored in pulsed-power settings. Finally, we address the interdependence

*Retired.

of observations, numerical simulations, and laboratory experiments in developing a better understanding of phenomena seen in the sky.

Hydrodynamical and magnetohydrodynamical (MHD) phenomena in astrophysics cover an enormous range of spatial and temporal scales. They are the basis for some of the most spectacular astronomical phenomena, such as supernovae (SN) shocks, accretion disks, and collimated jets. They sometimes occur on a relatively short time scale allowing for the direct detection of their variability. These dynamically evolving flows may be quite bright, thereby making possible the detection of quite intricate morphologies and fine details. This, in turn, helps in inferring the processes occurring at the sources of these flows, even if those sources are not directly resolvable. Magnetic fields are often detected in these objects or at least can be inferred from their morphology and dynamics. Despite an enormous diversity of morphologies and spatiotemporal scales, there is one point of commonality in many of these phenomena: they can be described by magnetohydrodynamics or by radiative magnetohydrodynamics.

It was realized decades ago that pulsed-power facilities offer a natural platform for the study of these phenomena in laboratory environments. By "pulsed power" we mean facilities where the plasma motion is triggered by high, short-pulse currents which drive the matter via the *j-cross-B* forces although sometimes motions can also be driven by the fast Joule heating of a sample or by a combination of the two processes. High magnetic fields are generated naturally and may become an integral part of the dynamical system.

The ability to generate flows with fields allows researchers to design laboratory experiments where flows that are morphologically similar to their astrophysical counterparts can be generated under controlled conditions and studied by a variety of diagnostic techniques. An expectation is that not only can morphology of astrophysical MHD flows be reproduced, but also one can detect effects that may be hard to resolve and identify in astrophysics. Examples of this would be the development of a small-scale turbulence or the appearance of non-MHD effects (such as the Hall effect). This general philosophy was earlier—and quite successfully—applied to the astrophysically relevant hydrodynamic experiments based on high-power lasers (Remington *et al.*, 1997; Kane *et al.*, 1997; Drake, 1999; Robey *et al.*, 2001). The first dedicated experiments with the pulsed-power facilities followed a few years later (Lebedev *et al.*, 2002).

In addition to the exploration of MHD processes, there are other applications of the pulsed-power devices that can benefit astrophysics. Because of their ability to develop high pressure in relatively large diagnosable volumes, pulsed-power devices are also used for studies of equations of state relevant to the planetary physics. The ability to generate very bright flashes of radiation has also been used for studies of opacities of various plasmas of interest for astrophysical systems (Rochau *et al.*, 2014; Bailey *et al.*, 2007, 2015; Knudson *et al.*, 2001, 2015). In what follows we, however, will focus on the MHD applications.

Pulsed-power devices are not the only platform suitable for the studies of astrophysical MHD: other platforms include high-power lasers and magnetic confinement facilities. Each of these platforms has its own advantages. Lasers are flexible and are capable to deliver enormous energy fluxes into small volumes. Pulsed-power systems are typically less expensive and allow for larger experimental volumes. Quasi-steady-state plasma devices produce even larger plasma volumes and allow researchers to naturally enter the regimes of low or negligible particle collisionality. This characterization is, of course, quite crude as there may be combinations of elements of more than one approach in a single experiment. We will describe some specific examples later.

In general, laboratory astrophysics based on a variety of experimental platforms has experienced explosive growth during the past decade, with several dozens of experimental papers appearing every year. We have chosen to summarize a subset of these results: the studies of astrophysics-relevant MHD with the pulsed-power facilities. By narrowing the scope, we gain the opportunity to provide more comprehensive analysis of this area of research which has developed its own efficient techniques for generating and diagnosing dynamical flows morphologically similar to their astrophysical counterparts.

One has to remember that a laboratory experiment can properly reproduce only a relatively narrow subset of processes affecting a particular astrophysical phenomenon. Still, if properly scaled, it provides a reliable test bed for validating numerical codes used in astrophysics, especially given that the experimenter can vary the input parameters and repeat an experiment many times. The main benefit to astrophysics is the capability of the laboratory experiments to reproduce the observed phenomena and thereby validate the conjectured underlying mechanisms.

A reader who might be interested in a broader view of laboratory astrophysics can benefit from an older comprehensive review (Remington, Drake, and Ryutov, 2006) that covers, in particular, the first steps in the use of one type of pulsed-power devices, the *Z* pinches. Another important publication is the review titled "The impact of recent advances in laboratory astrophysics on our understanding of the cosmos" (Savin *et al.*, 2012) that summarizes the state of the field as seen from the astrophysicist's perspective. There are also available two studies on the promises of the laboratory astrophysics that have been produced by community-based workshops (Prager *et al.*, 2010; Rosner and Hammer, 2010), where one can find some brief discussion of pulsed-power approaches to the problem. Broad reviews of the *Z*-pinch physics, technology, and applications can be found in Ryutov, Derzon, and Matzen (2000) and Haines (2011).

To provide the reader with some background regarding astrophysical flows that pulsed-power facilities have explored or are currently working on, we present several examples taken from the astrophysical literature; more details and references are provided in the later sections.

Figure 1 shows a jet generated by a young star. Such collimated supersonic streams of plasma driven from a central source are a common phenomenon in astrophysics. Most outflows and jets are thought to be generated near a central engine (e.g., a young, still forming star or a compact object such as a black hole) surrounded by an accretion disk. The experimental modeling of all ingredients of this process is still impossible, but significant features such as episodic events, intrajet clumps, the interaction with external medium, and

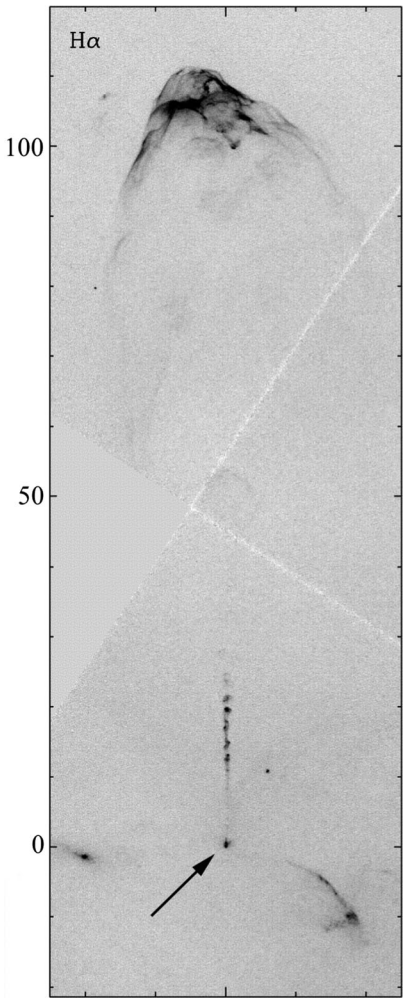

FIG. 1. A jet from a young star. The star situated inside the lowest knot (indicated by the arrow) is obscured by a compact reflection nebula. A knotty structure of the jet is obvious. Visible at the top of the figure is a bow shock produced by the interaction of the jet with the ambient medium. From Reipurth *et al.*, 2002.

other phenomena have been studied in a number of experiments (discussed in detail in Secs. II and III).

Creating an analog of the accretion disk (see Fig. 2) is a harder problem. The intrinsic difficulty here is the impossibility of reproducing the inward gravitational force that causes the disk material to spiral toward the central engine via various types of turbulent viscosity [Shakura and Sunyaev, 1973; Balbus and Hawley, 1991; see also Velikhov (1959)]. What is, however, possible in the lab is confining the rotating plasma from centrifugal radial expansion by maintaining the ram pressure of the incoming plasma flow. This configuration is discussed in Sec. IV.

A large segment of astrophysical MHD is related to the formation of shocks in supersonic and super-Alfvénic flows. In a number of cases the shocks may be of a collisionless nature (Sagdeev and Kennel, 1991). The shocks may also be strongly affected by radiative processes (Drake, 2006). Shocks, including radiative shocks, are discussed in Sec. V.

Thus far we considered single-fluid magnetohydrodynamics. This may become insufficient even at large scales

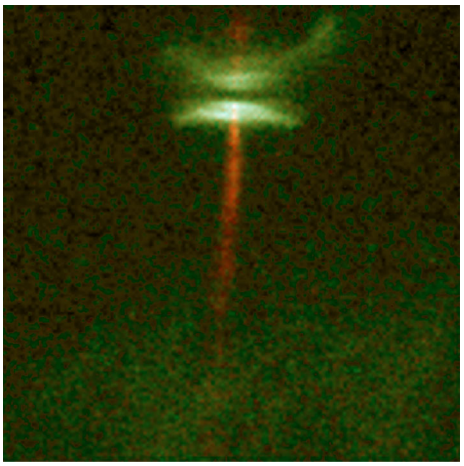

FIG. 2. Hubble Space Telescope image of HH-30 jet (NASA press release of June 6, 1995). An accretion disk observed edge on is seen at the top of the image as a dark band between its outer parts illuminated by the central star. The young stellar object is obscured by the densest part of the disk. From Madlener *et al.*, 2012.

compared to the particle mean-free path. In such cases one has to switch to two-fluid MHD that gives rise to new effects not covered by the "standard" MHD, in particular, to the Hall effect. The Hall effect may play a significant role in the evolution of astrophysical flows, in particular, in the jets (Königl, 2010) and in stellar flares and stellar winds (Mandt, Denton, and Drake, 1994). These issues are discussed in Sec. VI.

Another aspect of nonhydrodynamical effects is the formation of fast particles (high-energy beams and "hot" electron and ion populations). These effects may be important as an injection mechanism for further particle acceleration in cosmic rays. These phenomena lie beyond the boundaries of even a two-fluid hydrodynamics. Still, as high voltages formed in the disruptions of the current channels (see Fig. 3) may be triggered by hydrodynamic instabilities, we briefly discuss fast particles in Secs. III.B and VI.C.

Magnetic reconnection is one more phenomenon affecting dynamics of many astrophysical systems. Depending on the plasma parameters, it may occur via dissipative processes cascading down to the scales much shorter than the collisional mean-free path or via development of hydrodynamic turbulence (Yamada, Kulsrud, and Ji, 2010; Ryutov, 2015). In the high-energy-density environment of pulsed-power facilities, one can in principle access both regimes. We touch upon this possibility in Sec. VII.

An important issue in simulating astrophysical processes in laboratory experiments is the scalability between the two systems even though their spatial and temporal scales differ by many orders of magnitude. It turns out that the MHD equations allow for a broad class of similarities in situations where fluid viscosity and thermal conductivity are sufficiently low (Ryutov, Drake, and Remington, 2000). This occurs in a number of both astrophysical and laboratory settings. Importantly, shock waves are covered by this similarity. A different set of similarities covers aspects of two-fluid description and collisionless phenomena.

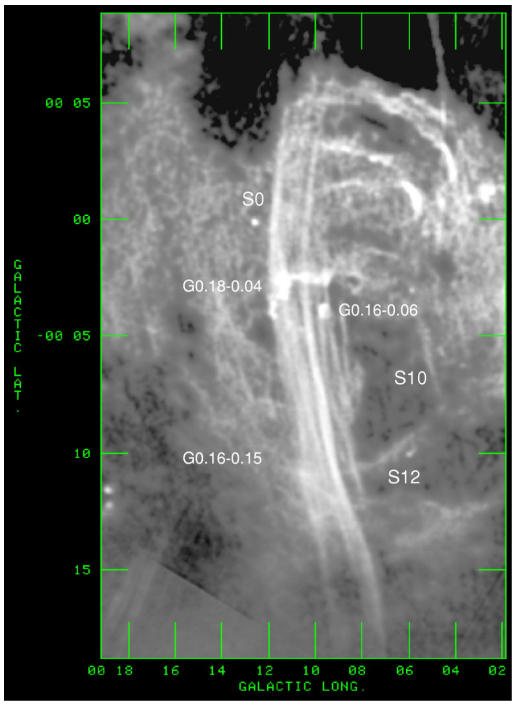

FIG. 3. The fine filamentary structures near the center of our galaxy consisting of a network of vertical filaments with lengths of about 30 pc (Yusef-Zadeh, Morris, and Chance, 1984, Yusef-Zadeh, Hewitt, and Cotton, 2004); it is speculated (Trubnikov, 1992) that those may be disrupting pinches leading to development of high voltages and particle acceleration. The image is taken by the NRAO Very Large Array at the wavelength of 20 cm.

In the Appendix we present a discussion of the similarity transformations and other conditions, which should be satisfied to allow meaningful connections between astrophysical and laboratory phenomena. It goes without saying that it is impossible to create in the lab a fully operating astrophysical object: laboratory experiments can model only a subset of a system for which such a representation is possible. Thus the successful design of the experimental system requires not only performing the scaling transformations, but also creating appropriate initial conditions and determining a time interval over which the scaling restrictions remain satisfied such that meaningful connections to astrophysical processes remain valid.

Experiments described in different sections of this review are at different stages of implementation of the outlined approach. Some of them are at relatively advanced stages, e.g., experiments with laboratory plasma jets (Secs. II and Sec. III), and it is possible to discuss the scaling correspondence between the laboratory and astrophysical phenomena. In other cases the experimental systems are still under development and a full scaling to a particular astrophysical system is not possible (e.g., experiments with rotating plasmas, Sec. IV). Experiments discussed in Secs. V–VII do not attempt to model particular systems, focusing instead on the physics of fundamental and astrophysically relevant processes such as shocks, non-MHD effects, and magnetic reconnection.

These experiments provide data for verification of numerical simulations of the processes. Codes tested in this way can then be reliably used to predict the behavior of an astrophysical system down to a certain scale established in a laboratory experiment.

In equations throughout the paper we use SI (mks) units, whereas in the tables and when presenting experimental data we use mixed units specified in each case.

II. JETS AND OUTFLOWS: WEAK MAGNETIC FIELD

Hydrodynamic jets with weak fields are an important class of astrophysical outflows. Special experimental techniques developed on pulsed-power facilities allow for a high degree of control over lab-scale jets suitable for exploring a variety of their astrophysical counterparts. Scalable experiments on the generation of highly collimated jets, their interaction with the side winds, and their collisions with dense gaseous clouds are described and related to astrophysical observations. Experimental techniques are briefly outlined.

A. Generating plasma streams and plasma jets with wire arrays

The generation of the astrophysically relevant jets was probably the most visible and important contribution of pulsed-power facilities to the laboratory studies of astrophysical MHD. An important part of these experiments was their capability to generate and control plasma flows by the use of so-called "wire arrays," which were initially developed for research in the areas of radiation sources and controlled fusion (Matzen *et al.*, 1999). In the simplest case, a "cylindrical array" is made of identical fine wires from a few microns to a few tens of microns in diameter, all parallel to the axis of the cylinder and distributed evenly over its circumference (i.e., an angle subtended by the two neighboring wires is $2\pi/N$ with N being the total number of wires). Such systems allow one to create a well-controlled initial state for fast Z pinches. They led to the controlled generation of intense pulses of soft and hard x rays. A general setup of the wire array experiment can be found in Matzen *et al.* (1999). Figure 4 represents a simple schematic.

An investigation of the early stage of the wire array implosion (Lebedev *et al.*, 1998, 1999, 2001; Aleksandrov *et al.*, 2016) has revealed that early in the current pulse plumes of plasma with a relatively low density are formed around each wire and begin to expand. This occurs prior to the onset of any radial motion of the wires themselves. This early stage of the discharge is illustrated by Fig. 5 (Lebedev *et al.*, 2001). Under the action of a global azimuthal magnetic field, the plasma plumes gain radial momentum, converging on the array axis well before significant motion of the wire cores begins. These separate streams merge somewhere halfway to the axis and form a continuous converging flow. A high resistivity of wire cores means that they do not carry a significant current and remain at their original positions, while the majority of the current concentrates on a layer of plasma surrounding the cores. This plasma layer is continuously replenished by the material ablated from the wire cores providing a long-lasting injection of ablated plasma streams accelerated toward the array center by the $J \times B$ force. The converging cylindrical plasma flow carries some axial current and, therefore, an azimuthal magnetic field. For sufficiently small azimuthal

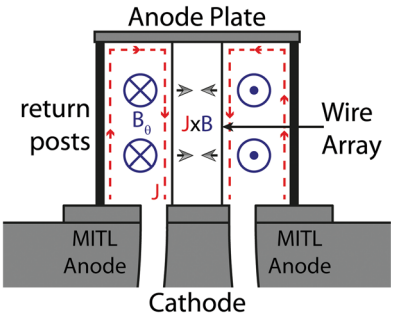

FIG. 4. Schematic of a wire array Z pinch. The cylindrical array of wires is fed through the gap at the bottom of the figure by the current supplied via the pulse-power generator (not shown). The current flows along the wire array (the position of which is shown by arrow) and through an outer cylinder, usually having holes for diagnostic access or made of separate return current posts. An azimuthal magnetic field present outside the array pushes it inward. In the fusion and radiation applications, implosion of the array leads to a short pulse of extremely high pressure. For the applications considered in this review, the main focus is the early stage of the pulse when the wires have just started moving toward the axis. From M. J. Bennett.

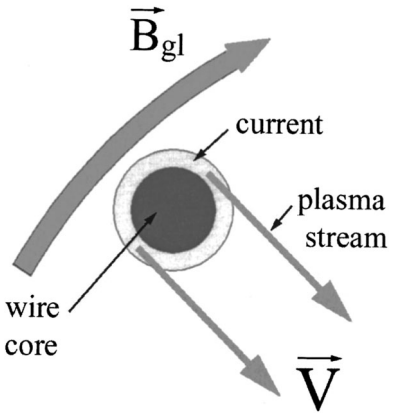

FIG. 5. Formation of a plume of plasma around a wire core (a white annulus around the dark circle). The global magnetic field vector B_{gl} is shown by the gray curved arrow. Interaction of an axial current in the plume with the global magnetic field causes acceleration of the light plume material toward the center. At some distance from the wires, the plumes merge to form a continuous flow carrying some axial current. From Lebedev *et al.*, 2001.

separations between the wires the azimuthal inhomogeneities smooth out at some distance inward from the wire cores, and we get a converging cylindrical plasma stream that is typically supersonic and superalfvenic. It is this smooth radial flow that served as a basis for a number of experiments described in this review, in particular, in Secs. II, III.A, IV, V, and VII. Other techniques for producing plasma flows suitable for the studies of the astrophysical MHD phenomena are described in Secs. III.E, V.B, and VI.

As an aside, one can mention that formation of the plasma flow propagating inward still allowed for the production of high-quality wire array implosions used in the applied (fusion, radiation sources) research (Cuneo *et al.*, 2006). The current per wire in these experiments was in the range from 1 kA to tens of kA, with the rise time of ~100 ns.

The use of the wire arrays allows one to create a diverging plasma flow by putting the reverse current conductor on the axis of a wire array as shown in Fig. 6 (Harvey-Thompson *et al.*, 2009). This produced an expanding plasma shell outside the wire array. Such a configuration facilitates an access to the experimental zone, which is now situated outside the wire array.

Returning to the generation of plasma jets, we describe the corresponding experimental configuration (Lebedev *et al.*, 2002), which is illustrated in Fig. 7. Here we have not a cylindrical, but a conical wire array, with the apex half angle of 15°–30°. Accordingly, after the pinch current is turned on, the plasma flow (that moves normal to the array surface) converges on the array axis. The plasma is highly collisional (see Table II), and the process has to be described as a hydrodynamic phenomenon. As the radial (toward the axis) component of the velocity is highly supersonic, a conical shock forms near the axis, which will redirect the flow momentum in the axial direction (a hydrodynamical "shaped-charge effect" (Walters, 1998). Such conical shocks are not a stranger to the astrophysical world. The role of these kinds of shock structures has been discussed, e.g., by Canto, Tenorio-Tagle, and Rozyczka (1988), with the possibility of young stellar object (YSO) jet formation by converging conical shock. In addition, Frank, Balick, and Livio (1996) used conically converging flows in the environment of stellar wind-blown bubbles to create highly collimated flows. In both cases conical flows were explored as a jet formation mechanism years before laboratory experiments were carried out. In the laboratory, dense, strongly radiating jets have also been produced by the irradiation of the inner surface of

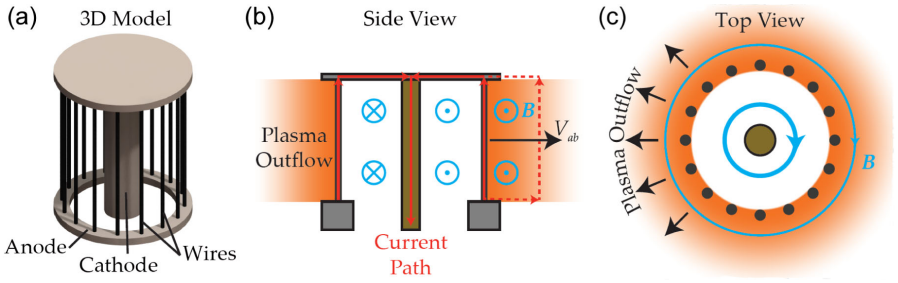

FIG. 6. Inverse wire array: (a) 3D schematic, (b), (c) side-on and end-on cross sections, respectively. The current comes from the bottom, flows upward along the wires of the array (16 in this case), and comes back through a central post (gray). Diverging cylindrical plasma flow is created due to magnetic pressure acting on the plumes in the outward direction. From J. Hare.

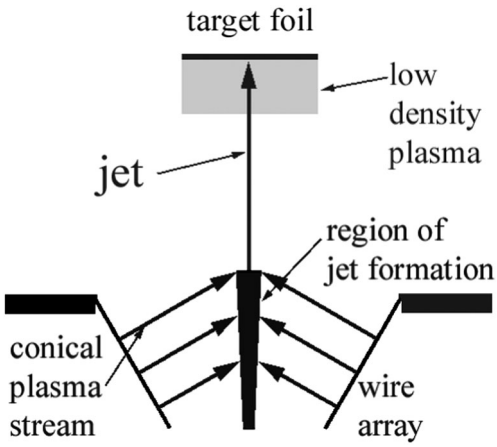

FIG. 7. Generation of the jet in a conical wire array. From Lebedev *et al.*, 2002.

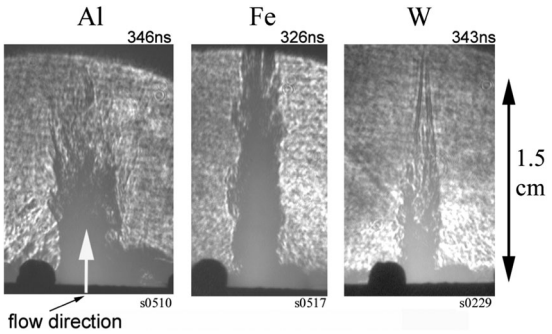

FIG. 8. Laser probing images of plasma jets formed in aluminum, stainless steel, and tungsten wire arrays show that the degree of collimation increases for elements with higher atomic number in which the radiative cooling is higher. From Lebedev *et al.*, 2002.

conical targets by high-power lasers by Farley *et al.* (1999) at the NOVA laser facility (Campbell, 1991) and by Shigemori *et al.* (2000) at the GEKKO-XII laser facility (Yamanaka *et al.*, 1981).

The dense plasma formed near the axis in the configuration of Fig. 7 has significant axial momentum and may be additionally accelerated by the pressure gradient in the axial direction. As a result, a well-collimated plasma jet emerges from the cone. Note that the wires in this scenario serve only as a source of plasma for jet generation and do not significantly participate in the motion (they remain too heavy to be accelerated).

This configuration and its variations allowed the experimenters to produce a broad range of astrophysics-relevant hydrodynamic objects: highly radiative weakly diverging jets, jets propagating through an external medium including emulation of a "side wind," rotating jets, simulated accretion disks, and other applications. The corresponding results are discussed in Secs. II.B, II.C, and IV. In the next section we describe the use of the just described techniques for the studies of some aspects of the physics relevant to the YSO jets.

B. Hypersonic, radiatively cooled hydrodynamic jets and their interaction with an ambient medium

The configuration of a conical wire array shown in Fig. 7 led to the most astrophysically relevant set of jet experiments from the early stage of the laboratory pulsed-power astrophysics research. In this way they served as an early model for what was possible with high-energy-density laboratory astrophysics. The first experiments with conical wire arrays (Lebedev *et al.*, 2002) have indeed shown the relevance of such jets to astrophysical problems, in particular, to the outflows from young stars which have comparable Mach numbers and radiative cooling parameters. Several wire materials were used in these experiments: tungsten, stainless steel, and aluminum. The wire diameters were 25, 25, and 18 μm, respectively. The number of wires was 16 with a bottom radius of the array set at 8 mm, and an opening angle of the wires at 30°. The length of the array was 1 cm. The velocity of the jet was measured via laser probing diagnostics and was found to be ∼150 km/s.

The structure of these jets is shown in Fig. 8 borrowed from Lebedev *et al.* (2002). The parameters of the jet beyond the upper surface of the array are either measured directly (Lebedev *et al.*, 2002) or inferred from numerical simulations matching the experiment (Ciardi *et al.*, 2002) and are presented in Table I; some of the most important derived parameters are presented in Tables II and III.

Note that the experiments achieve a remarkably high Reynolds number. The other dimensionless parameters Re_M and Pe also significantly exceed the unity. This provides a reasonable degree of confidence that the hydrodynamical phenomena occurring in this laboratory-generated jet will correctly replicate the same phenomena in hydrodynamical astrophysical jets, despite an enormous difference in the scales.

One of the most distinctive features of the YSO jets is their high degree of collimation with the length-to-radius ratios as high as 10 to 20. In addition the astrophysical flows are characterized by high Mach numbers of $M \sim 10$–20. It is thought that such divergence and high values of M are related to the fast radiative cooling of the jets (Blondin, Fryxell, and Konigl, 1990; Stone and Norman, 1993a, 1993b). The observed trend in the divergence of the laboratory-made jets versus the jet material supports this viewpoint: the tungsten jet is much better collimated than the aluminum jet. The same trend was found in the earlier laser-driven experiments (Farley *et al.*, 1999; Shigemori *et al.*, 2000).

Two-dimensional (r-z) simulations automatically produced azimuthally symmetric outflows due to their imposed azimuthal symmetry. In experiments the converging plasma flow inside the conical array was initially strongly modulated in the azimuthal direction due to the relatively small number of wires used (typically 16, sometimes as few as 8). Nevertheless it was observed that the jets had very good azimuthal symmetry at the exit from the array, which allowed concluding that formation of jet via converging conical flows is stable to the azimuthal perturbations. Note that this was a conclusion that could not be reached from traditional astrophysical studies alone. The characteristic cooling length in the

TABLE I. Measured and inferred parameters of the tungsten plasma formed in conical arrays: n_e (electron density); T (common value of the electron and ion temperatures), Z (average ion charge), a (jet radius at the upper surface of the wire array), S (sound speed in the jet plasma), V (jet velocity at the exit from the array), and L_C (cooling length, estimated from soft x-ray emission decay along the jet).

n_e	T[a]	a	Z[a]	S	V	L_C
10^{19} cm^{-3}	50 eV	1.5 mm	10	5×10^6 cm/s	$(1.5–2)\times10^7$ cm/s	0.3 cm

[a]Parameters inferred from numerical simulations.

TABLE II. Derived parameters: λ_{ei}, λ_{ii} electron-ion (ion-ion) collision length; ν ion kinematic viscosity; D_M magnetic diffusivity; χ_{therm} electron thermal diffusivity; and B_0 the magnetic field strength at which the plasma beta evaluated for the thermal pressure would become dynamically significant $\beta = 2\mu_0 p/B_0^2 = 1$.

λ_{ei}	λ_{ii}	ν	D_M	χ_{therm}	B_0
0.1 μm	0.1 μm	60 cm^2/s	10^5 cm^2/s	4×10^3 cm^2/s	15 T

TABLE III. Main dimensionless parameters: $\mathrm{Re} = aV/\nu$, $\mathrm{Re}_M = aV/D_M$, $\mathrm{Pe} = aV/\chi_{therm}$, and L/L_C

Re	Re_M	Pe	L/L_C
3×10^4	20	500	2–7

experiments was estimated from the measurements of the soft x-ray emission decay along the jet.

With regard to the magnetic field strength, it was not measured directly in these early experiments, but one could get an upper bound for it by noting that the jet did not show development of a pinch instability. The absence of this potent instability in a system perfectly describable by MHD could be interpreted as a magnetic pressure that was smaller than the plasma pressure, yielding an estimate presented in Table II. In subsequent experiments the magnetic field was measured directly, yielding the value of a few T, i.e., well below the upper bound given in the rightmost column of Table II and, correspondingly, not playing a significant dynamical role. We note that in astrophysical jets the magnetic fields appear to become less important at large distances from the region of collimation (Hartigan *et al.*, 2007).

C. Hydrodynamic interaction of the jets with a side wind

The jets previously described were truly hydrodynamic in that their plasmas were highly collisional and showed no significant effects due to magnetic fields. In a subsequent series of experiments such jets created by conical arrays were used to study the interaction of hydrodynamical stellar outflows with plasma clouds encountered during their propagation. To generate a miniature analog of such a cloud, a plastic foil was placed at some distance from the jets axis, at an oblique angle, as shown in Fig. 9(a). Extreme ultraviolet (XUV) emission from the standing conical shock and individual wires of the array interacted with the foil and led to the formation of a plasma flow (plasma wind) crossing the path of the jet (Lebedev *et al.*, 2004, 2005a; Ampleford *et al.*, 2007).

This setup mimics the interaction of the YSO jet with a cross wind, a process that is thought to be responsible for the formation of the C-shaped YSO jets, whose observations are summarized by Reipurth and Bally (2001). While there had been a number of analytic and simulation studies (Raga *et al.*, 2002) of these jet-wind interactions (relevant to the HH110 system) , the pulsed-power studies described next allowed for theory to be directly compared with controlled experimental studies for the first time.

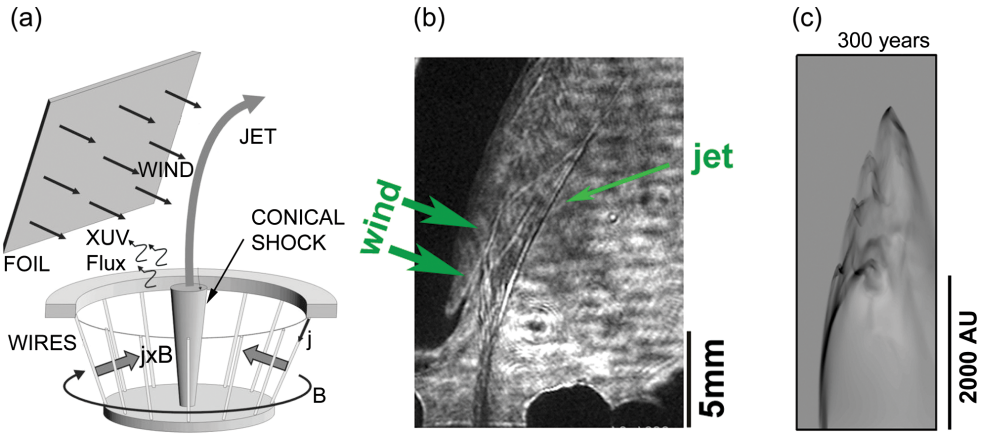

FIG. 9. (a) Schematic of the jet formation in a conical wire array and a side wind generation by surface plasma expansion from the plastic panel. (b) Time-resolved laser schlieren image of the jet bending (340 ns after the start of the current); the capability of resolving fine features of the interaction zone makes this platform attractive for selecting the most plausible scenarios of analogous effects in astrophysics. (c) The line-integrated density structure in the jet termination area obtained in numerical simulations of an astrophysical jet. Adapted from Ciardi *et al.*, 2008.

TABLE IV. Parameters of the jet and cross wind in experiments. From Lebedev *et al.*, 2004.

Area	Density ($g\,cm^{-3}$)	Velocity ($cm\,s^{-1}$)	T (eV)	Z
Jet	$\sim 10^{-4}$ [a]	$(10–20)\times 10^6$	<50	5–10
Wind	$\sim 10^{-5}$ [b]	$(2.5-5.5)\times 10^6$ [c]	Unknown	1–2

[a]At $n_e \sim 5\times 10^{18}$ cm^{-3}, $A = 183$, and $Z = 10$.
[b]At $n_e \sim 10^{18}$ cm^{-3}, $A = 6$, and $Z = 1$.
[c]The velocity of the cross wind was determined from the measured delays in the start of the jet-wind interaction, observed for different separations between the foil position and the jet axis

In the experiment, the presence of the cross wind was shown to cause deflection (bending) of the jet. The jet trajectory or shape was measured using laser probing and XUV self-emission images, and the densities of the jet and the ambient plasma (wind density) were measured by the interferometry. The wind velocity was only estimated, but not directly measured in these experiments. The observed behavior of the jet, its modified trajectory, was then interpreted using results of numerical modeling in which the plasma wind velocity was adjusted to fit the jet trajectory. The typical numbers for the jet (V) and wind (V_w) velocities as well as their densities are given in Table IV.

The same density and velocity ratios as well as the jet Mach number were then used to model the bending of *astrophysical* jets by the same mechanism. Simulations (Ciardi *et al.*, 2008) in addition to reproducing the overall trajectory similar to those predicted by the analytical model of Canto and Raga (1995) showed that the interaction also leads to formation of density perturbations (i.e., knots) in the jet. It is important to emphasize that in the simulations both the jet and the wind are initially uniform and smooth, and the perturbations (knots) arise from the development of the combination of Rayleigh-Taylor and Kelvin-Helmholtz instabilities. The duration of the laboratory jet interaction was insufficient to see such a development in the early experiments. Simulations also assessed effects of jet rotation on the morphology of the interaction, suggesting that there could be some observable differences.

Another common astrophysical configuration is represented by a jet plowing into a stationary gaseous cloud (see, e.g., Fig. 1). This occurs in star forming environments when a jet penetrates denser regions of its natal molecular cloud and in galactic-scale jets when they propagate through the clumpy media surrounding the central supermassive black hole. To explore these phenomena in the laboratory, Ampleford *et al.* (2005) and Suzuki-Vidal *et al.* (2012) formed the ambient medium using a cloud of neutral gas positioned on the path of the jet. The cloud was typically formed using a supersonic gas nozzle. The velocity of the gas flow was, however, significantly smaller than the jet velocity so the gas cloud could be considered as a stationary mass distribution. In this way astrophysically relevant ratios of jet and ambient densities were produced. For laser-based experiments on the interaction of jets with an ambient medium see Foster *et al.* (2005) and Nicolaï *et al.* (2008).

In some of the experiments the gas cloud had a relatively sharp boundary allowing direct study of the interaction of the jet crossing a density discontinuity. Ampleford *et al.* (2005) observed that the interaction produced a broad bow shock (Fig. 10). The overall dynamics of the working surface (Blondin, Fryxell, and Konigl, 1990) formed at the head of the jet interacting with the gas cloud was in reasonable agreement with the standard expressions describing its dependence on the density ratio. In addition, experiments show development of asymmetries in the shape of the bow shock, and, in particular, a transverse displacement of the brightest regions of the working surface with time. One possible explanation is the presence of an advected B field in the jets and in the plasma surrounding the jet. The ionization of the gas cloud by the XUV radiation could lead to the formation of a new, asymmetric path for the current, which could lead to the appearance of unbalanced $J \times B$ force slowly displacing the jet.

D. Highly collimated jets produced by ablation of the central area of a metal foil

This approach is based on the configuration where the central cathode post is connected with the surrounding cylindrical return current conductor by a thin, vacuum-tight planar metal foil, as shown in Fig. 11. The attractiveness of this technique is related, in particular, to the fact that it allows one to create a setting where the jet is interacting with an

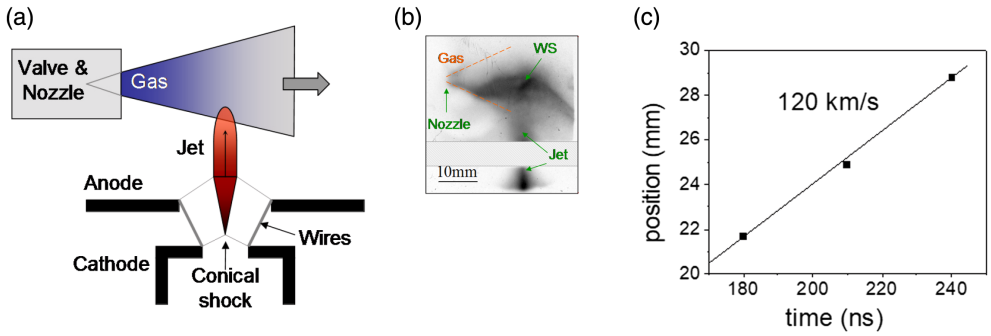

FIG. 10. (a) Schematic of the experiment in which a radiatively cooled plasma jet interacts with a gas cloud. On the time scale of the plasma jet propagation, the gas cloud can be considered stationary. (b) Self-emission image of a plasma jet (formed from stainless steel wires) interacting with an argon gas cloud. The position of the working surface (marked as WS) seen as a region of enhanced emission at the head of the jet is labeled in (b). Velocity of the working surface graphed in (c) is 2 times smaller than the jet velocity in the absence of the gas cloud, consistent with the jet-ambient density contrast of $\eta \sim 1$. Adapted from Ampleford *et al.*, 2005.

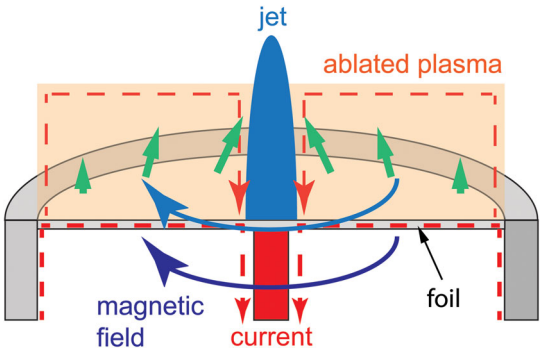

FIG. 11. Schematic of a thermal mechanism of the jet generation on the planar metal foil. A "distributed" magnetic field structure is formed due to advection of the magnetic field diffusing through the resistively heated foil. Ablation, strongest near the axis, combined with the magnetic hoop force, leads to the formation of a dense jet surrounded by a lower-density plasma flowing upward. From F. Suzuki-Vidal.

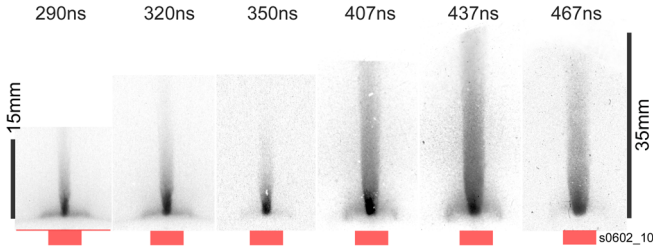

FIG. 12. XUV self-emission images of a jet from a radial foil propagating in vacuum. The images were obtained during the same experiment and times are relative to the start of the current. Position and diameter of the cathode are shown below the jet images, including the initial position of foil in the first image. The jet starts ∼1.5 mm above the initial foil position due to expansion of the central part of the heated foil. From Suzuki-Vidal *et al.*, 2012.

ambient medium from the very beginning of the jet formation. This allows one to address an important issue of the effect of the ambient medium on the formation and propagation of the astrophysical jets. This question is particularly important as conditions in the medium surrounding an astrophysical jet may not be directly probed by observations so that the medium's conditions (and collimating pressure) may not be directly inferred.

In the experiments the jet is formed because the radial current flowing through the foil between the central post and external cylindrical return current conductor is heating the foil predominantly near the center due to the radial divergence of the current flow. Therefore, intense heating of the foil occurs only near the center, and the ablated plasma column turned out to be highly collimated. This technique was used by Suzuki-Vidal *et al.* (2012).

We start from the situation where the ambient gas density above the foil is negligible, and the ablated plasma expands into "empty space." Even in this case, some lower-density plasma appears outside the dense central jet due to the heating and ablation of the foil. This "halo" plasma has density a factor of ∼10 smaller than that in the central jet but moves with the same axial velocity.

These and related (Suzuki-Vidal *et al.*, 2012, 2013a) experiments produced jets with a very high degree of collimation: an opening angle of 2°–5° is sustained over the distance exceeding the jet radius by a factor of >10, with a sharp density contrast at the boundary between the jet body and the halo plasma; see Fig. 12. The internal Mach number in these experiments was measured by a Thomson scattering (TS) diagnostic: the Doppler shift of the ion feature provided jet velocity. Spectral broadening provided measurements of ZT_e and thus the ion sound speed. From these measurements the Mach number was determined to be only ∼2.5, too small to explain the observed very small divergence of the jet (a 3° opening angle would require $M \sim 20$).

Explanation of this discrepancy came from MHD simulations (Suzuki-Vidal *et al.*, 2012), which suggest that the halo plasma surrounding the jet carries some level of frozen-in toroidal magnetic field, with the current path responsible for this field closing at the boundary of the halo plasma. The pinch force associated with this B field produced the inward convergence of the halo plasma. The collimation of the central, dense part of the jet was provided by the ram pressure of this converging flow. What is remarkable in this setup is that this is essentially a magnetic collimation of the outflow by the "distributed" magnetic field structure. It provides strong collimation but does not destroy the jet stability. In these experiments the maximum observed jet length (≈45 mm with a length-to-radius ratio >20) was determined by the duration of the current pulse driving the plasma ablation from the foil, which allowed the jet to propagate distances exceeding the radius of the plasma emitting foil by a factor of 2. The question of how much longer the steady, stable propagation of the jet is possible in this setup has not been investigated as yet.

As mentioned earlier, the setup with the use of radial foil provided more flexibility for adding ambient media for jet-plasma interactions, in particular, allowing creating a uniform distribution of the neutral gas above the foil. In this case the interaction remains azimuthally symmetric with formation of a bow shock ahead of the central jet.

As shown in Fig. 13, two distinct features are formed (Suzuki-Vidal *et al.*, 2012). First there is a curved shock, gradually becoming a conical shock and driven into argon prefill by the lower-density halo plasma. The shock position is determined by the radial profile of ram pressure in the flow and the temporal delay in the plasma formation at the foil (plasma forms earlier at smaller radius as it is driven by a higher-current density of the radial current).

Second, the bow shock is developing above the central jet from ∼300 ns and can be seen above the conical ablation shock in the last five images of Fig. 13(a). This is also illustrated by Fig. 15(a), where the tops of the last three images of Fig. 13(a) are shown with higher magnification. Figure 15(b) shows the images for a different shot—the similarity of the two rows shows the robustness of this feature. The bow shock is driven by the faster axial velocity of the plasma ejected by the high pressure created at the top of the central jet.

This experiment was modeled with the GORGON 3D resistive MHD code (Chittenden *et al.*, 2004; Ciardi *et al.*, 2007), with the simulations accounting for the radiative cooling of the plasma. As can be seen from Fig. 13(b), which

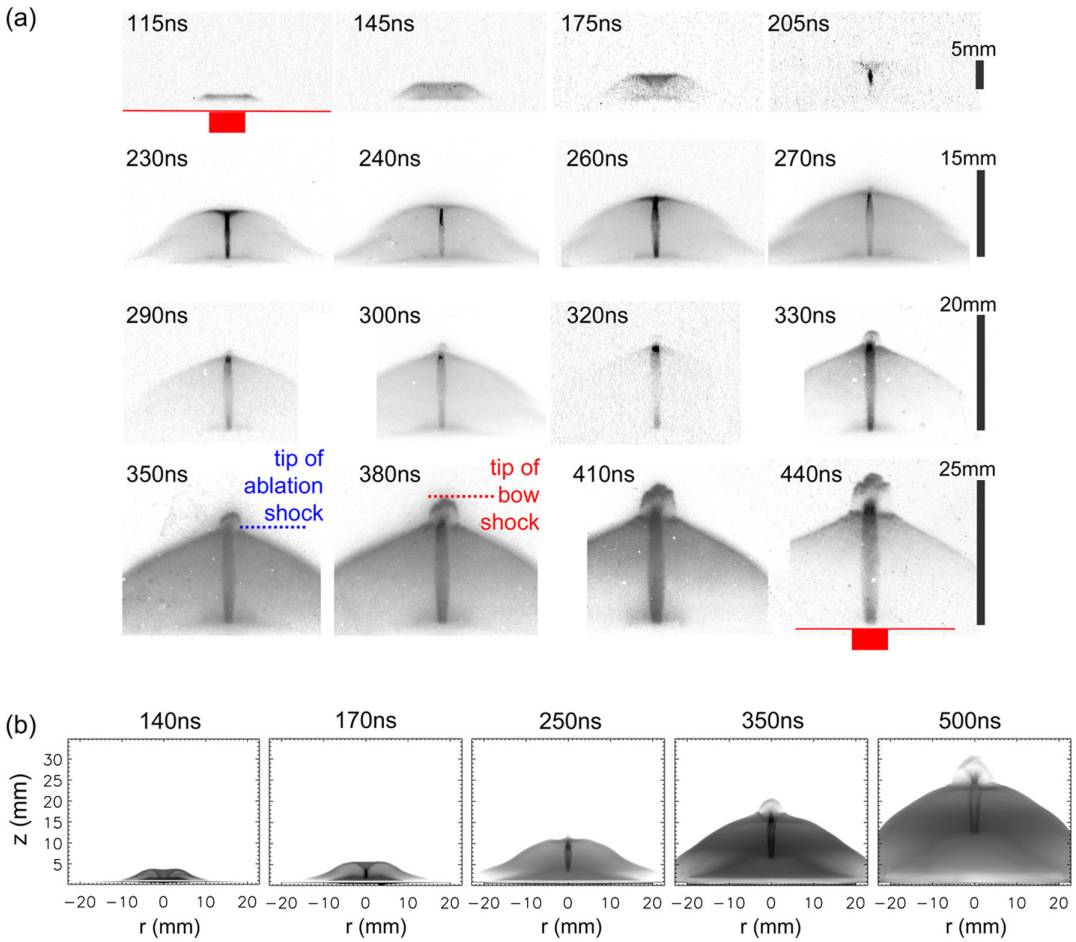

FIG. 13. (a) Sequences of XUV self-emission images of a jet generated via an aluminum foil and propagating in argon, showing the formation and evolution of the jet together with the formation of two distinctive shock features: an "ablation shock" formed at early times, followed by the later formation of a "bow shock" seen above ablation shock from ~300 ns. The diameter and position of the cathode and the foil are shown on the first and last frames. (b) MHD simulations of the experiment reproduce the main features of the jet formation and evolution (synthetic XUV images). From Suzuki-Vidal *et al.*, 2012.

shows synthetic XUV emission images, the simulations were able to reproduce all of the main features of the evolution of the system. Maps of the force densities and the stream lines of the plasma flow (Fig. 14) show that collimation of the central jet is provided by the converging plasma streams: the plasma ablated from the foil is redirected toward the axis by the radial component of the $J \times B$ force.[1] The motion of the interface between the ambient gas and foil material [the "ablation shock" indicated in Fig. 13(a)] is also magnetically driven, by the $J \times B$ force provided by the toroidal magnetic field and current flowing along the ablation shock surface.

The simulations also suggest that the bow shock seen in Fig. 13 is formed due to an increase in pressure at the tip of the ablation shock. This is driven to a large extent by the enhanced toroidal magnetic field in this region, forming a structure resembling a nozzle. The bow shock driven by the fast plasma flow develops a number of regular, larger-scale structures with the size comparable to the bow shock radius. It is interesting to note that very similar structures were recently observed in numerical simulations of the astrophysical bow shocks (Hansen *et al.*, 2017), where they were interpreted as due to the development of thin-shell instability advected along the bow shock. Similar structures of bow shocks were also seen in computational studies of radiatively cooled astrophysical jets [see, e.g., Fig. 5 in Blondin, Fryxell, and Konigl (1990)].

In addition to these large scale features, the experiments also show the development of small-scale perturbation at the bow shock surface. The structure is best observed using laser probing in a shadowgraphy setup [Fig. 15(c)], as this diagnostic is sensitive to the gradients of the refractive index (plasma density). Note that the image in Fig. 15(c) provides a high resolution view of the jet's fine details and can admit the use of correlation analyses and a full parameter study to be compared with the numerical runs. Similar fine details develop in astrophysical jets [see, e.g., Fig. 17 in Hartigan *et al.* (2011)] although in the lab we have the privilege of being able to control their development via manipulation of external parameters. The most probable reason for the

[1]Simulations shown in Fig. 14 correspond to the case when a low density ambient gas was added above the foil, but the same mechanism of jet collimation was observed in simulations of jet formation in the absence of the ambient material: in both cases the pinching azimuthal magnetic field was located in the material ablated from the foil.

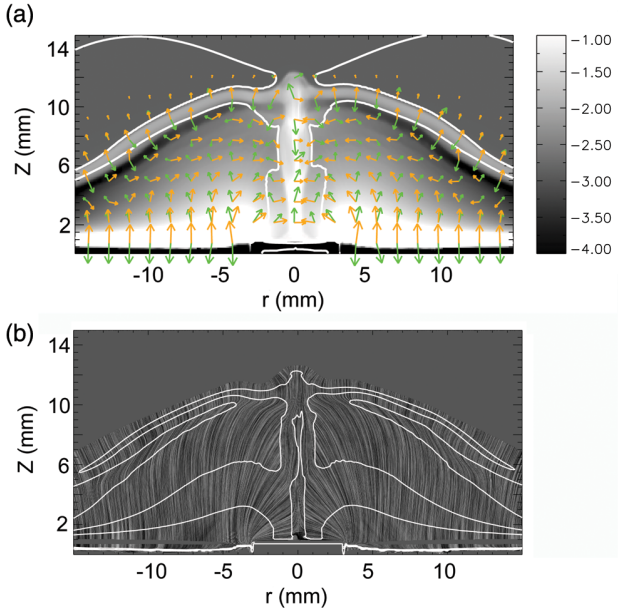

FIG. 14. MHD simulations of a jet from a radial foil propagating through argon ambient gas. (a) The background shows mass density (in logarithmic scale, in units of kg/m^3). Superimposed are contours of plasma $\beta = 1$. The arrows represent force densities in the plasma, $J \times B$ (green) and pressure gradient (orange). (b) Flow stream lines showing the direction of the plasma flow and contour lines of constant density [with values −4, −2, and −1 of scale shown in (a)]. From Suzuki-Vidal *et al.*, 2012.

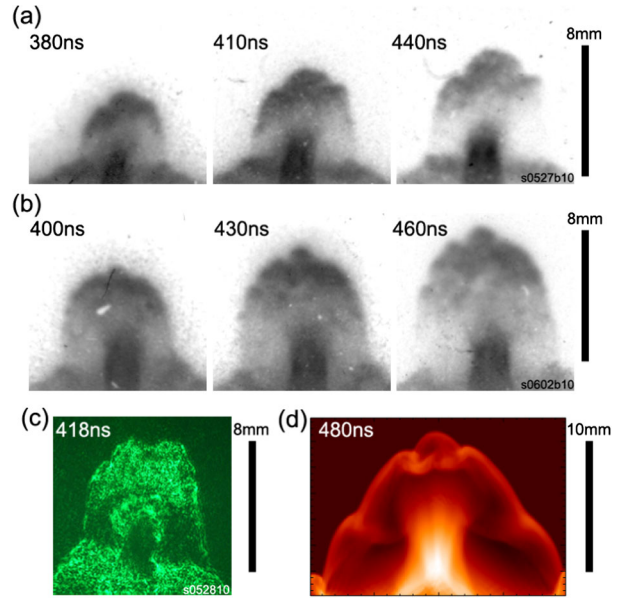

FIG. 15. (a), (b) XUV emission of the bow shock ahead of the jet from two experiments. The images show the formation of spatial features at the front of the shock. Both images are centered on the strongly emitting region at the tip of the jet. (c) Dark-field laser schlieren image showing the presence of small-scale structures inside the shock. (d) Simulation results showing the formation of spatial features at the front of the shock. From Suzuki-Vidal *et al.*, 2012.

development of these structures is the presence of strong radiative cooling. The characteristic spatial scale seen in the experiment is close to the calculated cooling length.

Comparison of the observed and simulated structures in Figs. 15(c) and 15(d) shows that, although the simulations reproduce the overall structure of the bow shock quite well, they do not show the presence of much smaller, ∼200 μm scale perturbations seen in the experimental images. The absence of such structures in the simulations comes from the insufficient spatial resolution (100 μm) in this global simulation which included modeling of the whole experimental system (50 mm diameter, 30 mm height). This example illustrates the potential for experimental systems to model significantly larger ranges of spatial scales than a global numerical model can since numerical diffusion at the grid level effectively reduces the "numerical" Re, Pe, and Re_M numbers to values much smaller than those determined by the physical parameters of the system.

In conclusion, the use of pulsed-power machines allowed for production supersonic, collimated plasma flows with weak magnetic field applicable to studies of hydrodynamic aspects of astrophysical jets. The relevance of these laboratory plasma jets to their astrophysical counterparts, in particular, to stellar jets at distances far from the central star, is based on the similarity of the relevant dimensionless parameters determining their dynamics. This is illustrated by Table V, which compares typical dimensionless parameters characterizing astrophysical stellar jets and laboratory plasma jets described in this section (see the Appendix for a discussion of the scaling issues).

Table V shows that the Re, Re_M, and Pe numbers are all much greater than unity, which means that both systems are well described by the equations of ideal MHD and the effects of viscosity, diffusion of magnetic field, and thermal conduction are negligible on the global scale L. The noticeable differences in the values of these parameters mean that the

TABLE V. Comparison of typical dimensionless parameters characterizing astrophysical stellar jets and laboratory plasma jets described in this section.

Parameter	Stellar jets	Laboratory jets
Reynolds number Re	$>10^8$	10^{5}[a]
Magnetic Reynolds number Re_M	$>10^{15}$	50–500[a]
Peclet number Pe	$>10^7$	20–500[a]
Mach number M	2[b]–20	2–10
Density contrast $\eta = \rho_{\mathrm{jet}}/\rho_{\mathrm{ambient}}$	0.1–10	1–10
Cooling parameter $\chi = \tau_{\mathrm{cool}}/\tau_{\mathrm{dyn}}$	0.1	0.1–0.001
Spatial scale[c]	15 000 AU	10 mm
Relation between time scales [d] $t_{\mathrm{Ast}} = t_{\mathrm{Lab}}(L_{\mathrm{Ast}}/L_{\mathrm{Lab}})(V_{\mathrm{Lab}}/V_{\mathrm{Ast}})$	700 yr	200 ns

[a]Effective values of Re, Re_M, and Pe numbers for global 3D simulations, determined by discretization in numerical schemes, are $\mathrm{Re} \sim \mathrm{Re}_M \sim \mathrm{Pe} \sim 10^3$.

[b]A smaller value of Mach number corresponds to internal shocks in the jets [see, e.g., Hartigan *et al.* (2011)].

[c]Characteristic sizes of bow shocks shown in Fig. 1 for HH34 object and in Fig. 15 for laboratory experiment.

[d]Using the spatial scales for $L_{\mathrm{Ast}} = 15\,000$ AU; $L_{\mathrm{Lab}} = 10$ mm, and $V_{\mathrm{Ast}} = 200$ km/s, $V_{\mathrm{Lab}} = 100$ km/s

ideal MHD description becomes invalid at different relative spatial scales δ/L, which are, however, much smaller than the global scales of the systems $\delta/L \ll 1$.

Consider two examples: (1) For a model of the Rayleigh-Taylor instability on the background of a smooth density variation with the scale $L \equiv \rho/|\nabla\rho|$, the viscous effects are small for the scales $\delta/L > \mathrm{Re}^{-1/2}$ (Ryutov *et al.*, 1999). (2) For the Kelvin-Helmholtz (KH) instability of sheared flow, with a scale L of velocity variation, viscosity is negligible for the perturbations with the scale $\delta/L > (\mathrm{Re}/\mathrm{Re}_{\mathrm{crit}})^{-3/4}$, where $\mathrm{Re}_{\mathrm{crit}} \sim 1000$ is the critical Reynolds number for the onset of the KH instability (Landau and Lifshitz, 1987).

Thus for laboratory experiments discussed here the range of the spatial scales δ which can be modeled correctly is orders of magnitude less than the corresponding global scale L, albeit the ratio δ/L is not as small as in the astrophysical jets. It is worth noting here that similar limitations are applicable to computational modeling, where effects of numerical viscosity are equivalent to the relatively small values of effective "numerical" Reynolds numbers (Table V). Therefore, the laboratory experiments provide a good basis for advancement and validation of the astrophysical codes.

There is a close match for the dimensionless parameters which determine the temporal and spatial evolution of the systems. For jets in which magnetic fields are not dynamically significant (plasma $\beta \gg 1$), the dimensionless parameters commonly used in the astrophysical jet literature are as follows: the Mach number (equivalent to the Euler number in the Appendix), the density contrast (equivalent to the similarity in morphology or initial conditions in the Appendix), and the radiative cooling parameter (ratio of radiative cooling time to hydrodynamic flow time in the Appendix). Discussion of these dimensionless parameters in the context of numerical simulations of astrophysical jets can be found in Norman *et al.* (1982) and Blondin, Fryxell, and Konigl (1990). As is seen in Table V there is a good overlap between these parameters. Thus the evolution of structures developing in the interaction of laboratory jets with ambient plasma is scalable. Using the transformations discussed in the Appendix, we can determine that the scaling between the laboratory and astrophysical time scales goes as $t_{\mathrm{Ast}} = t_{\mathrm{Lab}}(L_{\mathrm{Ast}}/L_{\mathrm{Lab}})(V_{\mathrm{Lab}}/V_{\mathrm{Ast}})$. Taking spatial scales corresponding to the characteristic transverse size of the bow shock in HH43 (top part of Fig. 1), and the size of the bow shock in experiments (Fig. 15), we find that a 200 ns duration of the laboratory jet evolution corresponds to ~700 yr of the astrophysical jet evolution.

III. JETS AND OUTFLOWS: SIGNIFICANT MAGNETIC FIELD

In this section we consider experiments relevant to those types of astrophysical jets whose evolution is dominated by magnetic forces. Such jets are prone to a variety of MHD instabilities and may manifest intermittent behavior. Special experimental techniques have been developed to explore these jets in the laboratory. The techniques and experimental results are presented and compared with astrophysical models. The possible role of MHD activity in the generation of high-energy ions is briefly discussed. The section is concluded with a description of the merger of multiple current channels that may occur in the atmosphere of magnetically active stars.

A. Magnetically dominated tower jets

In the previous section, we considered jets and their interaction with the external medium for the cases where magnetic fields were absent or relatively weak (aside from the formation mechanism). We also established the connection with some astrophysical phenomena. In the current section we address the case where the magnetic field becomes critically important in jet creation, propagation, and the interaction with the ambient medium. Both "weak field" and "strong field" scenarios will be realized in astrophysical systems; see Lovelace *et al.* (2002) and Pudritz *et al.* (2007) for further details. Magnetically dominated jets could also play a role in SN explosions (Wheeler, Meier, and Wilson, 2002; Sawai, Kotake, and Yamada, 2005; Uzdensky and MacFadyen, 2006, 2007; Woosley, 2010; Branch and Wheeler, 2017.

In a number of theoretical models, astrophysical jets are believed to be driven by a combination of toroidal and poloidal magnetic fields, where the generations of toroidal components are attributed to the differential rotation in the accretion disk or between the disk and the central star. Launched and collimated by magnetic forces, these jets can propagate distances that are tens to thousands of times greater than their radius. Note also that these jets can be either kinetic or magnetic (Poynting flux) energy dominated (Lynden-Bell, 2003; Kato, Hayashi, and Matsumoto, 2004). Figure 16 illustrates the results of numerical simulations of a jet well outside the domain where it was formed. In the experiments described next a single collimated beam is created as opposed to the bipolar jets formed in most astrophysical situations.

The experimental work discussed next is most closely related to the magnetic-tower scenario (Lynden-Bell, 2003; Kato, Hayashi, and Matsumoto, 2004; Uzdensky and MacFadyen, 2006, 2007). This scenario involves the presence

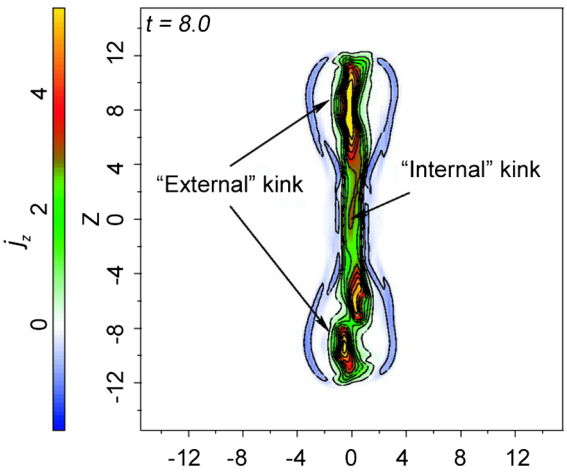

FIG. 16. The results of numerical simulation of a magnetically driven jet. The "engine" that drives the current through the central column is situated near $z = 0$. The return current flows in the outer shell that forms a characteristic "cocoon" structure. The central jet is unstable with respect to the kink mode. From Nakamura, Li, and Li, 2007.

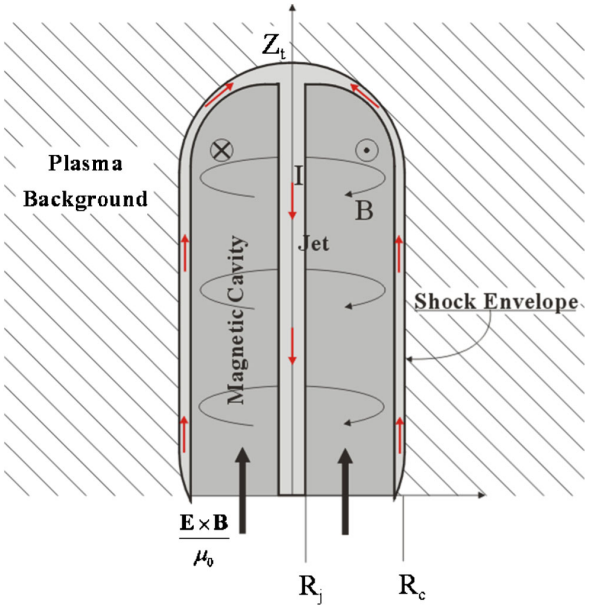

FIG. 17. Schematic of a magnetic-tower jet. The toroidal magnetic field in the cavity is supported by the current propagating through the central jet (red arrows). The ambient plasma acts to prevent rapid expansion of the cavity. A Poynting flux through the base injects magnetic energy driving the growth of the cavity. From Ciardi *et al.*, 2007.

of a magnetic cavity with a highly wound-up and predominantly toroidal magnetic field. It is the magnetic pressure of this field that accelerates the outflow. The second key ingredient of this model is the presence of an external ambient medium, acting to confine the magnetic cavity. A simplified schematic of the magnetic-tower jet model is shown in Fig. 17. The toroidal magnetic field in the cavity is supported by the current propagating through the central jet and the cavity's envelope. The growth of the cavity is driven via injection of magnetic energy at its base. In astrophysical scenarios this is provided by the winding of the initially poloidal magnetic field by rotation of an accretion disk. In laboratory experiments a similar configuration is generated via appropriately configuring the path of an electrical current driven by a pulsed-power generator as will be discussed next.

One of the experimental approaches to study these jets is based on the use of *radial wire arrays* which consist of a pair of concentric electrodes connected radially by thin metallic wires (Lebedev *et al.*, 2005a, 2005b; F. Suzuki-Vidal *et al.*, 2010); see Fig. 18(a) for the schematic. The plasma formation and the flow dynamics during the initial stage of the experiment are the same as those observed in conical wire arrays. The main difference in the radial setup is that the system reaches a stage where the wire cores near the central electrode become completely depleted of material, triggering the formation of a "magnetic bubble" and a magnetically dominated jet.

The development of the jet in this system is shown schematically in Figs. 18(b)–18(d). During the first stage [Fig. 18(b)] ablated plasma is accelerated axially by the Lorentz $J \times B$ force and fills the region above the radial array forming an ambient medium into which the magnetic tower will eventually expand. As with the conical arrays, the magnetic field and the currents remain confined in the proximity of the wires leading to a relatively high-β background plasma. Thus the magnetized jets that form will propagate into a relatively weakly magnetized medium as

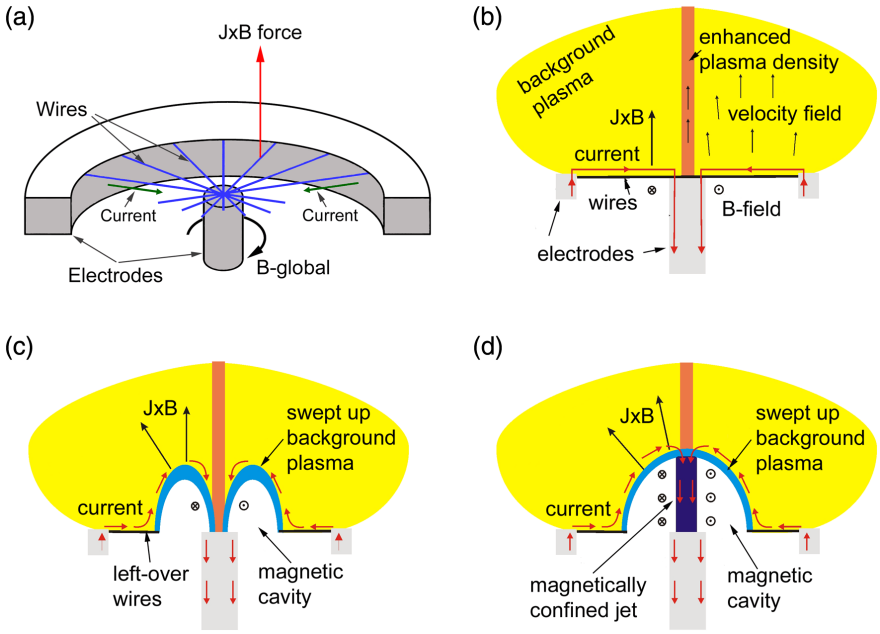

FIG. 18. (a) Schematic of a radial wire array experiment. Currents flow radially through fine metallic wires and along the central electrode, producing a toroidal magnetic field which lies below the wires; a typical radius of the radial wire arrays is ~1 cm. (b) The $J \times B$ force acting on the plasma ablated from the wires produces a plasma background above the array; resistive diffusion is slow and the current path remains close to the wires. (c) Full ablation of the wires near the central electrode leads to formation of a magnetic cavity, which evolves (d) into a magnetic-tower jet driven upward by the pressure of the toroidal magnetic field. From Lebedev *et al.*, 2005b.

is the case in many astrophysical settings. Characteristic parameters for this plasma are electron densities of $\sim 10^{17}$–10^{18} cm^{-3} and temperatures of ~20 eV. Injection of plasma into the upper regions continues until the wires are fully ablated and stop acting as mass sources. The ablation rate is highest close to the axis and at some moment in time the wires near the central electrode will be fully ablated. The disappearance of parts of the wire cores means that the swept-up plasma cannot be replenished, and the current path shown schematically in Fig. 18(b) is no longer available. Wire breakage thus leads to the development of a magnetic cavity in the background plasma, which is pushed by the rising toroidal field loops [Fig. 18(c)]. This is the beginning of the second phase of the experiment: the formation of a magnetically driven jet. The current is now forced to flow along the surface of the cavity and through the central region, where a dense jetlike plasma column develops [Figs. 18(c) and 19(d)]. The pressure of the toroidal magnetic field, associated with the current flowing in the plasma column, leads to radial and axial expansion of the magnetic tower and to the axial acceleration of the jet column. Furthermore, the confinement of the magnetic cavity is largely determined by the thermal pressure of the background ambient plasma. This is quite similar to what the models of the astrophysical magnetically driven jets assume (Lynden-Bell, 1996, 2003; Lovelace *et al.*, 2002; Uzdensky and MacFadyen, 2006, 2007).

During the past decade, laboratory experiments of the aforementioned type have produced a number of finely resolved features that are suitable for comparing with corresponding features in astrophysical jets. Parameters characterizing these experiments are summarized in Table VI, and the derived dimensionless parameters are shown in Table VII. The values of the Re, Re$_M$, and Pe numbers are all much greater than unity, meaning that these laboratory plasma jets can be well described by ideal MHD equations. Thus one could expect that the evolution of the laboratory jets should be similar to that in the magnetic-tower models of astrophysical jets, occurring on the temporal scales connected via scaling relations discussed in the Appendix.

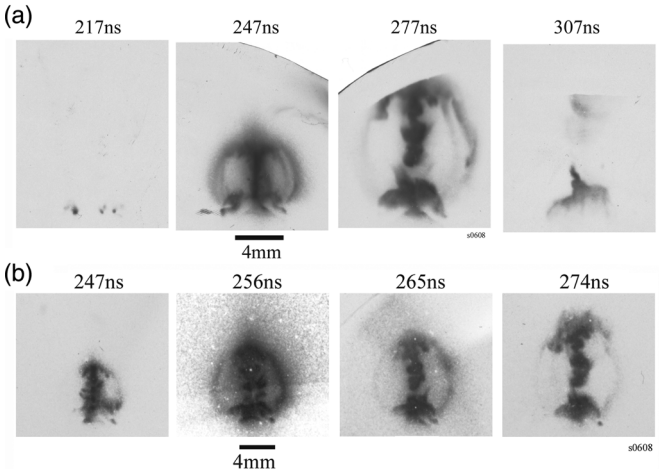

FIG. 19. Time sequence of soft x-ray images (~300 eV) obtained during a single shot showing expansion of the magnetic cavity and development of instabilities in the central jet column. The four images in (b) were taken with smaller interframe time separations and from different viewing angles than in (a). From Lebedev *et al.*, 2005b.

TABLE VI. Summary of physical parameters in the magnetic-tower jet experiment. From Lebedev *et al.*, 2005b.

Parameter	Symbol	Jet	Background plasma
Velocity (km/s)	V	100–200	10–15[a]
Density (cm^{-3})	n_i	10^{18}–10^{19}	10^{16}–10^{17}
Temperature (eV)	T	120	<20
Magnetic field (kG)	B	>500	<50
Ionization	Z	20	10–15
Atomic number	A	184 (W)	184 (W)

[a]Sound speed.

The main conclusions from the results of these experiments can be summarized as follows: The central column on axis is held from radial expansion by the toroidal magnetic field, associated with the axial current. The current then closes through the outer part of the shell, forming a familiar cocoon structure. The axial expansion of the magnetic tower occurs with velocity determined by the magnetic pressure inside the cavity and the density of the ambient plasma ahead of the cavity (at Alfvén velocity v_A calculated using a magnetic field inside the cavity and the ambient density ahead of it). In these experiments the length of the magnetic tower reached ~30 mm, a factor of 15 larger than the radius at which the magnetic energy was injected through a narrow gap at the base of the magnetic tower (at radius ~2 mm, corresponding to R_C in Fig. 17).

The high-beta plasma near the axis is generally unstable with respect to necking and kinking instabilities (Kadomtsev, 1965). With the jet propagating upward, the corresponding features are advected along the axis. All this is clearly seen in the set of images (Fig. 19) taken from Lebedev *et al.* (2005a). The central jet on the axis of the magnetic-tower cavity shows the development of $m = 0$, $m = 1$ instabilities with characteristic wavelengths of ~1 mm, comparable to the central jet radius ($kr_0 \sim 5$). Their growth time of ~2 ns is consistent with that expected for the MHD modes ($\sim R_{\rm jet}/v_A$) and is significantly shorter than the overall evolution time of the magnetic cavity of ~200 ns in these experiments.

On the other hand, Fig. 19 shows that these instabilities do not disrupt the plasma acceleration. A well-collimated, although highly structured, outflow is produced. In the experiments the level of instability development is at least partially determined by the balance between the jet acceleration time (cavity expansion time) and the time required for the driving current to "short circuit" at the base of the jet. This removes, or at least reduces, the axial current in the jet

TABLE VII. Derived dimensionless parameters for the magnetic-tower jet experiment.

Reynolds number Re	Magnetic Reynolds number Re$_M$	Peclet number Pe	Mach number M	Plasma β	Cooling parameter $\chi = \tau_{\rm cool}/\tau_{\rm dyn}$
$>10^4$	20–200	5–20	3–5	~1	10^{-3}–10^{-4}

reducing the driving force for the instability. Similar mechanisms may act at the base of an astrophysical disk-driven jet, near the disk surface (Lovelace *et al.*, 2002; Pudritz *et al.*, 2007). The fragmentation of astrophysical jets, particularly stellar jets, is well known as observations show the flows to be clumpy on small scales (Hartigan *et al.*, 2011).

The observed morphology agrees well with extensive numerical simulations of the tower jets with both laboratory plasma codes and astrophysical codes (Ciardi *et al.*, 2007; Huarte-Espinosa *et al.*, 2012). Figure 20 shows a comparison of soft x-ray images from an experiment with synthetic images from simulations using the laboratory plasma code GORGON (Chittenden *et al.*, 2004; Ciardi *et al.*, 2007). The overall evolution and the main observed features are fairly well reproduced. In both simulations and experiments the most intense emission comes from the magnetically confined central jet. The other prominent emitting region is the shock formed at the envelope of the cavity that is expanding supersonically ($M > 2$) into the cavity confining ambient material.

Simulations (Fig. 21) show the formation of tangled magnetic field structures inside the cavity, developing from the purely toroidal field due to the growth of the kink instabilities. This is seen in simulations of both the laboratory and astrophysical magnetic-tower jets. The morphological similarity of the field structures in Fig. 21 is obvious, despite the very different spatial and temporal scales involved.

The magnetic-tower jet scenario creates an outflow propagating away from the region where the driving magnetic field is injected. In Fig. 22, we show an extreme case of separation of the well-formed plasma column from the base. The azimuthal field in the separated part of the jet is maintained by the poloidal current circulating within this separated piece. This section of the flow continues propagation in the vertical direction and forms an isolated "bullet." The current at the foot of the "cocoon" zone is now reestablished and can drive the next burst of the plasma. Formation of the isolated plasma bullet is illustrated by the shadowgraphs in Fig. 22. In these experiments the total duration of the electric current pulse generated by the experimental facility was comparable with the time of the magnetic cavity expansion, so only one episode (pulse) of jet formation occurred. A modification of the setup,

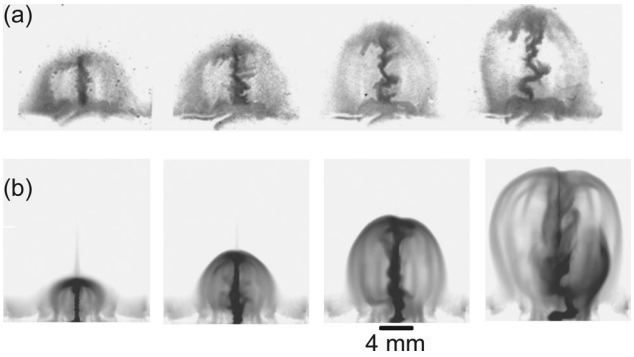

FIG. 20. (a) Time sequence of experimental soft x-ray images (~30 eV) obtained at four different times in the same experiment and (b) synthetic x-ray images from MHD simulations of the experiment. From Ciardi *et al.*, 2007.

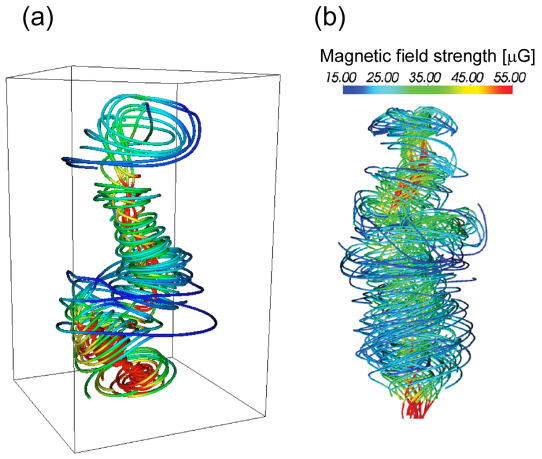

FIG. 21. Structure of magnetic field lines inside the cavity of radiatively cooled magnetic-tower jets from MHD simulations; the colors represent the field strength decreasing from red to blue: (a) laboratory experiment, 230 ns, jet height ~15 mm. From Ciardi *et al.*, 2007. (b) Astrophysical jet, 118 yr, jet height 300 AU. From Huarte-Espinosa *et al.*, 2012.

allowing formation of several episodes of magnetic-tower jets, is discussed in Sec. III.D.

New possibilities of generating larger-scale jets suitable for both the testing of scaling arguments and the introduction of new diagnostics may appear with the higher-power, higher-current drivers. The first steps in this direction have been made

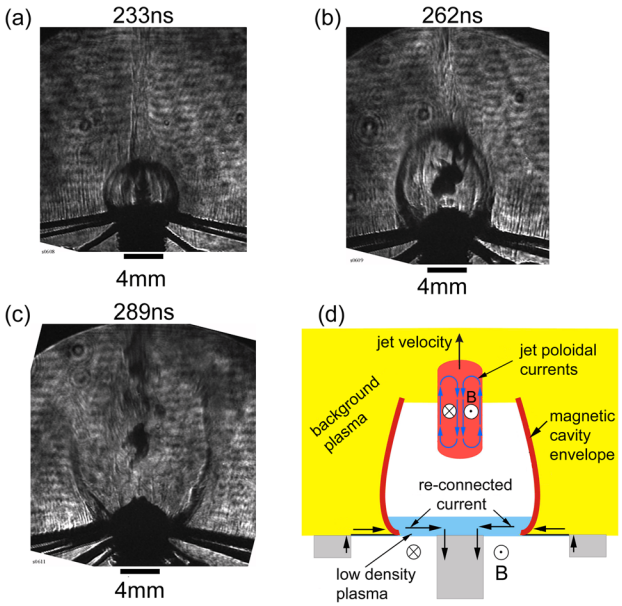

FIG. 22. Laser shadowgraphs of the magnetic jet evolution. (a) At 233 ns the magnetic cavity is well developed. A collimated jet is clearly visible on axis inside the cavity. (b) The magnetic cavity elongates axially and expands radially. Because of instabilities, sections of the jet on axis are no longer visible, and the jet assumes a clumpy structure. (c) The upper edge of the magnetic cavity breaks up and disappears. A well-collimated clumpy jet is still visible on axis. (d) Schematic of the last stage of the magnetic jet evolution, showing how currents reconnect at the foot point of the magnetic tower and a jet is ejected with entrained magnetic fields. From Lebedev *et al.*, 2005a.

with the PTS Z-pinch facility in China (Xu *et al.*, 2017), where the magnetic-tower jets have been produced and characterized with the driving currents of up to 4 MA.

B. Formation of energetic ions in a magnetic cavity

The cavity around the central jet is magnetically dominated, and the magnetic field is sufficiently strong to confine high-energy ions (Suzuki-Vidal *et al.*, 2013b). These ions can be injected into the cavity by a potential difference at the base of the cavity (~100 kV) (Burdiak *et al.*, 2013; Suzuki-Vidal *et al.*, 2011). Injection may also occur during a clump formation, where the current may experience sharp turns or even complete disruption (cf. Sec. VI.B). There is a good reason to believe that the ions most susceptible to acceleration are the protons, due to their highest Z/A ratio. The protons are always present in the system due to their residual presence in the metals used in the hardware (Suzuki-Vidal *et al.*, 2013b), in particular, in tungsten wires used in the experiments.

The presence of higher-energy ions with $W > 100$ keV was tested by a variety of techniques, including a magnetic spectrometer and an array of the proton imaging techniques based on the use of the CR-39 radiochromic films (Fleischer, Price, and Walker, 1965). The main findings were as follows: the proton spectrum extended from ~100 keV to ~3 MeV. The higher-energy (>600 keV) protons originated from the central area of the cavity around the clumpy jet well above the wire array. We take 3 MeV as a reference for the maximum energy. Note that the protons with an energy exceeding 100 keV have a very long mean-free path in the cocoon plasma. For the tungsten plasma of $T = 20$ eV temperature, $n_e = 10^{18}$ cm^{-3} density, and $Z = 5$ the 100 KeV protons have a mean-free path of 60 m. The 100 keV proton slowing length (due to the friction against the electron gas) is also large, ~20 cm. These numbers become very large near the cutoff energy of 3 MeV. This means that the high-energy proton formation is not affected by collisions. This is especially true inside the magnetically dominated cavity where the plasma density is smaller.

To get an energy of 3 MeV in one "kick" the proton would have to cross a voltage drop of 3 MV. This is much too high (by factor of 10–30) compared to what the circuits involved in the experiments can produce. The maximum inductive voltage drop is ~100 kV. Also, the presence of 3 MV drop would show up in the generation of intense electron beams inevitably accompanied by the hard x rays (up to 3 MeV), which are absent in the experiment. Therefore, we conclude that the ion acceleration cannot occur in one big step, but is rather produced in the multiple ion interactions with time-varying ("moving") magnetic field nonuniformities, very much as in a Fermi mechanism (Fermi, 1949).

Taking as a cutoff energy of accelerated protons the energy of $W_{\max} = 3$ MeV, we should consider whether such protons could be confined in a cavity of the observed size and the magnetic field strength. For the current $I_{\rm jet}$ through the central jet of 1 MA, and the cavity radius of $a = 1$ cm, the field strength at its periphery is $B_a = \mu_0 I_{\rm jet}/2\pi a \sim 20$ T. For such a field strength the gyroradius of 3 MeV protons is 1.25 cm, i.e., comparable to the cavity size. Imposing this condition as a rough constraint on the maximum proton energy compatible with the size of the cocoon, one can write this constraint as

$$(\gamma_{\max}^2 - 1)^{1/2} < 2I_{\rm jet}/I_{pA}, \tag{3.1}$$

where $I_{pA} \equiv 2\pi m_p c/e\mu_0 \approx 30$ MA is a so-called proton Alfvén current. We introduced here a factor $\gamma \equiv 1 + W/m_p c^2$ in order to be able to cover relativistic energies, if needed (see later). In the nonrelativistic case it agrees with the aforementioned estimate of the maximum proton energy in experiment by Suzuki-Vidal *et al.* (2013b).

The protons execute complex orbits, with a characteristic orbiting period of $\sim 2\pi a/v_{p,\max}$. The presence of random variations of the centroid of the current-carrying column caused by its MHD instabilities produces random perturbations of the magnetic field with a characteristic time scale of $\tau \sim r_{\rm jet}/v_A$. This generates random vortex electric fields which can cause diffusion of the protons in velocity space with a diffusion coefficient $D_v \sim (\Delta v)^2/\tau$ (where Δv is the velocity change in each event). The same statement can be rephrased in terms of the second-order Fermi mechanism, where the inductive electric field would be associated with the magnetic features with velocities $\pm\Delta v$, giving small random kicks to the protons.

The fastest diffusive acceleration occurs in the vicinity of the jet, since the instability-induced fluctuations of the magnetic field are highest there. For a strongly distorted jet, the changes of the velocity are on the order of the Alfvén velocity itself, with v_A evaluated at the jet surface. Making a standard diffusive estimate for the velocity of protons achieved within some time t,

$$V^2 \sim 2D_V t, \tag{3.2}$$

one finds that

$$V \sim v_A \sqrt{2v_A t/r_{\rm jet}}. \tag{3.3}$$

This part of the discussion pertains to a nonrelativistic case as in Suzuki-Vidal *et al.* (2013b). Taking the numbers typical for this experiment, $v_A \sim 4 \times 10^7$ cm/s, $r_{\rm jet} \sim 0.1$ cm, and $t \sim 250$ ns, we find $V \sim 6 \times 10^8$ cm/s corresponding to the proton energy $W \sim 150$ keV. Obviously, this number is significantly smaller than the maximum energy of 3 MeV. However, the Gaussian tail of the diffusive distribution would extend at least a factor of 2–3 over the rms value of $V \sim 6 \times 10^8$ cm/s, easily yielding an energy of 600 keV. In this regard the number looks consistent with the spectral information from the experiment; see Fig. 23.

With regard to the highest detected energies (~3 MeV) some non-Gaussian effects may play a role, in particular, related to a special choice of the initial phase-space characteristics of the accelerated particle (location and three velocity components). One can then get a nondiffusive acceleration (first-order Fermi), limited only by the particle confinement within the cocoon, as previously mentioned ("Hillas constraint") (Hillas, 1984). Although the first-order mechanism has been studied in great detail (Longair, 2011) its existence

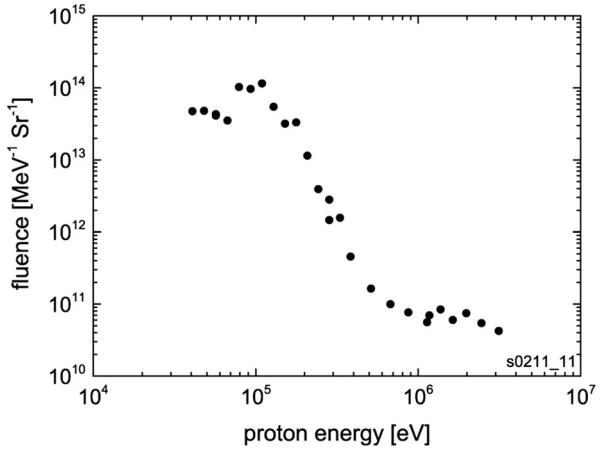

FIG. 23. Proton energy spectrum measured by the magnetic spectrometer in magnetic-tower jet experiments. From Suzuki-Vidal *et al.*, 2013b.

and efficiency in the cocoon setting previously described has not been proven yet. If this mechanism turns out to work for the astrophysical jets, higher-energy protons should be generated there as well. The maximum (cutoff) energy would still be determined by Eq. (3.1). In the astrophysical setting the jet current can easily reach $(10^3$–$10^5)I_A$. If the basic physics behind the clumpy high-current jets remains similar to that described in Secs. III.A–III.C, then the magnetic-tower jets should correlate with the sources of relativistic protons and be considered as injection points for cosmic ray acceleration. We note that astrophysical jets, particularly relativistic flows associated with gamma ray bursts, have often been suggested as particle acceleration sites (Bosch-Ramon and Rieger, 2012). A strong support to the mechanism just discussed is experimental scaling of the maximum proton energy versus the pinch current as described by Eq. (3.1). Such experiments are yet to come.

C. Possible role of an axial magnetic field

In the physics of the jet launching from the central part of an accretion disk, an important issue is that of the relative role of the toroidal and axial components of the magnetic field (Lovelace *et al.*, 2002; Pudritz *et al.*, 2007). Experiments with radial wire arrays provide a natural platform to address this issue experimentally. In the study of F. Suzuki-Vidal *et al.* (2010) the axial field was added using a solenoid connected in the path of the current driving the radial wire array. The axial field produced near the center of the launch area was $B_Z \sim 5$ T. Because of a significant magnetic Reynolds number of this experiment ($\mathrm{Re}_M \sim 20$, Table VII), the field was line tied to the plasma of the emerging jet and compressed together with it.

The contribution of the axial field pressure limited the jet compression at the radii somewhat larger than in the absence of the field. The maximum value of the axial field was as high as 200 T, comparable with the magnitude of the drive field (100 T). The limit to the achievable degree of compression should have led to lower plasma temperatures (compared to the no B_Z case); indeed, an increase of the minimum jet radius and a reduction of the x-ray emission intensity at compression are observed.

The axial magnetic field of the achieved values is not sufficient to stabilize the fastest-growing modes of MHD instability of a current-carrying column. So, the formation of clumps was not noticeably affected. The main conclusion from this discussion is that compressed axial fields, even those as high as the drive toroidal field, do not have any dramatic effects on the jet launching.

To address the role of the jet instabilities on the global properties of the magnetic cavity growth and jet propagation (in the setting with the anode made of a thin foil), a thin metal needle (stainless steel, 400 μm diameter, 1 cm long) was added above the foil along the axis of the system (Francisco Suzuki-Vidal *et al.*, 2010). The presence of the needle provided a well-defined, fixed path for the current which was not affected by the instabilities. This prevented radial displacements (wiggling) of the jet and excluded disruptions of the current. The needle made an early stage of the discharge more smooth and led to faster growth of the magnetic cavity (~40% faster in both radial and axial directions), which is consistent with the larger value of current flowing through the central jet.

Current-driven instabilities of the central column were also experimentally observed and numerically simulated by Gourdain *et al.* (2012) for a thin (10 μm) Al foil driven through a small-diameter (0.5 mm) "pin" cathode. The development of a kink mode was clearly identified and they observed that insertion of a metal needle on the axis of the system led to suppression of this mode and to general symmetrization of the discharge. In general, experiments with the central needle suggest that the development of MHD instabilities in the central plasma column could provide feedback for the process of an episodic formation of magnetic cavities.

D. Episodic magnetic-tower jets

In the magnetic-tower jet model (Lynden-Bell, 2003) the formation of the magnetically driven jet or cavity is intrinsically transient, and experiments described in Sec. III.A investigated properties of the outflows formed during a single episode of the magnetic cavity expansion. A closure of the gap through which the magnetic flux is injected into the cavity by a plasma could lead to current reconnection at the jet base [Fig. 22(d)]. Such a reconnection restores the initial magnetic field configuration, providing conditions for a new episode of magnetic-tower jet formation as schematically illustrated in Fig. 24. The possibility of episodic magnetic-tower jet activity was investigated using a modified experimental setup in which the radial wires were replaced by a thin radial foil (Ciardi *et al.*, 2009; Suzuki-Vidal *et al.*, 2009). Average mass per unit area decreased in the radial direction of a radial wire array, whereas for a foil of constant thickness, the same parameter did not depend on the radius. The foil was therefore ablated and pushed up to form a cavity in a narrower region near the axis leading to ejection of a bubble of smaller radius and energy content. The smaller radial extent where all foil material was ablated created conditions for more frequent "reconnection" of the current at the base. This led to the generation of several subsequent magnetic cavities and jets (Ciardi *et al.*, 2009; Suzuki-Vidal *et al.*, 2009). A detailed

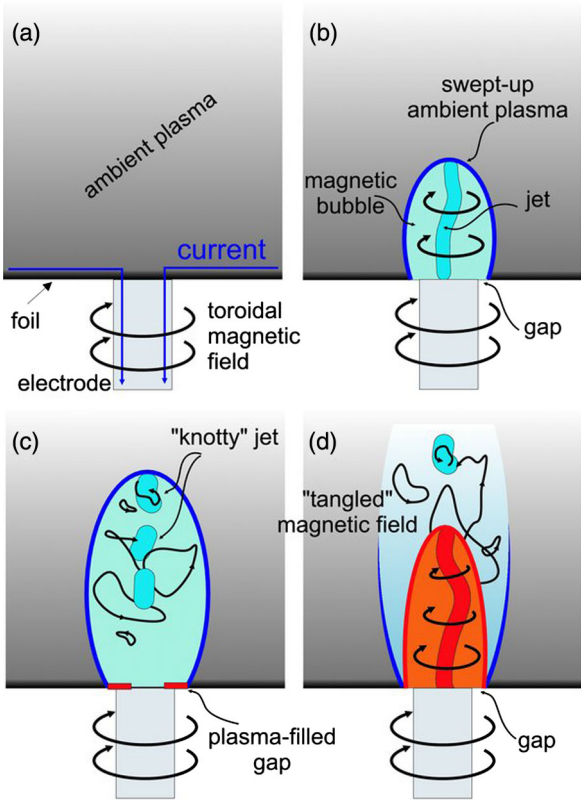

FIG. 24. Schematic illustrating formation of episodic magnetic-tower outflows in experiments. Filling of the gap at the base of the magnetic cavity by plasma restores the initial magnetic configuration. A new jet and bubble (red) then formed (d), which propagate and interact with the plasma and "tangled" magnetic field left by the previous ejection event (blue). From Ciardi *et al.*, 2009.

experimental characterization of the processes occurring in the foil during the discharge can be found by Gourdain *et al.* (2010) based on the Cornell Beam Research Accelerator (COBRA) pulsed-power device at Cornell University.

After the reconnection event had occurred and led to a separation of the jet from the base (similar to what is shown in Fig. 22), a new cavity could start growing, with a new jet emerging from the base. This was accompanied by an episodic burst of soft x rays generated during compression of the central jet. The time evolution of the jets and bubbles is presented in Fig. 25. A succession of multiple cavities and embedded jets is seen to propagate over length scales spanning more than an order of magnitude—from the smallest to the largest bubble. The central jet in each of the subsequent cavities is unstable to current-driven instabilities, with the characteristic growth time of a few nanoseconds. This corresponds to the Alfvén propagation time across the jet radius. The second time scale in this experiment is the magnetic cavity ejection period, which was a factor of 10–20 longer and linked to the temporal variability of the Poynting flux feeding the cavities. It is important to note that episodic jet formation appeared in several numerical simulations of young stellar objects jet launching (Goodson, Winglee, and Böhm, 1997; Goodson, Böhm, and Winglee, 1999; Goodson and Winglee, 1999; Romanova *et al.*, 2006).

The resulting flow observed in the experiments is heterogeneous and clumpy and is injected into a long-lasting and well-collimated channel made of nested cavities. It is worth remarking that the bow-shaped envelope is driven by the magnetic field and not hydrodynamically by the jet. Another interesting observation was the increase of the axial expansion velocities of the subsequent cavities. This occurs due to their propagation through a smaller density as a substantial part of the plasma was "swept" to the central column in a previous episode (Ciardi *et al.*, 2009). The subsequent clumps may have higher axial velocity than the preceding ones, this leading to an overtaking effect and formation of the internal shocks in the clumpy outflow. The characterization of knots in many astrophysical jets also shows them to be propagating into environments that are already in motion (Hartigan *et al.*, 2011). Thus the experiments allow researchers to explore a key aspect of astrophysical jet evolution.

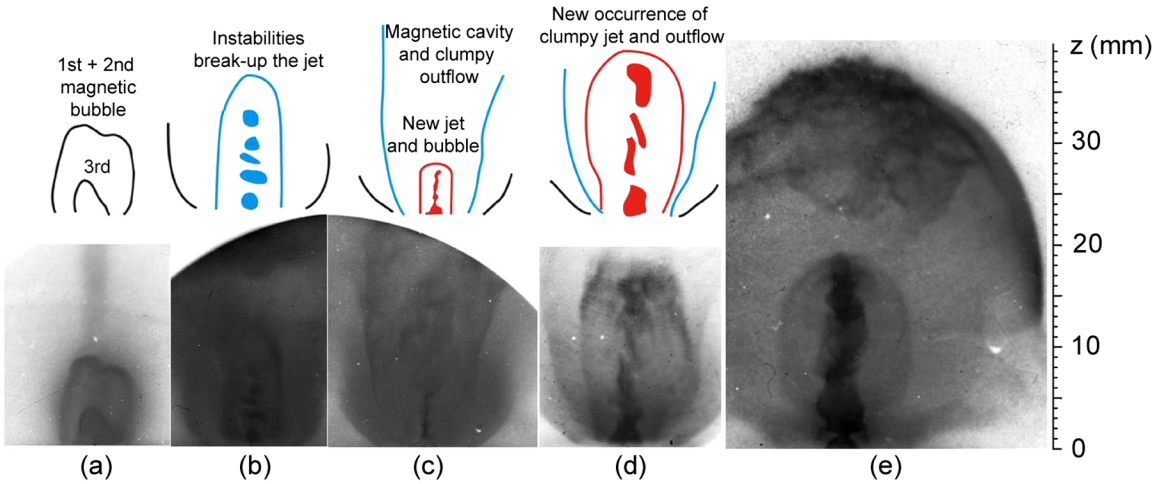

FIG. 25. Time sequence of soft x-ray images showing the evolution of episodic magnetically driven jets with images taken at (a) 286, (b) 346, (c) 376, (d) 406, and (e) 487 ns after the driving current start. The schematic cartoon serves to guide the eye; the features are described in the main text. From Ciardi *et al.*, 2009.

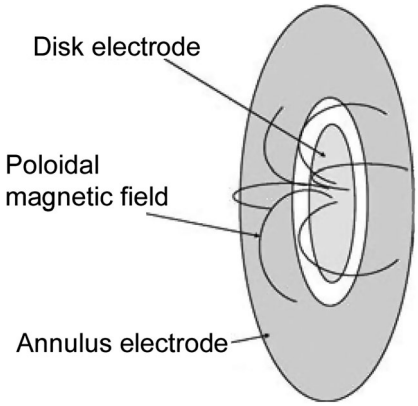

FIG. 26. Schematic of the Caltech experiment on the merging of current channels and formation of an axial jet. This structure is attached to a large vacuum chamber (not shown) extending by ~1.5 m to the left, with diameter ~1.4 m. The formed plasma objects are observed through several ports in the chamber; magnetic probes are used for *in situ* measurements of the magnetic field. From Bellan, You, and Hsu, 2005.

The dimensionless parameters characterizing this experiment are similar to those shown in Table VII and a similar scaling can be applied to consider astrophysical implications of the results of this experiment. This was discussed by Ciardi *et al.* (2009) and F. Suzuki-Vidal *et al.* (2010), where they suggested that the scaling of the experiment to the parameters of protostellar jets indicates that the presence of multiple bubblelike features should be observed on scales of a few hundred of AU from the source, while the nonaxisymmetric features from the current-driven instabilities should appear within tens of AU. This is consistent with the observations of outflows from, e.g., the DG Tauri star which demonstrate many morphological features similar to those observed in the experiments: ejection variability, limb-brightened bubblelike structures, and the presence of wiggles in the optical jet evident on scales ranging from tens to a few hundred of AU from the source (Bacciotti *et al.*, 2000, 2002; Dougados *et al.*, 2000). Some possible connections between the results of the episodic magnetically driven jet experiments and the astrophysical observations and numerical models were discussed by Mereghetti (2008), McKinney and Blandford (2009), Ciardi and Hennebelle (2010), Moll (2010), Pascoli and Lahoche (2010), Agra-Amboage *et al.* (2011), Savin *et al.* (2012), Federrath *et al.* (2014), White *et al.* (2014), and Metzger *et al.* (2015).

E. Magnetic arches and their stability

Interesting features of astrophysically relevant jets have been revealed in the experiments by the Caltech group based on the pulsed-power techniques related to the spheromak magnetic configuration (Bellan, 2000). The dimensions of the plasma objects in these experiments reach tens of centimeters, and the evolution time of the plasma objects exceeds several microseconds, i.e., orders of magnitude larger than in the fast *Z* pinches. Still, the basic physics underlying the evolution of the jets remains the same and some of the images are very similar to their mm-size counterparts. This once again indicates the potential of the scalings and similarities in relation to astrophysics. A detailed comparison of the spheromak-produced laboratory jets with astrophysical models was given by Bellan (2018a, Bellan, 2018b); see also You *et al.* (2018).

The basic configuration of the Caltech experiment is shown in Fig. 26 (Bellan, You, and Hsu, 2005). The poloidal magnetic field threads two electrodes, the inner disk (cathode) and the outer annulus (anode). In several points (roughly at the foot points of those field lines that are shown in the figure) the working gas is injected, and the voltage of a few kV is applied between the inner and the outer electrodes. As breakdown occurs the current starts flowing predominantly between the foot points ending at the location of the gas inlets. The poloidal current causes mutual attraction of the inner "stems" of the current channels and, at the same time, pushes the outer stems outward, similar to the magnetic-tower jet configuration discussed earlier. This dynamics is reflected in the optical images shown in a set of consecutive snapshots in Fig. 27.

In the first few frames of Fig. 27, one sees a process of merging of the inner stems and formation of one bright current channel; the current is closed through the outer shroud

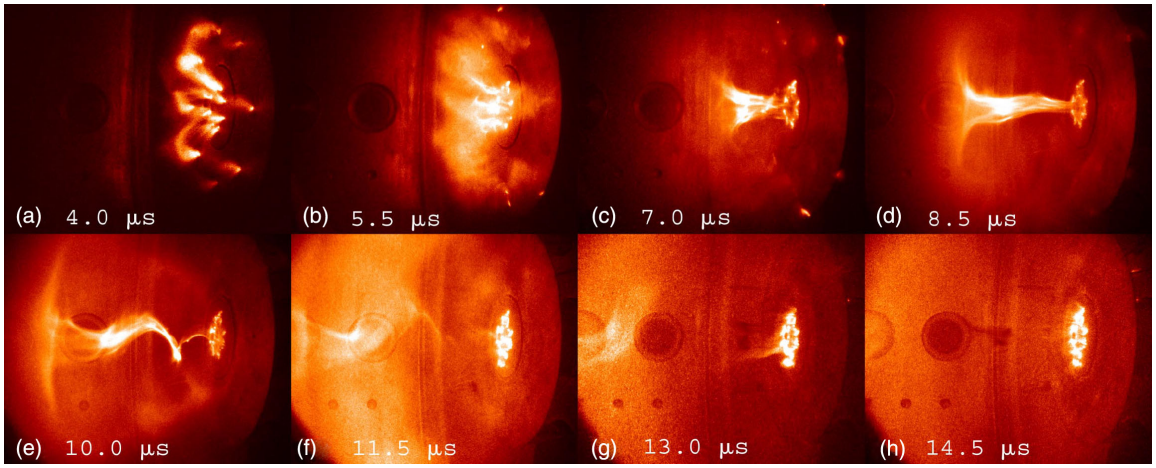

FIG. 27. A sequence of snapshots showing an evolution of the plasma. The time after applying the voltage between the electrodes is shown in each frame. From Hsu and Bellan, 2002.

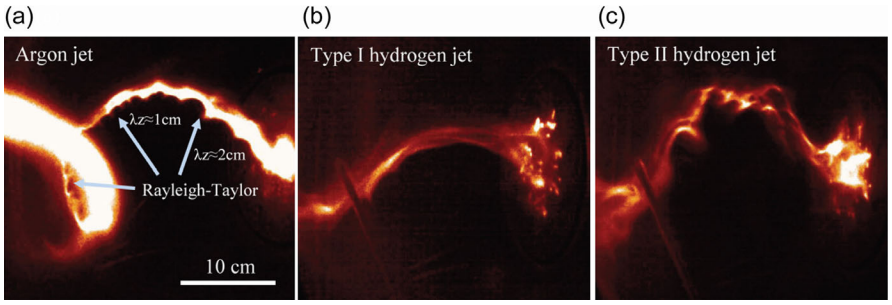

FIG. 28. Development of the finer structure on the twisted jets, experiencing lateral acceleration. From Zhai and Bellan, 2016.

which grows in size and eventually leaves the field of view. The central jet propagates away from the electrodes. As it propagates it shows signs of kinking and then, eventually, dissipates. The characteristic plasma parameters in this experiment were (Hsu and Bellan, 2002): plasma density (hydrogen) $n_e \sim 10^{14}$ cm^{-3}, T_e, $T_i <$ 5–20 eV, $B = 0.2$–1 kG, and the duration of the shot ~15 μs. The length of the jet at $t = 10$ μs is $L \sim 50$ cm. The Coulomb mean-free path for $T_e = T_i =$ 10 eV is 3 cm, i.e., the plasma is mildly collisional. The ion gyroradius for $T_i = 10$ eV and $B = 0.5$ kG is ~1 cm, i.e., less than the jet radius. The magnetic diffusivity D_M is $\sim 10^5$ cm^2/s, i.e., the magnetic diffusion time $\tau_{\rm diff}$ over the jet radius of $r \sim 3$ cm is $\tau_{\rm diff} \sim r^2/2D_M \sim 30$ μs. Thus an MHD approach can be used in the analysis of the jet behavior, at least qualitatively. The jet kinking is a part of the MHD predictions, although specific results may depend on such factors as the axial current distribution over the radius, as well as the possible effect of the velocity shear, similar to those discussed in Sec. III.F.

As emphasized, applying a voltage between the electrodes in the preimposed poloidal field is equivalent, in terms of the effects produced, to the rotation of the electrodes. Therefore, the setting of Fig. 26 imitates processes occurring near the foot of the jet and related to the presence of the differentially rotating accretion disk (Bellan, 2018a, 2018b). This kind of phenomena has been the subject of considerable interest in astrophysical disk simulations (Romanova *et al.*, 2004).

Higher resolution optical imaging used in recent experiments of the Caltech group allowed them to detect some finer features on the jet images; see Fig. 28 that contains snapshots of a shorter segment of the jet seen in Fig. 27. In the course of violent lateral motions generated by the kink instability, the surface of a jet may also experience high lateral acceleration. This creates conditions for the Rayleigh-Taylor instability at the interfaces. Moser and Bellan (2012) and Zhai and Bellan (2016) attribute the features shown in Fig. 28 to this instability. In these experiments both hydrogen and argon plasma were used. In an argon plasma [Fig. 28(a)] the lateral acceleration of 10^{10} cm/s^2 generated this effect quite reproducibly. In hydrogen, with the same acceleration the effect was not detectable [Fig. 28(b)]; however, at higher acceleration of 10^{11} cm/s^2 it reappeared as shown in Fig. 28(c).

F. MHD equilibria stabilized by the shear flow

A plasma column where the plasma pressure is balanced by the magnetic pressure is often considered as a reasonable representation of magnetically dominated astrophysical jets. However, it is well known that an equilibrium pinch is unstable with respect to the formation of "necks" ($m = 0$), as well as "kinks" ($m = 1$). These instabilities are identified as a common occurrence in the dynamics of long, thin, current-carrying astrophysical jets (Benford, 1978; Begelman, 1998; Reipurth and Bally, 2001; Nakamura and Meier, 2004). The growth of both modes is associated with the release of the magnetic energy due to changes in the current distribution and can be evaluated on the basis of the MHD energy principle; see the review by Kadomtsev (1965). The growth rate Γ is highest for the perturbations with the axial length scale $1/k_z$ comparable to the equilibrium pinch radius a (i.e., for $k_z a \sim 1$) and is roughly equal to $\Gamma \sim v_A/a$, where v_A is the Alfvén velocity. Note that there are special pressure distributions (Kadomtsev's profile) for which the instability is stabilized (Kadomtsev, 1965); however, if the pinch equilibrium is not specially tailored from the outset, this profile does not form automatically.

The possibility to stabilize such MHD instabilities by introducing a sheared axial flow velocity $[v_z(r)]$ was investigated in experiments with the so-called "flow pinch," described in the context of the laboratory astrophysics by Shumlak, Nelson, and Balick (2007) and Shumlak *et al.* (2017). The parameters of the hydrogen plasma in these experiments are (Shumlak, Nelson, and Balick, 2007) plasma radius $a = 1$ cm, plasma length 100 cm, plasma density $n = 10^{16}$ cm^{-3}, plasma temperature $T = 100$ eV, and flow velocity on axis $v = 10^7$ cm/s. The azimuthal magnetic field is zero on axis and reaches 25 kG on the pinch radial boundary. The particle mean-free path (3 cm) is somewhat larger than the plasma radius. Importantly, the plasma flow has significant shear in the radial direction, with the flow being faster on axis and slower on the periphery. The presence of velocity shear leads to stabilization of the sausage instability. It is worth noting that such shear flows are likely to occur in jets from accretion disks as the foot points of flow rotate at the local Keplerian velocity (Ferreira, Dougados, and Cabrit, 2006). The characteristic growth rate of the sausage instability in this experiment is $\sim v_A/a$ and stabilization occurs if the radial shear dv/dr is sufficiently high, $dv/dr > v_A/a$. The qualitative explanation of the shear stabilization is that the shear destroys radial coherence of the mode, by stretching the perturbation along the axis. This, perhaps, may serve as one of the factors explaining the remarkable length of some of the astrophysical jets.

IV. ROTATING PLASMAS: TOWARD AN ACCRETION DISK EXPERIMENTAL PLATFORM

Momentum transport in accretion disks is among the most intriguing issues of the modern astrophysics. Is the momentum transport caused by the plasma turbulence? If so, what kind of turbulence is involved? Is the magnetic field a significant player? Novel techniques developed on pulsed-power facilities have allowed experimenters to take the first steps in producing rotating plasma disks whose behavior may help in answering some of the aforementioned questions.

Accretion disks (Pringle, 1981) are formed around a variety of celestial objects, from young stars to supermassive black holes in the center of galaxies. They "feed" central objects and are also thought to be responsible for the formation of jets that emanate from the vicinity of the central object. To feed a central object, meaning to allow accretion to occur, some viscous mechanism is needed for transferring angular momentum from the inner to the outer parts of the disk. Despite a very high Reynolds number ($>10^{10}$), purely hydrodynamic turbulent viscosity is insufficient to produce the necessary momentum transfer (Shakura and Sunyaev, 1973; Balbus, 2011). Magnetic fields are thought to play an important role in this process through the creation of new unstable modes such as the magnetorotational instability [(Balbus and Hawley, 1991); see also Velikhov (1959)]. The interaction of gravity, shear flows, and magnetic fields creates a complex dynamical system that is the subject of active study observationally, theoretically, and numerically. The role of the fluid turbulence, magnetic fields, and disk vertical structure are all examples of open questions in the study of accretion disks (Thompson, 2006; Käpylä *et al.*, 2010; Balbus, 2011).

Unfortunately, laboratory experiments, including those using pulsed-power devices, cannot reproduce the gravity of the central object, and this limitation makes laboratory simulation of full accretion disk physics impossible. Still, as shown in recent years, it is possible to reproduce key aspects of the sheared rotation of magnetized plasmas and transformation of the radially convergent flow into the bipolar jets (Ryutov, 2011). This experimental approach allows studies of fast phenomena occurring on a time scale of one rotation period. Modeling phenomena that develop on time scales of many (∼100) rotation periods remain beyond the current capabilities of pulsed-power or laser-driven experiments.

In spite of this limitation, plasma effects occurring in a turbulent rotating plasma disk during a single rotation period are of interest as these can occur in the zone in the innermost part of the astrophysical disk-jet system, including the launch of jets and the transfer of angular momentum to these jets. Specific aspects of accretion disk physics which could be amenable for laboratory study include turbulent anomalous viscosity, the interaction of differentially rotating disks with a magnetic field, and the formation of axial outflows from the inner boundaries of the disk.

The first steps in creating plasma flows with nonzero angular momentum were made by Ampleford *et al.* (2008) using a "twisted" conical wire array (Fig. 29) to add spin to a jet. Compared to untwisted arrays, in this case some axial magnetic field was generated by the azimuthal component of the currents appearing due to the twisting. The plasma streams

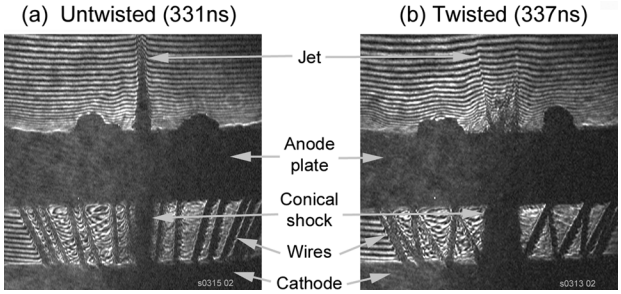

FIG. 29. Schlieren images of the plasma flows in (a) nontwisted and (b) twisted Al wire arrays. The jet is a dark feature near the axis. Also seen are wires and upper and lower electrodes. Note that the jets look dark due to high density gradients within them. The presence of plasma rotation in the jets is inferred from the twisted filamentary features visible on the shadowgrams at higher magnification [see Fig. 4 in Ampleford *et al.* (2008).

flowing toward the axis received a finite angular momentum from the global *axial* magnetic field (in addition to the radial momentum that they receive from the global *azimuthal* field). Converging near the axis, these streams merged into the plasma jet spinning around its axis and propagating upward, as described in Secs. II.A and II.B. The difference between the jets exiting the wire arrays in twisted [Fig. 29(b)] and untwisted [Fig. 29(a)] cases is obvious. The larger diameter of the rotating jet is related to the effect of the centrifugal force. Typical flow parameters in the jets formed from tungsten wires were $A = 183$, $Z = 5$, $n_e = 4 \times 10^{17}$ cm^{-3}, $T_e = 20$ eV, jet axial velocity at the upper end of the array $V = 10^7$ cm/s, and rotation velocity 25 km/s (all values were inferred from MHD simulations, shadowgraphy, and interferography). As seen from these numbers, the jet is made of a highly collisional plasma ($\lambda_{ei} \sim 60$ μm, $\lambda_{ii} \sim 2.5$ μm) that can be accurately described by the standard MHD equations. Dimensionless parameters characterizing the jets are similar to those reported for young stellar object jets (as discussed in Sec. II), including the ratio of rotational and axial velocities of 10%–25% (Coffey *et al.*, 2004).

The formation of "braids" in the rotating jets is related to the discrete nature of the sources; the aforementioned twisting of the braids [visible in Fig. 29(b) and, more clearly, in Fig. 2 of the original paper by Ampleford *et al.* (2008)] is caused by the plasma rotation and can be used for determining the pitch of the rotating flow, allowing for the estimate of the azimuthal velocity. Taken as a whole this configuration provides an interesting platform for developing a better understanding of the physics of rotating jets. For example, numerical simulations of astrophysical jets interacting with ambient media suggest that jet rotation could lead to observable differences in the morphology of interaction (Ciardi *et al.*, 2008), and the experimental platform allows one to test such predictions. We note the importance of such flows in astrophysical studies where observations have measured the rotation rates for a number of YSO jets. These rotation rates have then been used to distinguish between different jet launching models (i.e., physics occurring in the accretion disks) (Bacciotti *et al.*, 2002; Frank *et al.*, 2014; Coffey *et al.*, 2015, Lee *et al.*, 2017).

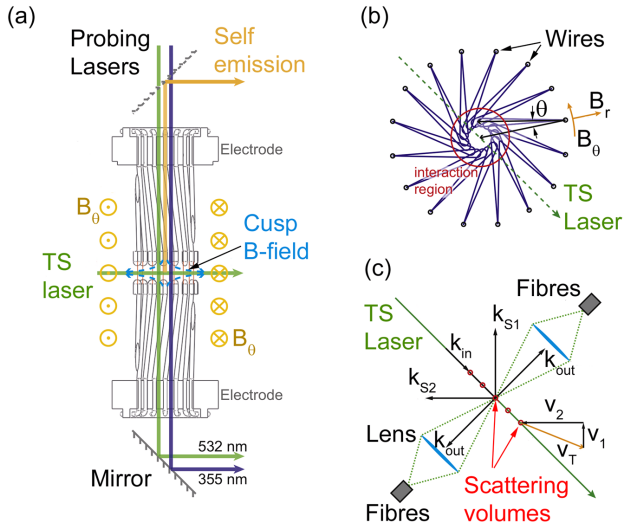

FIG. 30. The generation of a rotating plasma disk. (a) The wire array (16 Al wires) is only 4 mm tall and occupies a short section in the middle of the whole structure, whose diameter is 16 mm. Therefore, the plasma would indeed form a disk. The rest of the hardware is made of two sets of 1-mm-diameter conductors supplying a current separately to each wire. The upper and lower sets are twisted in the opposite directions but match the positions of the wires of the wire array. The presence of the twists in the upper and lower structures leads to formation of an axial magnetic field directed oppositely above and below the midplane. This causes formation of a cusp magnetic field around the midplane, with the field being almost radial at the location of the wires. (b) The flow, formed by the plasma ablated from the wires, streams toward the center with some offset, caused by the "kick" produced by the azimuthal force $\propto j_z B_r$. As a result, a rotating plasma disk is formed that is held from the expansion in the radial direction by the ram pressure of the incoming plasma [cf. Ryutov (2011)]. (c) The orientation of the incoming and scattered light in the Thomson scattering system that allows measuring the rotation velocity and plasma temperature. From Bennett *et al.*, 2015.

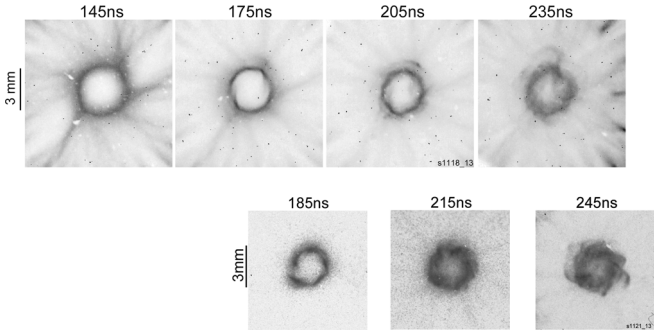

FIG. 31. XUV images of the disk obtained in two identical shots (top and bottom rows, respectively) with aluminum wire array, 16 wires, 30 mm diameter. From Bennett *et al.*, 2015.

The next important step was to limit the axial extent of the rotating plasma and thereby to produce a rotating disk. This was attained by using a novel configuration (Bennett *et al.*, 2015) of conductors and wires, illustrated in Fig. 30 where explanations of the operation are given in the figure caption.

Self-emission optical and XUV images indicate the formation of a disk of diameter 3 mm near the axis (with the diameter of the array of 16 mm); see Fig. 31. The Thomson scattering measurements of the rotation velocity yield $v_{\rm rot} \sim 6 \times 10^6$ cm/s. Fine structure appearing at the images late in time and reminiscent of spiral arms may be driven by shear-flow instabilities. Note that between the first and last frames, the plasma makes a full rotation around the axis.

There is, of course, no gravity, but the disk is confined radially by the ram pressure of the incoming streams. Since there is no confinement in the z direction, a bipolar plasma outflow is formed, very similar morphologically to outflows from astrophysical disks where gravitational "confinement" cannot counter the combination of the magnetic and thermal pressure pushing plasma away from the center along the vertical axis.

MHD simulations (Bocchi *et al.*, 2013) of these experiments reproduce the main features of the overall evolution of the rotating plasma disks and the formation of bipolar outflows; see Fig. 32. Characteristic plasma parameters in a disk made by the ablation of copper wires are as follows (at 160 ns from the driving current start): radius of the spinning disk $a \sim 1.5$ mm, electron density $n_e \sim 3 \times 10^{17}$ cm^{-3}, temperature $T \sim 15$ eV, rotation velocity $v_{\rm rot} \sim 6 \times 10^6$ cm/s, axial velocity $V \sim 3 \times 10^7$ cm/s, $A = 64$, and $Z \sim 3$. For this set of parameters we find the magnetic diffusivity $D_M \sim 2 \times 10^5$ cm^2/s and kinematic viscosity $\nu \sim 10$ cm^2/s. Note we used simple approximate expressions of Ryutov (2015) [note also a typo in Eq. (27) of that paper, where the exponent of the temperature should be 5/2 instead of 3/2 although the numerical coefficient is correct].

The corresponding dimensionless parameters are $\mathrm{Re}_M = a v_{\rm rot}/D_M \sim 5$, $\mathrm{Re} = a v_{\rm rot}/\nu \sim 10^5$, and $\mathrm{Pr} = \mathrm{Re}_M/\mathrm{Re} \sim 5 \times 10^{-5}$. The small value of the magnetic Prandtl number is relevant to conditions expected in the inner parts of protoplanetary disks (Balbus and Henri, 2008). The magnetic Reynolds number exceeds unity which means that the radial magnetic field embedded in the rotating disk will experience significant stretching by differential rotation. Such "winding" of the field is an essential step in so-called $\alpha - \Omega$ dynamo models which are expected to be a principal means by which fields are generated in disks (Moffatt, 1978). Experiments on higher-current facilities, such as the PTS facility in China (Xu *et al.*, 2017), could allow the production of disks with higher values of magnetic Reynolds numbers.

The large Reynolds number implies that hydrodynamic turbulence in the experiment can be fully developed. The rotating disk formed in these experiments is initially smooth, but then demonstrates the development of azimuthal perturbations which start at the longest spatial scale ($m = 2$ azimuthal mode) and rapidly progress toward much shorter scales (Fig. 31). Even more important, the late-time images in Fig. 31 show a significant inward expansion of the inner boundary of the disk, which occurs on a time scale of only ~50 ns (~0.5 of rotation period). This time scale is significantly (by 4–5 orders of magnitude) smaller than the diffusion time ($t \sim a^2/\nu_{\rm Sp} \sim 2 \times 10^{-3}$ s) calculated for the classical (Spitzer) viscosity. The observed fast inward expansion of the rotating disk can be interpreted as evidence of the

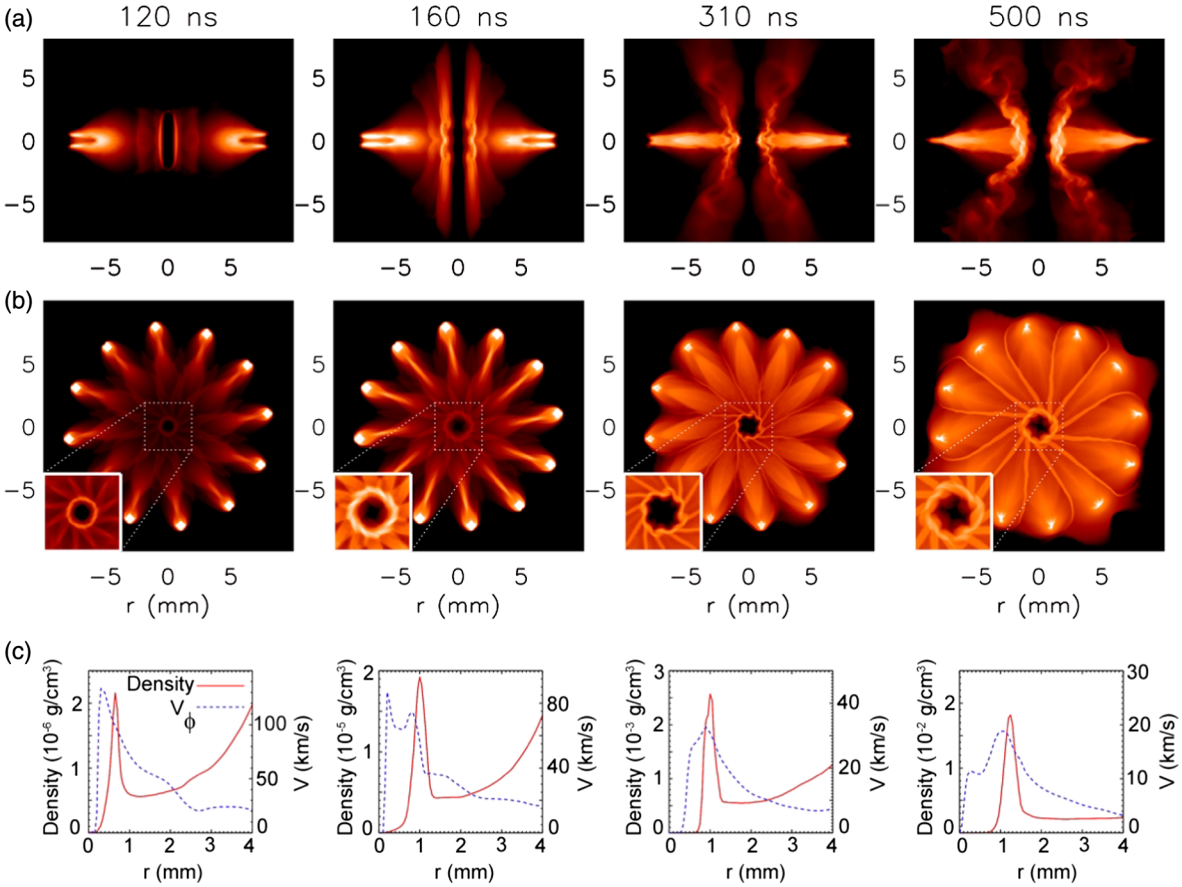

FIG. 32. Results of the reference case simulation of the formation of the rotating plasma disk (50 μm resolution). (a) Time sequence of slices of mass density on the X-Z plane. From left to right: 120, 160, 310, and 500 ns. Only part of the computational domain is shown. The color scale is logarithmic, ranging from 10^{-7} g cm^{-3} (darker tones) to variable levels (lighter tones) to highlight structures. (b) Same as (a) but for the X-Y plane instead. The insets in the bottom left corners are magnified versions of the central region. (c) Time sequences of average radial profiles of density (solid red lines) and toroidal velocities (dashed blue lines). The times are the same as in (a) and (b). From M. Bocchi.

development of anomalous viscosity in this system. Indeed, for Re $\gg 1$ the growth rate of shear-flow instabilities is of the order of $\Gamma \sim v_{\rm rot}/a$ (Landau and Lifshitz, 1987). Thus one revolution time $(2\pi a/v_{\rm rot})$ would provide a significant growth factor $\sim \exp(2\pi\Gamma a/v_{\rm rot}) = \exp(2\pi)$. Given that initial perturbations are large due to the discrete nature of the plasma streams forming the disk, the development of turbulent viscosity should be possible on the time scale of the experiment. It is interesting to note that the value of viscosity required to explain the fast inward material transport observed in this experiment $\nu_{\rm tr} \sim 10^5 \nu_{\rm Sp}$ corresponds to the value of the α parameter in the α prescription ($\nu_{\rm tr} = \alpha C_S H$) of Shakura and Sunyaev (1973) of $\alpha \sim 0.1$.

Although the laboratory experiments investigating accretion disks are in their initial stages, they provide a promising platform for future studies of a number of physical processes affecting real astrophysical accretion disks.

V. ASTROPHYSICS-RELEVANT SHOCKS

Shock waves form naturally in many dynamical astrophysical environments. They appear wherever large energy releases occur or where the supersonic or super-Alfvénic plasma streams collide or meet other obstructions. Shocks effectively convert the flow's kinetic energy into thermal energy and radiation. They are also thought to play an important role in particle acceleration. Pulsed-power techniques provide an excellent opportunity to study the physics of magnetized shocks of astrophysical relevance. In particular, issues related to a number of problems have been explored such as (i) blast waves and radiative precursors, (ii) blast-wave instabilities, (iii) the structure of intrajet shocks, and (iv) the interaction of shocks with obstructions.

A. General comments

Shock waves are an integral part of supersonic hydrodynamical and magnetohydrodynamical flows and appear in a variety of forms, including blast waves following SN explosions, termination shocks formed at transition of supersonic to subsonic expansions, bow shocks forming in the interaction of supersonic flows with impermeable obstructions, and many others. Of particular interest are the effects of radiation on MHD shock structure and shock stability.

Shocks appearing at the tips of astrophysical jets, as well as intrajet shocks (called "working surfaces," Sec. II) caused by the variability of the flow velocity, have been discussed in some detail in Sec. II, as they are an integral part of the jet

physics. Next, we cover broader aspects of astrophysical shocks: blast waves of various kinds, shocks in a magnetic field, and radiative effects in shocks. We also discuss instabilities with a particular emphasis on thermal instabilities of the shocked flow.

In the ideal MHD description, shocks appear as sharp discontinuities in the flow; i.e., the transition width is assumed to be infinitesimal (Landau and Lifshitz, 1984, 1987). In reality the width of the shock transition in density is determined by the particle mean-free path (m.f.p.) and, for the magnetic field, by the resistivity of the medium. If both scales are small compared to the global scale of the flow, then MHD, with shocks included, provides a valid description of the global flow. An example of the situation where such a description is valid are shocks propagating through an expanding supernova material (Arnett, 1996). Plasmas produced in pulsed-power experiments are typically highly collisional, with the m.f.p. significantly shorter than the global dimensions of the flow. Thus pulsed-power experiments deal here with the canonical MHD shocks.

The main dimensionless parameter that characterizes the presence of the shock is the width of the shock transition compared to the global scale of the underlying flow: the former must be much less than the latter. The shock strength is characterized by the Mach number. In the case of flows with significant radiative loss, the cooling time of the shocked material with respect to the hydrodynamic time scale is of significance. In partially ionized gas, the degree of ionization affects the equation of state and thereby a Mach number. These effects and corresponding dimensionless parameters are discussed next in relation to specific types of shocks and corresponding effects.

In astrophysics, one can also meet situations where flows occur in media having a very long m.f.p. An example is a late stage of expansion of supernova remnants into the interstellar medium [see, e.g., images and plasma parameters for the SN 1006 remnant in Ghavamian *et al.* (2002) and Bamba *et al.* (2003)]. In this case, the collisionality of the medium may be reinstated due to the development of microinstabilities of the interpenetrating plasma flows. In this way so-called "collisionless" shock can be formed [see a summary in Sagdeev and Kennel (1991)]. Although the properties of these shocks are somewhat different from the "canonical" collisional shocks (in particular, the concept of the adiabatic index has to be modified), the global structure of the flow will still be similar to that occurring in a collisional medium. The general morphology of the collisionless shocks could then be reproduced in the collisional flows generated in pulsed-power facilities.

There is a significant on-going effort in the generation of collisionless shocks in the lab as well as studies of their internal structure. Many of these experiments are based on laser-generated plasma streams (Fox *et al.*, 2013; Huntington *et al.*, 2015); thus any substantive discussion of these experiments would bring us well beyond the scope of this review.

B. Blast waves and radiative precursors

A blast wave is usually defined as a diverging shocked flow initiated by a sudden energy release in a small initial volume. The ensuing structure then consists of a hot core expanding into the surrounding medium and driving a strong (but gradually weakening) shock. Depending on the density distribution in the ambient medium, there may appear a reverse shock in the hot driver that may be propagating backward toward the center. This reverse shock may have a smaller velocity than the expanding gas and be advected outward. There exist many good tutorials on blast-wave structure and these flows are also described by the well-known Sedov-Taylor self-similar solution (Landau and Lifshitz, 1987).

The Sedov-Taylor solution shows that the matter in front of the shock is compressed to a thin shell that, in the frame of the blastwave, accretes the preshock material. The shell thickness depends on the equation of state of the gas and on the intensity of radiative losses in the case of an optically thin shell. A number of instabilities can develop in the propagating shock, and the presence of small-scale structures is visible in the images of many of the supernova remnants; see Fig. 33 for an example.

The shell may experience ripple instabilities (Vishniac instability) (Vishniac, 1983); a qualitative assessment of those for the Z-pinch setting can be found in Ryutov, Derzon, and Matzen (2000), Eq. (4.32). In the astrophysical environment, the Vishniac instability is important in a number of situations (Ostriker and McKee, 1988).

A complementary (conjugate) configuration of a blast wave is a *converging* strong shock that can be produced by turning on a high pressure on the spherical or cylindrical surface and pushing an imploding shell inward. The physics behind the diverging and converging (imploding) thin shell is similar in many respects, in particular, in the properties of the Vishniac instability as long as perturbations of the scale smaller than the curvature radius are concerned.

Systematic studies of the converging blast waves have been carried out on the Mega Ampere Generator for Plasma

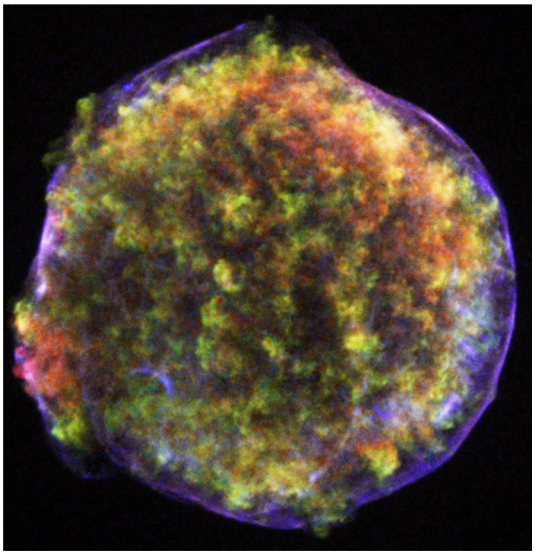

FIG. 33. Tycho's (1572) supernova remnant x-ray image (false colors); Chandra x-ray telescope. The highly structured surface of the blast wave is thought to be a result of a variety of instabilities. NASA/CXC/Rutgers/J.Warren and J. Hughes *et al.*, http://chandra.harvard.edu/photo/2005/tycho/.

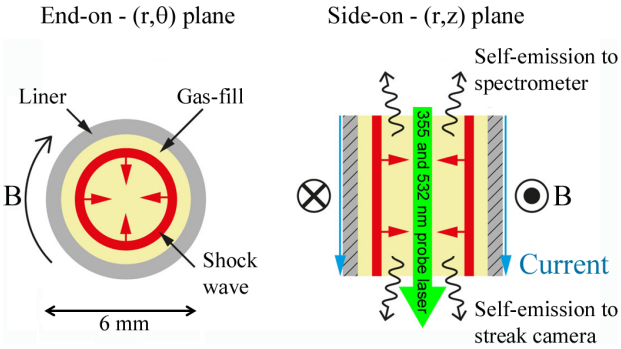

FIG. 34. Schematic of the blast-wave experiment. Note that the liner (shown in gray) is not imploding as a whole; however, its inner surface gives a strong kick to the gas inside, thereby driving a converging blast wave (red). The density distribution during the implosion was found by the end-on interferometry. From Burdiak *et al.*, 2015.

Implosion Experiments (MAGPIE) pulsed-power facility (Imperial College) (Burdiak *et al.*, 2013, 2014, 2015), with Ne, Ar, and Xe. A schematic of one such experiment is shown in Fig. 34. A cylindrical shock was launched from the inner surface of an aluminum cylinder of 5.8 mm inner diameter and 14 mm long. The wall thickness was 0.09 mm. The axial current of 1–1.4 MA caused some inward displacement of the inner surface that pushed the gas and generated a strong converging shock. (Specific details of the processes that caused the inward push are still under study.) The temperature increase at the shock front created a radiation field that could ionize the preshock gas [a radiation precursor; see, e.g., Drake (2006)]. The initial mass density of the gas fill was 1.3×10^{-5} g/cm^3 in all cases. This corresponded to the particle density of 6×10^{16} cm^{-3} for Xe. Given that the atomic collision cross section for Xe is $\sim 10^{-15}$ cm^{-2}, this corresponded to mean-free paths of ~0.15 mm for Xe, so that the anticipated shock thickness was much less than the inner radius of the tube (2.9 mm). The shock velocity was ~20 km/s, so that the postshock temperature reached a few eV. Such temperatures cause partial ionization of the gas and excitation by electron impact. This, in turn, produces a flux of intense ionizing radiation from the shock—a radiative precursor. The ionization states in a shocked region reach $Z \sim 2$.

The electron (and ion) density at the shock transition produced a characteristic peak typical of the blast wave; see Fig. 35(b). Instabilities of the front show up clearly; see Fig. 35(a). The high azimuthal mode number and the localization near the blast wave may indicate the presence of the Vishniac-type instability (Vishniac, 1983), although the thermoradiative instabilities behind the shock are also possible. The measured shock velocity of ~20 km/s corresponds to Mach numbers of $M = 60$ for Ar and $M = 110$ for Xe with respect to the sound speed of nonpreheated gas. However, the significant preheating of the upstream material by the radiation from postshock plasma reduces the Mach number to $M \sim 7$ (Burdiak *et al.*, 2013). The radiative cooling of the postshock plasma is significant: the radiative cooling time of 5–10 ns (Rodriguez *et al.*, 2012) is a factor of 10–20 shorter than the shock propagation time.

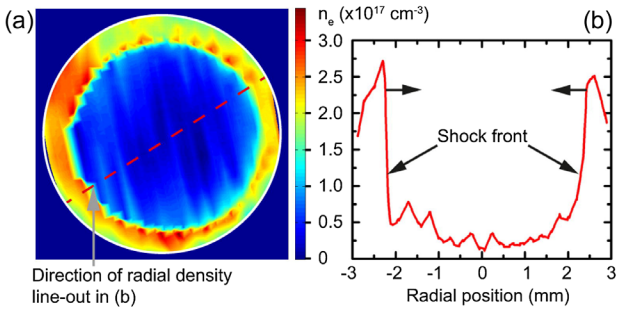

FIG. 35. (a) The electron density distribution reconstructed from the end-on interferometry (Ar, 182 ns after the start of the current pulse). (b) Radial electron density distribution at that time. The radiative precursor extending far beyond the shock transition is clearly visible. From Burdiak *et al.*, 2013.

On larger scales, radiative precursors have been studied on the *Z* facility at Sandia National Laboratories (SNL) (Rochau *et al.*, 2008). The precursor was driven into a CH_2 foam by the imploding inner liner in a nested arrays *Z* pinch. The shock velocity exceeded 250 km/s, and the shocked foam temperature reached 400 eV. Under these conditions, the shock radiated 30–50 GW into the unshocked foam, leading to its ionization prior to the shock arrival. An extensive set of data presented by Rochau *et al.* (2008) allows one to obtain opacity data suitable for benchmarking astrophysical radiative codes against the experiment (Falcon *et al.*, 2015).

C. Shocks in the colliding streams

As was discussed in Secs. II and III, in clumpy jets one can often encounter a situation where one of the later clumps moves faster than the previous one and eventually overtakes it. As the Mach numbers are quite high (especially in the presence of radiative cooling), the Mach number for the relative velocity is also high, and the interaction of colliding clumps leads to a formation of intricate shock structure often referred to as working surfaces (Sec. II); see also Hartigan (2005).

The process of collision of two nonidentical clumps was simulated in a dedicated experiment (Suzuki-Vidal *et al.*, 2015). This was done by investigating the interaction of two counterstreaming plasma jets. The setup shown in Fig. 36 produced currents flowing in the opposite direction in the lower and upper foils. This is a situation where the Hall effect should lead to a difference in the densities and velocities of the two jets (see details in Sec. VI.A). Indeed, the upper jet turned out to be faster and denser than the lower one, thereby creating a desired situation of collisions of two nonidentical jets.

The resulting configuration (Fig. 37), if considered in a reference frame moving with the average jet velocity, is equivalent to the interaction of the faster part of an astrophysical jet catching up with slower moving jet material. The emerging bow shock is initially smooth, but the development of small-scale structures is subsequently observed. The spatial and temporal scales are consistent with those expected for the thermal instabilities, developing at the appropriate slope of the radiative cooling curve. The dimensionless parameters characterizing these experiments are similar to those discussed in Sec. II.D. Suzuki-Vidal *et al.* (2015) discussed the scaling of

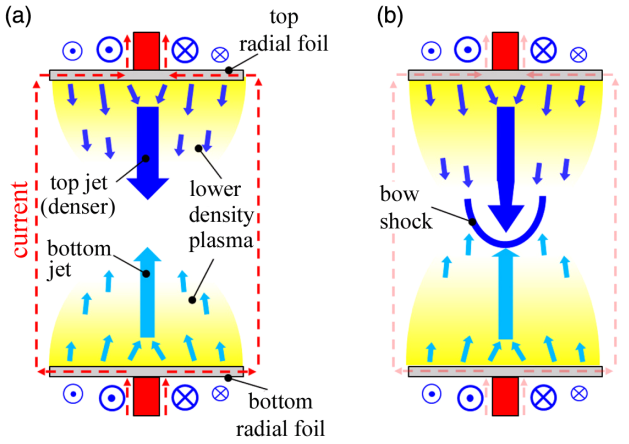

FIG. 36. Schematic of experimental configuration to study the formation of a bow shock from the interaction between two counterstreaming jets with different axial velocities, represented as opposite vertical arrows on axis. The schematic depicts a side-on (radial), cut view of the system, which has azimuthal symmetry. The dashed (red) arrows represent the path of the current that drives the two plasma flows. The (blue) arrows pointing into and out of the page correspond to the azimuthal magnetic field generated by the current, which provides the driving force for the two outflows. The jets are surrounded by lower-density plasma (yellow regions), which moves with the same axial velocity as the jets. Smaller arrows in these regions represent the plasma flow direction. The images depict the two counterstreaming outflows (a) before their collision and (b) after they collide, triggering the formation of a bow shock moving toward the bottom foil. From Suzuki-Vidal *et al.*, 2015.

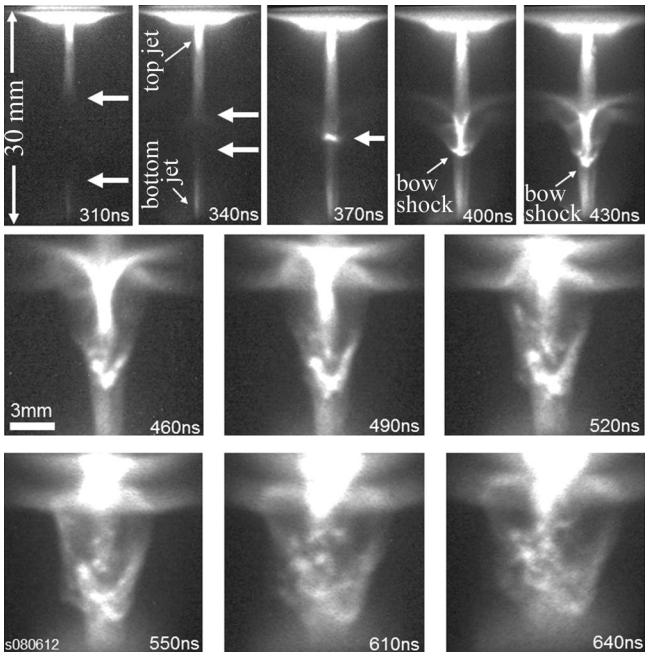

FIG. 37. Counterstreaming jet interaction results from optical self-emission of the plasma obtained from the same experiment. The arrows in the first three frames indicate the position of the tip of both jets (visibility dependent on image contrast levels), with their collision highlighted at 370 ns. The next two frames show the formation of the bow shock. The last six frames are focused on the bow shock region, which is seen to fragment most evidently in the last 3 times. From Suzuki-Vidal *et al.*, 2015.

the observed shock evolution to the conditions of shocks in Herbig-Haro (HH) objects. The temporal scale of the shock fragmentation in these experiments (~30 ns) corresponds to ~15 yr for plasma conditions typical for the shocks in HH objects, while the observed spatial scales (between ~100 μm and ~1 mm) correspond to 3–30 AU. It was noted in this paper that the size of the larger-scale nonuniformities is consistent with the size of the new knots appearing in the HH 1 object (Hartigan *et al.*, 2011).

Experiments with colliding plasma jets in which the jets were produced by two conical wire arrays are reported by Valenzuela *et al.* (2015). These experiments also show the development of clumpy structures, consistent with the development of cooling instabilities in which the cooling time is shorter than the flow dynamical time.

Besides the jets produced in wire arrays and foils, the pulsed-power technique allows for a great variety of other configurations, with other plasma parameters. An interesting example is the interaction of plasma jets formed in the rail guns (Merritt *et al.*, 2014; Moser and Hsu, 2015). Well-collimated plasma streams with velocity of 35–45 km/s, Mach number of 3–10, initial density of $(1–2)\times10^{16}$ cm^{-3}, electron temperature of 1–2 eV, diameter of 5 cm, and length of 20 cm have been produced. The working gas was hydrogen with heavier admixtures of argon and other gases.

Several experiments on the collision of the plasma jets produced by two individual guns were performed. One experiment was made for the geometry where two such jets collided head on in the middle of a large (2.7 m diameter) vacuum chamber, as illustrated in Fig. 38. Because of high directed energy of the ions, the Coulomb collisions between the ions of the two jets correspond initially to a long mean-free path, greatly exceeding the length of either of the jets. However, the friction between the common electron population (in the overlap zone of the two jets) and the streaming ions is very high (Ross *et al.*, 2012). The electrons are then rapidly

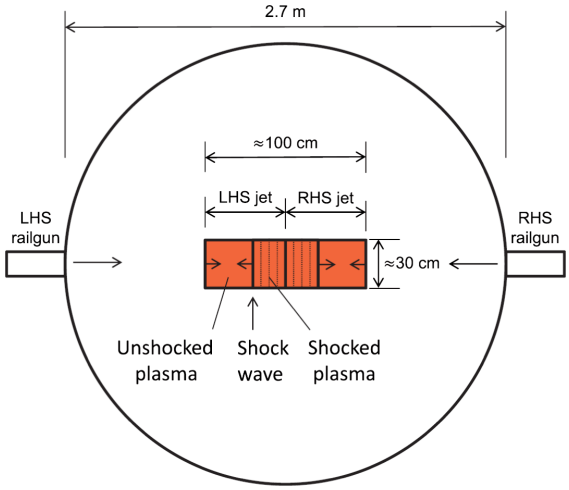

FIG. 38. Schematic of the experiment with two counterpropagating, high Mach number plasma bunches from the right-hand-side (RHS) and the left-hand-side (LHS) rail guns. Note the size of the spherical vacuum chamber (2.7 m in diameter). From Moser and Hsu, 2015.

heated driving sufficient ionization of the initially singly charged ions to the higher Z states. Then, as the ion-ion collision cross section scales as Z^4, the mean-free path becomes low and a rapid braking of the stream occurs. Therefore a transition from initially collisionless interpenetration changes to a strong collisional interaction. In astrophysics this would correspond to the onset of enhanced particle scattering driven by plasma microinstabilities (i.e., formation of shocks in the initially collisionless system).

In another set of experiments Merritt *et al.* (2014) used a different set of ports for injecting the jets creating an oblique collision of the two jets. The relative velocity of ions of the two identical jets was now small due to a small intersection angle and, although the common "parallel" velocity was large, the merging of the jets was collisional and gave rise to the formation of collisional oblique shocks, as illustrated in Fig. 39. We remind the reader that such flows represented some of the earliest models for jet formation in the astrophysical literature (Canto, Tenorio-Tagle, and Rozyczka, 1988).

Similar structures were earlier observed and analyzed by (Swadling *et al.* (2013) in conjunction with the merging of the jets emanating from the wires in wire arrays. In this latter case the spatial scale was in the range of a millimeter, compared to tens of centimeters of Fig. 39. This is one more example of the scalability of hydrodynamic equations (the change of scale by a factor of 30 maintains even the finest features of the flows).

D. Introducing magnetic fields

The presence of the magnetic field adds a new degree of freedom to the dynamic processes occurring in complex plasma flows. Lebedev *et al.* (2014) studied the interaction of a magnetized plasma flow with an obstacle. The schematic of the experiment is shown in Fig. 40. The cylindrically diverging plasma flow is produced in the inverse-pinch configuration discussed earlier (Sec. II.A). The flow carries an azimuthal magnetic field $B_1 \sim 2$ T measured by miniature magnetic probes. Plasma density along vertical lines of sight is measured interferometrically, whereas the flow velocity and temperature of the electrons and ions are measured by Thomson scattering. The parameters of the upstream flow are summarized in Table VIII.

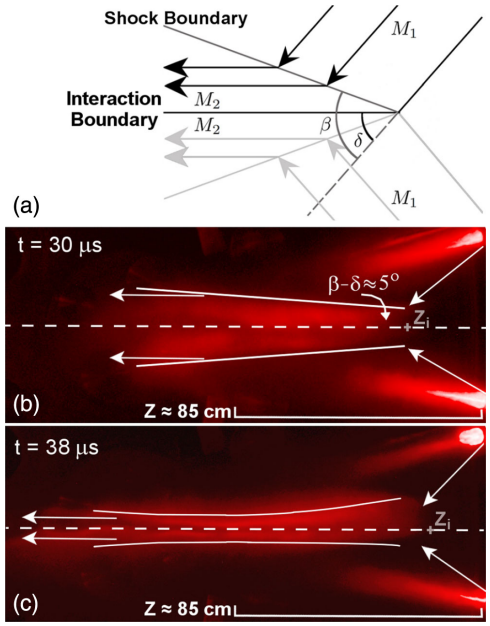

FIG. 39. Oblique merging of the two high-Mach number jets. False-color optical image for two instants of time. The notation is explained in (a). From Merritt *et al.*, 2014.

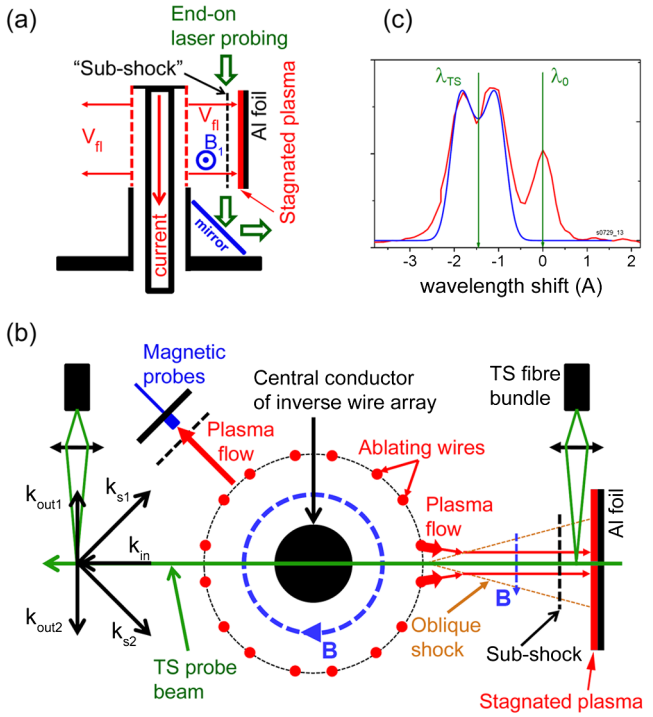

FIG. 40. Schematic of an experiment investigating interaction of a magnetized plasma flow with a planar conducting obstacle (thin Al foil). (a) Side-on and (b) end-on views of the setup and diagnostics. (c) The Doppler shift of the TS spectra measured in the upstream plasma was used to determine plasma flow velocity and temperature. From Lebedev *et al.*, 2014.

This well-diagnosed experiment produced some unanticipated results. When an obstacle in the form of a rectangular aluminum foil (0.5×1 cm^2 or 1×1 cm^2, 17 μm thick) was introduced to the flow, one could anticipate the formation of a reverse shock propagating away from the foil, with parameters determined by MHD shock conditions (Landau and Lifshitz, 1984). In particular, the density should have increased by a factor of 4 or more, depending on the details of the equation of state. Experimentally, however, the density jump did not exceed a factor of 2 (we call this shocklike structure a "subshock"). Other peculiarities of this flow configuration are discussed later.

To understand the flow a parameter called the ion-ion m.f.p. can be evaluated for the directed energy of the incoming ions (~700 eV for the incoming flow). It determines the width of the shock front: the incoming ions get scattered on and "mixed" with the shocked ions at this distance. An estimate in Table VIII is rather crude as it does not account for the density increase behind the shock. Still, it indicates that the collisional shock thickness will be no less than a few millimeters, whereas the distance between the aluminum foil and the subshock is also similar to a few millimeters.

TABLE VIII. Characteristic parameters of the upstream plasma flow in experiments by Lebedev *et al.* (2014). n_e: electron density; T_e: electron temperature; $\bar{Z}$: average ion charge; $V_{\rm fl}$: flow velocity; $\lambda_{\rm ii}$: ion-ion m.f.p.; $\lambda_{{\rm ii}\_v}$: ion-ion m.f.p. for the directed energy[a]; D_M: magnetic diffusivity; M: Mach number; M_A: —Alfvénic Mach number; Re: Reynolds number; Re_M: magnetic Reynolds number.

n_e	T_e	$\bar{Z}$	$V_{\rm fl}$	$\lambda_{\rm ii}$	$\lambda_{{\rm ii}\_v}{}^*$	D_M	M	M_A	Re	Re_M
10^{18} cm^{-3}	20 eV	3	10^7 cm/s	<1 μm	2 cm	3×10^5 cm^2	5	2	10^5	20

[a]See explanations in the text.

Interestingly, the ion gyroradius for the incoming flow in a 2 T magnetic field is ~3–4 mm, so that the magnetic field can affect the formation of the observed transition, e.g., via two-fluid plasma effects; several examples of the importance of two-fluid MHD effects in astrophysical settings were given by Kurlsrud *et al.* (1997), Königl (2010), and Gregori *et al.* (2012). We note that experiment is also relevant to on-going discussion of the relation and transition between the collisional and collisionless effects in shock formation (Ross *et al.*, 2017).

E. Interaction of magnetized streams with clumps and globules

The interaction of supersonic flows with clumps of various nature is of significant interest for astrophysics (Klein, McKee, and Colella, 1994, Hartquist and Dyson, 1996, Jones, Ryu, and Tregillis, 1996, Hartigan, 2005, Yirak, Frank, and Cunningham, 2010). In particular, the issue of clump destruction processes by shear-flow instabilities is still an active area of research. Some experiments based on the use of high-power lasers have been performed (Klein *et al.*, 2003, Poludnenko *et al.*, 2004, Hansen *et al.*, 2017), but with no magnetic field. Astrophysical flows are, however, likely to carry significant embedded magnetic fields. Pulsed-power techniques allow one to simulate both the effect of a magnetic field and radiation on the flow-clump interaction. This can be done via converging or diverging, magnetized plasma streams produced by a standard or an inverse wire array (see Sec. II). In this way the first experiments on flows around small obstacles were recently carried out.

Ampleford *et al.* (2010) investigated the formation of bow shocks in experiments where the plasma stream was produced in the standard Z-pinch configuration and propagated inward. This flow then collided with wires of a target array (Al, 15 μm diameter) positioned inside the main, ablating wire array (Fig. 41). The current in each wire of the inner array could be varied and made sufficiently large to create a dynamically significant magnetic field of up to ~40 T. The flow of Al plasma with $Z\sim5$, $n_e\sim3\times10^{18}$ cm^{-3}, and velocity of $V=1.5\times10^7$ cm/s emerging from the outer array collided with the inner array and produced a set of intersecting bow shocks. The dimensionless parameters characterizing the bow shock formation in these experiments are $M=4$–12, $M_A=1$–5, $\beta=0.1$–5, and $\mathrm{Re}_M=4$–10 (Ampleford *et al.*, 2010). Reduction of the current (magnetic field) in the inner array resulted in the smaller apparent size of the obstruction, indicating that the magnetic field is an essential factor in the formation of the shock structure. Transition from Al wires to W wires in the outer array caused a significant decrease of the Mach angle compatible with increased radiation losses.

This work also included a detailed and, in general, favorable comparison of the experimental results with simulations by numerical code GORGON (Chittenden *et al.*, 2004, Ciardi *et al.*, 2007), widely used for the simulation of astrophysics-related experiments on pulsed-power devices.

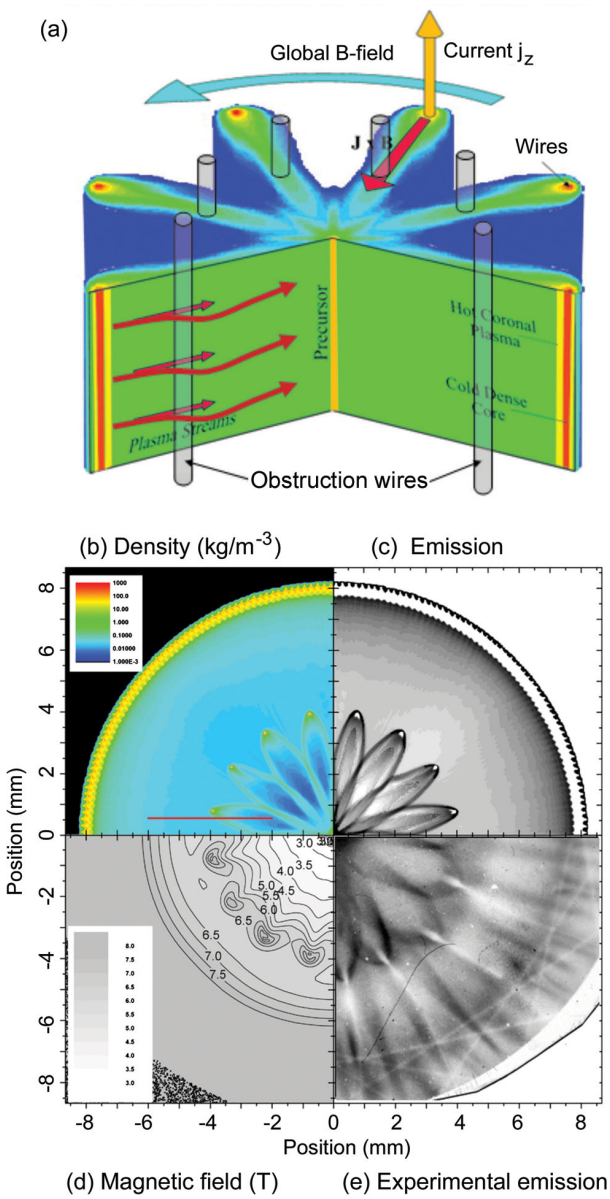

FIG. 41. (a) MHD simulations showing density distribution of ablation streams inside a cylindrical wire array and positions of obstacles for formation of bow shocks. (b) Simulated maps of density, (c) XUV emission, (d) magnetic field, and (e) emission map recorded in experiment. From Ampleford *et al.*, 2010.

An example of such a comparison is presented in Fig. 41 for the case of plasma flow from Al wires. The simulations reasonably well reproduced the formation of the bow shocks around the wires of the target array, including the dependence of the shock angle on the strength of radiative cooling. However, the experimentally observed angles of the bow shocks were a factor of ∼2 larger than those found in the simulations. The reasons for this discrepancy were not further investigated in that paper, in part due to the difficulties in obtaining detailed measurements of the plasma parameters of the incoming plasma and of the formed shocks, as the diagnostic access in this setup was limited to probing only along the axial direction.

Significantly improved diagnostic access, allowing more detailed characterization of the bow shock formation and evolution, was achieved using plasma flows from "inverse wire array" Z-pinch configurations, similar to those shown in Fig. 40.

The experiments of Bott-Suzuki *et al.* (2015), based on the pulsed-power generator XP at Cornell University, generated currents of 260 kA (Kalantar, 1993). Since the current was relatively low in these studies they used an array made of only two wires. Each wire (made of tungsten) then produced a plasma stream propagating radially, away from the central post, and carried with it a magnetic field embedded in the flow in the vicinity of the wire. The stream was, therefore, interacting with an obstruction made of another wire (Al, 25 μm diameter), bent in such a way as to allow unhindered diagnostic access along the z axis. The characteristic flow parameters in these studies were temperature $T \sim 15$ eV, flow velocity $V \sim 10^7$ cm/s, average charge state $Z \sim 10$ ($A = 184$), and electron density $n_e \sim 10^{18}$ cm^{-3}. The magnetic field carried by the flow and measured in the absence of the obstruction (i.e., in the undisturbed flow) was ∼5 T at the point where the obstruction would be inserted. A picture of the bow shock shrouding the obstruction was obtained by end-on interferometry [Fig. 42(a)]. Gated pinhole images show the shock transition as a narrow but strong emitter of the hard UV, compatible with the anticipated postshock temperature of ∼50 eV. The presence of a diffuse emission region in front of the shock transition may be a sign of a radiative precursor, similar to that seen in Fig. 35.

Interestingly, the width of the shock transition—determined by the collisions of the incoming ions with the slower ions of the postshock plasma—is rather large. Indeed, the upstream tungsten ions have the energy of 9 keV, so that the shock width is at a scale of a few mm, quite large compared to the obstruction diameter. The ion charge state in the shocked material may have become higher than 10 thus increasing the ion-ion Coulomb cross section and making the width consistent with the observations.

The magnetic diffusivity for a $Z = 10$, $T = 15$ eV plasma is $D_M = 6 \times 10^5$ cm^2/s. For a flow velocity of $V = 10^7$ cm/s, this would correspond to a penetration distance δ of the shock-compressed magnetic field into the upstream region $\delta \sim D_M/\mathrm{V} \sim 0.6$ mm. Even for the higher temperature of the shocked plasma ($T \sim 50$ eV) the magnetic diffusivity remains high, $\sim 10^5$ cm^2/s, so that δ stays well beyond the wire diameter. As the size of the obstruction is much smaller than δ,

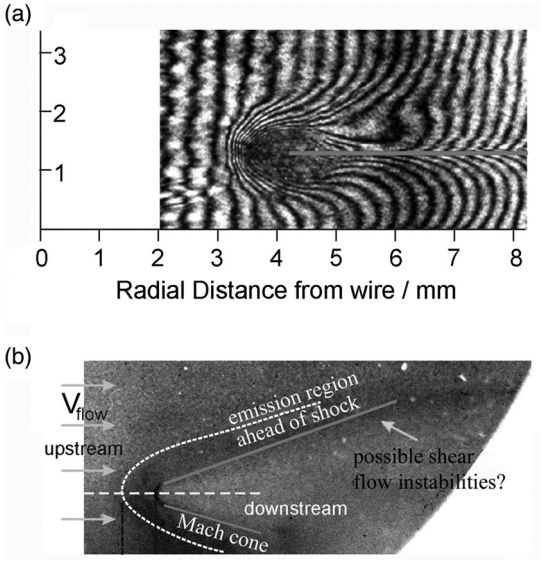

FIG. 42. (a) Interferometric image of the flow around the cylindrical obstruction placed at 4 mm from the plasma source; (b) a gated pinhole image of the same structure in the extreme UV range $h\nu > 80$ eV. From Bott-Suzuki *et al.*, 2015.

it is hard to imagine a strong compression of the magnetic field behind the shock. In other words, the magnetic field in the shock transition stays at its preshock level. It may still play a role in setting the shock structure, as the electrons, heated to ∼50 eV behind the shock, start to become magnetized even by this relatively weak field, $\lambda_{ei} \sim 7$ μm, $\rho_e \sim 5$ μm, and the electron heat conduction is suppressed.

The experiment of Burdiak *et al.* (2017) investigated how the level of magnetic field pileup at an obstacle affects the structure of bow shocks. Supersonic plasma flow ($M_S = V_{\mathrm{flow}}/C_S = 5$, $M_A = V_{\mathrm{flow}}/v_A = 2$–$2.5$), produced with an inverse wire array setup, is similar to what is shown in Fig. 40. This flow interacted with conducting cylindrical obstacles oriented parallel or perpendicular to the magnetic field which was frozen ($\mathrm{Re}_M = 20$) into the plasma flow. It was found that both the orientation and the conductivity of the obstacles significantly affected the shape of the bow shock and the stand-off distance from the obstacles; see Fig. 43. For cylindrical obstacles oriented along the magnetic field [Figs. 43(a) and 43(c)], the measured angle of the bow shock was consistent with the fast-magnetosonic Mach number of the plasma flow. The presence of magnetic field has been seen to be affecting the plasma compressibility. The stand-off distance in this case was, however, small due to the limited pileup of the magnetic field at the obstacle. Both the plasma and B field were able to slip past the small-diameter obstacle. For the parallel orientation of the B field (with respect to the obstacle axis) both the shock curvature radius and the stand-off distance were much larger [Figs. 43(b) and 43(d)], indicating a significant pileup and draping of field lines over the obstacle.

The setup and diagnostics used in this experiment allowed detailed measurements of the bow shock structure and plasma parameters. These included spatially resolved measurements of flow velocities and plasma temperatures via Thomson scattering diagnostics, measurements of the density

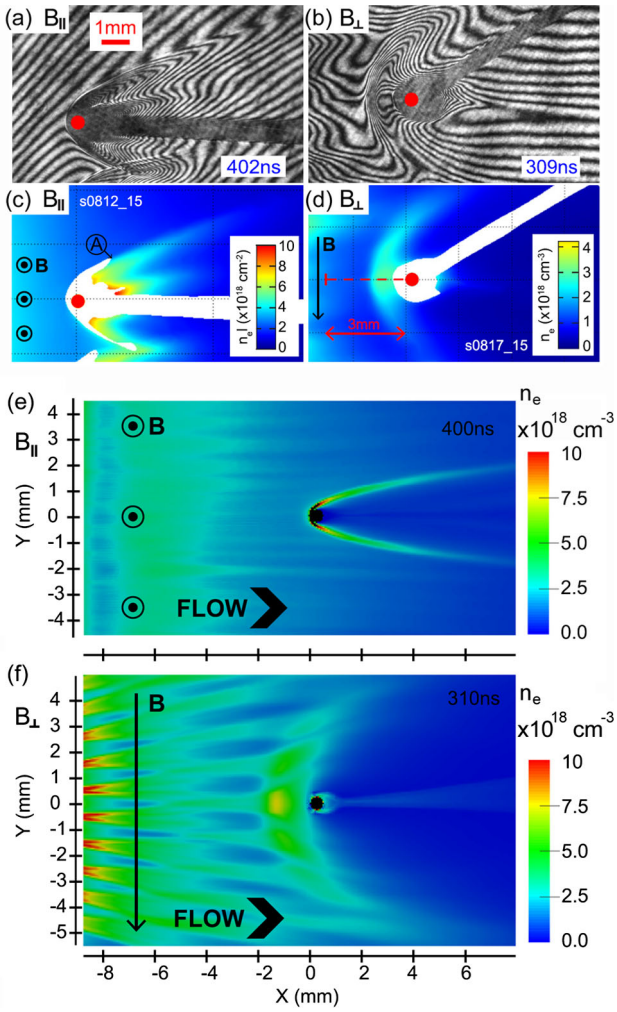

FIG. 43. (a), (b) Interferometric images of bow shocks formed around cylindrical obstacles (red spots indicate diameter and position of the obstacles) and (c), (d) derived electron density maps of the flows with magnetic field oriented (a), (c) parallel and (b), (d) perpendicular to the obstacles. (e), (f) 2D electron density slices from 3D GORGON MHD simulations for parallel and perpendicular orientations, respectively. From Burdiak *et al.*, 2017.

distributions with intereferometry, and the magnetic field with miniature magnetic probes. From these measurements detailed comparisons of the experimental results with 3D resistive MHD simulations performed with the GORGON code (Chittenden *et al.*, 2004, Ciardi *et al.*, 2007) could be carried out. For the $B_{\parallel}$ case, the simulations [Fig. 43(e)] reproduced the history of the shock formation observed in the experiments, including the small values of the shock opening angle and the small stand-off distance. For the $B_{\perp}$ case, however, the simulations did not reproduce the initial stages of the shock formation. In simulations the shock is first formed at the obstacle surface, as would be expected for an MHD shock, and then gradually moves away from the obstacle due to pileup of the advected magnetic flux. In experiments, the shock in this time-dependent flow was formed not at the obstacle, but at a large (~1.5 mm) stand-off distance from the obstacle via a gradual steepening of the density perturbation. At the start of the interaction the ion-ion m.f.p. is large and the streaming ion flow is quite collisionless, and therefore one should not expect an MHD model to fully capture the formation dynamics. Instead the initial interaction is governed by two-fluid plasma effects, when the magnetized electrons are decelerated by the piled-up magnetic field while the nonmagnetized ions are decelerated by the cross-shock electric field. The thickness of the layer where the decoupling of the electron and ion velocities is possible is the ion-inertial length ($c/\omega_{\rm pi}$). The value of the ion-inertial length agrees well with the stand-off distance of the shock at the formation time. We note that despite not being able to correctly reproduce the initial phases of the shock formation, the MHD modeling reproduces well the structure of the shock for the later times; see Fig. 43(f).

VI. NON-MHD EFFECTS

In this section we go beyond the single-fluid magnetohydrodynamics and discuss two astrophysically relevant extensions. The first is the Hall effect which is significant in objects such as astrophysical shocks and stellar flares. The second is the generation of fast particles by the disruption of the current-carrying plasma columns. We conclude with a discussion of astrophysical systems where such effects can take place and consider their scaling to laboratory experiments.

A. Hall effect

In some cases of astrophysical significance a magnetohydrodynamical description requires a refinement that would amend MHD equations with terms accounting for the Hall effect. This effect appears in two-fluid MHD (Braginski, 1965), which has separate equations for the mass, momentum, and energy of both electron and ion components of the plasma. The Hall effect stems from the electron momentum equation, which reads

$$0 = -\nabla p_e - en_e(\boldsymbol{E} + \boldsymbol{v}_e \times \boldsymbol{B}) + \boldsymbol{F}_{\rm ei}. \tag{6.1}$$

Here p_e, n_e, and $\boldsymbol{v}_e$ are the electron pressure, particle density, and velocity, respectively, and $\boldsymbol{F}_{\rm ei}$ is a friction force between the electrons and ions. The latter is, in particular, responsible for the plasma resistivity. In Eq. (6.1) we neglected the electron inertia due to the small electron mass.

In the absence of the electron pressure gradient and electron-ion friction, Eq. (6.1) becomes a familiar line-tying equation, $\boldsymbol{E} + \boldsymbol{v}_e \times \boldsymbol{B} = 0$. Note however an important qualification, the magnetic field, is line tied to the *electron* fluid.

One can express $\boldsymbol{v}_e$ in terms of the mass velocity $\boldsymbol{v}$ of the plasma, which to a high accuracy is equal to the ion velocity $\boldsymbol{v}_i$, and the plasma current $\boldsymbol{j}$. To do that, one uses an expression for the current density, $\boldsymbol{j} = en_e(\boldsymbol{v}_i - \boldsymbol{v}_e)$, solves it for $\boldsymbol{v}_e$, and substitutes the latter into Eq. (6.1), with the understanding that $\boldsymbol{v}_i \approx \boldsymbol{v}$. The result reads

$$\boldsymbol{E} + \boldsymbol{v} \times \boldsymbol{B} = \frac{\boldsymbol{j} \times \boldsymbol{B}}{en_e} + \frac{\boldsymbol{F}_{\rm ei}}{en_e} - \frac{\nabla p_e}{en_e}. \tag{6.2}$$

We assume that the plasma is quasineutral. In the case of one ion species with a charge Z, the quasineutrality constraint

implies $n_i = n_e/Z$. The electron-ion friction force can be expressed in terms of the plasma current density $\boldsymbol{F}_{\rm ei} = en_e\boldsymbol{j}/\sigma$, where σ is the electrical conductivity.

For a medium at rest and without a pressure gradient one finds the following textbook relation describing the Hall effect in a resting conducting medium (such as solid metal):

$$\boldsymbol{j} = \sigma\left(\boldsymbol{E} - \frac{\boldsymbol{j}\times\boldsymbol{B}}{en_e}\right). \tag{6.3}$$

This equation indicates that if an electric field is applied to a solid conductor immersed in a magnetic field, the current generated will acquire a component flowing perpendicularly to the electric field—a textbook setting for the Hall effect.

In an environment of a conducting medium experiencing a complex and sometimes turbulent motion, the Hall effect may acquire new significance. As mentioned, in terms of MHD problems, the change brought about by this effect comes from the fact that the magnetic field is frozen into electron fluid, whose velocity may differ from the mass velocity at sufficiently high-current density. If this is the case, the magnetic field interacts with the mass flow differently compared to a single-fluid MHD, where the right-hand side of Eq. (6.2) is dropped and the magnetic field is advected with hydrodynamic velocity.

We focus here on fully ionized plasmas, where the role of neutral particles in the plasma dynamics and magnetic field evolution is negligible. In a weakly ionized plasma one needs to consider the dynamics of all three components (electrons, ions, and neutral atoms), this leading to a variety of additional effects. For example, the friction of gravitationally unstable, collapsing molecular clumps against magnetically supported ionized gas may play a significant role in star formation (Mckee and Zweibel, 1992; Zweibel, 2002), and the Hall effect may contribute to this process (Tassis and Mouschovias, 2004; Wardle, 2004; Bai, 2014). The presence of a neutral component in these problems means a low temperature of the plasma and makes it difficult to simulate them in pulsed-power experiments. So, we next consider only the case where the neutral density is negligible.

The difference between velocities of the two components $\boldsymbol{u}$ can be expressed in terms of the current density $\boldsymbol{u} = \boldsymbol{v}_e - \boldsymbol{v} = -\boldsymbol{j}/n_e e$. It is convenient to characterize the role of the Hall effect by the dimensionless parameter Ha, "the Hall number," that indicates by how much the velocities of the two plasma components differ,

$$\mathrm{Ha} \equiv u/v = j/n_e e v. \tag{6.4}$$

One can express it in terms of the characteristic values of the magnetic field B and the spatial scale of the system L. From the equation $\nabla\times\boldsymbol{B} = \mu_0\boldsymbol{j}$, we get $j \sim B/\mu_0 L$, so that

$$\mathrm{Ha} = B/\mu_0 n_e e v L. \tag{6.5}$$

One sees that favorable conditions for the observation of the Hall effect include small spatial scales, low densities, and slow hydrodynamic motions.

TABLE IX. Comparison of the characteristic parameters of laboratory and astrophysical pinches.

Parameter	Laboratory	Astrophysical
Aspect ratio ξ	10–20	10–20
Pinch radius a (cm)	0.1	10^{17}
Magnetic field B(G)	10^6	10^{-6}
Plasma density n (cm^{-3})	10^{22}	10^{-3}
Pinch current I (MA)	1	10^6
Alfvén velocity v_A (cm/s)	3×10^6	6×10^6
Evolution time τ (s)	3×10^{-8}	10^{10}
Electron beam energy W_e (keV)	300	10^9

Because of very large spatial scales of the astrophysical systems, the Hall number is typically very small for them. As an example, one can take the inferred parameters of a typical Herbig-Haro outflow (Reipurth *et al.*, 2002): $B \sim 10^{-7}$ T, $n_e \sim 10^{-9}$ m^{-3}, $L \sim 10^{15}$ m, and $v \sim 10^6$ m/s (see Table IX). This yields the Hall number of 6×10^{-10}. However, the Hall parameter can be large in the systems such as astrophysical MHD shocks, where the small spatial scale is associated with the shock thickness. The Hall effect is significant in the space environment as well as in environments such as the solar wind and its interaction with the Earth's magnetosphere (Xu *et al.*, 2015).

An interesting feature of the Hall effect is that it breaks the symmetry properties of a single-fluid MHD. Equations of single-fluid MHD allow for the transformation $\boldsymbol{B}\to-\boldsymbol{B}$, $\boldsymbol{v}\to\boldsymbol{v}$, or, similarly, $\boldsymbol{j}\to-\boldsymbol{j}$, $\boldsymbol{v}\to\boldsymbol{v}$. This means, in particular, that if one changes polarity of electrodes, the system evolves in exactly the same manner as for the initial polarity, just the signs of the current and the magnetic field change. On the other hand, if the Hall effect is present, this symmetry breaks down: the evolution of two systems of different polarity differs substantially.

The polarity effect was tested experimentally by Gourdain and Seyler (2013) in the radial foil configuration (cf. Sec. III). The heating of the foil by a high current causes the appearance of the plasma on the outer side of the foil. This plasma intercepts part of the radial current and gets accelerated in the upward direction. The current sheath moves upward, with the current closing through a central column.

When the "normal" polarity was reversed (with the central post becoming an anode), the jet parameters experienced detectable changes (Gourdain and Seyler, 2013): the jet became more collimated near the axis and faster than in the normal polarity. This is interpreted as a result of the sign change of the Hall contribution to the radial current: in the normal case, it is directed oppositely to the radial current formed due to plasma inertia. In the reverse case the currents add up, increasing the upward "push." This is illustrated in Fig. 44. The characteristic plasma parameters that define the value of the Hall number (6.5) were (Gourdain and Seyler, 2013, 2014) $n_e = 5\times10^{19}$ cm^{-3}, $L = 2\times10^{-2}$ cm, $B = 10^5$ G, and $v = 10^7$ cm/s. This yields a modest value of $\mathrm{Ha}\sim1/15$, sufficient to detect the difference between two cases.

In problems where one considers turbulent dynamos and amplification of initially very weak magnetic fields, the Hall

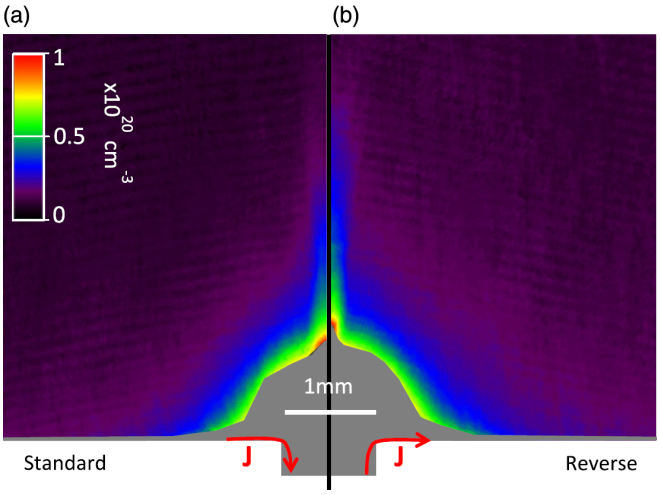

FIG. 44. Density distribution of the jets generated in experiments by Gourdain and Seyler. This figure is a combination of two "halves": the left one is the left half of the density distribution in the normal polarity, whereas the right is the right half in the reverse polarity. The results are obtained by the Abel inversion of interferometric column densities. From Gourdain and Seyler, 2013.

effect is negligible, and the polarity effect does not show up. In other words, a given turbulent velocity field will enhance in the same way initial magnetic fields of opposite polarity. Thus, if one wants to see effects of the broken symmetry, one has to assume that the magnetic field is sufficiently strong from the outset. On the other hand, there exists an observationally proven correlation between the vector of angular velocity of the active galactic nuclei accretion disk and the Faraday rotation measure, making the Hall effect one of the potential explanations (Königl, 2010).

The polarity effect was demonstrated in a very graphic form by Suzuki-Vidal *et al.* (2015), where two oppositely directed jets were driven in exactly the same configurations, but with opposite polarities, in conjunction with the bow shock experiment (see Sec. V.C).

In the laboratory experiments there exist other polarity effects, not related to the Hall effect. In particular, if an experiment includes interfaces between plasmas and condensed matter, the electron or ion emission from the interface may significantly depend on the polarity. A significant polarity effect was observed by Bland *et al.* (2005), where the experimental design allowed one to see the effect of the *radial* electric field polarity on the performance of the wire array. This circumstance may obscure the presence of the Hall effect.

B. Generation of energetic particles

It has long been understood that in astrophysical environments there may exist natural sources of localized current channels driven by the motion of conducting medium with embedded (possibly, self-generated) magnetic fields. Examples where these currents would naturally appear include stellar atmospheres, stellar outflows, accretion disks, and giant planets (Severnyi, 1959; Hardee, 1982; Trubnikov, 1992; Szego *et al.*, 2015). These currents may experience disruptions caused by the development of various instabilities, in particular, the sausage and kink instabilities driven by the combination of Rayleigh-Taylor and field-line curvature mechanisms. Particularly interesting is the sausage instability that causes the formation of narrow necks in the current channel, and corresponding increase of the current density that may lead to a rapid growth of kinetic instabilities, the onset of high anomalous resistance, and corresponding spikes in the voltage across the neck. Note that this mechanism is different from the Fermi-like acceleration occurring outside the current channel, in the cocoon area of the tower jets and described in Sec. III.B. Here we have acceleration occurring right at the neck, with a combination of direct, one step beam acceleration and, possibly, electromagnetic microturbulence leading to the fast formation of the ion tail in the neck area (not considered here).

The plausibility of this chain of events became clear in an extensive set of laboratory studies using Z pinches, plasma foci, and X pinches (Pikuz, Shelkovenko, and Hammer, 2015a, 2015b). Although not motivated by astrophysical connections, these studies revealed effects that could be of relevance to astrophysics: the formation of energetic, nonthermal ion populations, and the generation of particle beams. Among the most important manifestations of such processes may be the conjectured current disruptions in filamentary structures (Trubnikov, 1990) observed near the center of our Galaxy [depicted in Fig. 3 of the Introduction of Yusef-Zadeh, Morris, and Chance (1984)].

In the remaining part of this section, we briefly summarize the experimental findings relevant to fast particle formation in current disruptions. We then discuss (still tentative) theoretical models for this process and speculate about the scaling of these results to their possible astrophysical counterparts. We emphasize again that this is a different mechanism from the one discussed in Sec. III.B.

We base our discussion on recent publications on the subject (Bakshaev *et al.*, 2014; Klir *et al.*, 2016; Shelkovenko *et al.*, 2016), which contains an extensive list of the earlier papers. Information on the ion distribution function was obtained mostly via the neutron measurements in deuterium discharges (Klir *et al.*, 2016). The ion spectrum and its anisotropy were related to neutron time-of-flight measurements along multiple chords. By fitting the power spectrum of deuterons to the observed neutron spectrum, they concluded that the neutron data can be explained by the time-integrated deuteron energy spectrum of the form const$/E^n$ with n being 2.5–3. The anisotropy was related to the orbit effect of the deuterons moving along the pinch in an azimuthal magnetic field [Fig. 1 in Haines (1983) and Fig. 10 in Bakshaev *et al.* (2014)]: for isotropic ion population near the axis, the larger fraction would leave the constriction toward the cathode than toward the anode. The characteristic "temperature" of these deuterons was ~10 keV.

In addition to the main group of the ions, there can be generated also much higher-energy ions, forming a weakly diverging stream detected at the cathode by the use of a radiochromic film (Klir *et al.*, 2016). The ion energy in this stream reached tens of MeV.

Alongside the fast ions, fast electrons are also formed in the pinched plasma, with the energies exceeding 300 keV, thereby approaching the relativistic domain. The most recent results as

well as the earlier references are presented by Shelkovenko *et al.* (2016).

In all cases, the formation of high-energy ion tails and electron beams was correlated with the formation of "hot spots" near the constrictions of the axial current. Note also that, despite high plasma density in the constrictions, the mean-free paths of fast particles (ions, electrons) were much greater than the constriction size. This indicates that the collisionless description of the formation process may be adequate.

The appearance of fast particles in pulsed-power devices, and the astrophysical significance of this effect has recently gained attention from the research community. We note a recent study (Takezaki *et al.*, 2016), where fast ions were formed in the interaction of plasma flow generated in a plasma focus device, with a perpendicular magnetic field and indicating one more mechanism of fast ion formation that may have astrophysical relevance.

C. Energetic electrons produced by current disruptions and conjectured scaling

In this section we discuss a specific model of the fast particles generation by the "necking" effect and attempt to scale the experimentally observed characteristics of the fast particles to the corresponding characteristics in the analogous astrophysical systems. Despite the presence of many uncertainties, this exercise may serve as a useful template for similar future studies based on more detailed analyses.

When the constriction starts to develop, as shown in the schematic form in Fig. 45, the total current within a column remains almost constant due to a high inductance. The azimuthal magnetic field in the constriction area must therefore increase. Ions are heated due to compression and their pressure increases to match the increased magnetic pressure. They are pushed out of the constriction zone along the axis (both ways). It is not certain what limits the width of the neck from below.

As the current remains constant, the shrinking of the neck radius leads in parallel to an increase of the relative velocity u of the electrons and ions. When u exceeds a threshold for the development of microinstabilities of ion-acoustic and/or lower-hybrid type, the microfluctuations cause enhanced scattering of the electrons and may lead to a rapid growth of the anomalous plasma resistivity (Ryutov, Derzon, and Matzen, 2000). To sustain the current, the electric field increases, reaching a runaway threshold for the electrons on axis. The electrons may form a beam with the energy $\sim eEa$ in the direction of the anode. The combination of these effects creates a complex and not yet fully understood picture.

To relate laboratory observation to possible astrophysical counterparts, we assume that the underlying physics of the laboratory and astrophysical pinches and their disruptions is the same. In particular, we assume that the shrinking of the constriction occurs with a nonrelativistic velocity (i.e., $v_A < c$), as is the case in the laboratory experiments. Accordingly, we can extend our similarity consideration only to those astrophysical phenomena where $v_A < c$. This does not mean that we cannot have relativistic electron beams formed in the neck, as these beams still do not change the overall nonrelativistic evolution of the constriction zone, and the energy taken away by relativistic electrons is small.

The acceleration mechanism discussed in this section is directly related to the formation of very high electric fields and the rapid collapse of a constriction. This is the situation usually met in the laboratory experiments with Z and X pinches and plasma foci. In the astrophysical tower jets, as well as in their laboratory counterparts, additional mechanisms can work for the ion acceleration related to a long wandering of the ions in the magnetic field outside the central jet but inside the return current shroud (see Sec. III.B). Here the acceleration will be a gradual Fermi-like one and may lead to the formation of long ion tails (Sec. III.B). This should favor ion acceleration as the ions go through a longer nonrelativistic phase, which the electrons may not survive due to their much stronger attachment to the field lines and a rapid loss through a "leaky" magnetic field prior to reaching relativistic energies. Direct electron acceleration by the enormous inductive voltage in the disrupting current-carrying column may contribute to the appearance of highly relativistic electrons observed in a number of astrophysical sources.

The pinch length l will be assumed significantly larger than its radius, and the processes in the constriction can be characterized by the length scale a (Fig. 45) related to the constriction size. The ratio $\xi = l/a \gg 1$ will be called an aspect ratio. The time can be measured in the units of the Alfvénic time a/v_A. As we are not going to develop a comprehensive theory model, but rather use the experimentally determined energy of fast electrons to scale it to the corresponding values in an astrophysical problem, we can skip the numerical coefficients in the scaling relations that follow.

The time scales will be related as the Alfvénic time scales, so that

$$\tau_{\text{astro}} = \tau_{\text{lab}} \frac{(B/a\sqrt{n})_{\text{lab}}}{(B/a\sqrt{n})_{\text{astro}}}. \tag{6.6}$$

Now we consider the energy of accelerated electrons. Inductive accelerating voltage U appears with the onset of the anomalous resistance and resulting rapid current decrease:

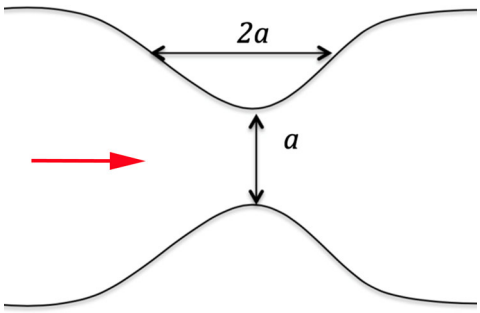

FIG. 45. Geometry of constriction. Effects of particle heating and acceleration occur predominantly in the zone of the neck with the length comparable to its diameter. The hot ions are ejected both ways, whereas the electron (ion) beam is directed toward the anode (cathode) situated far to the left and right and not shown in the figure. The red arrow shows direction of the current flow. The characteristic evolutionary time of the constriction is $\tau \sim a/v_A$, where the Alfvén velocity v_A is evaluated for the magnetic field and plasma density in the neck area.

$$U \sim L\Delta I/\tau \equiv LI(\Delta I/I)(1/\tau), \tag{6.7}$$

where L is the inductance of the column. One has

$$\frac{L_{\rm astro}}{L_{\rm lab}} = \frac{(a\xi)_{\rm astro}}{(a\xi)_{\rm lab}}. \tag{6.8}$$

We also present the following equation for the pinch current:

$$I_{\rm astro} = I_{\rm lab}\frac{(aB)_{\rm astro}}{(aB)_{\rm lab}}. \tag{6.9}$$

There are two dimensionless parameters that characterize both systems. Those are the aspect ratio ξ and the current drop $\Delta I/I$. Combining Eqs. (6.6)–(6.10), we find scaling for the energy $W_e = eU$ of the electron beam generated at the constriction:

$$\frac{(W_e)_{\rm astro}}{(W_e)_{\rm lab}} = \frac{(aB^2/\sqrt{n})_{\rm astro}}{(aB^2/\sqrt{n})_{\rm lab}}\frac{\xi_{\rm astro}}{\xi_{\rm lab}}\frac{(\Delta I/I)_{\rm astro}}{(\Delta I/I)_{\rm lab}} = \frac{(aB^2/\sqrt{n})_{\rm astro}}{(aB^2/\sqrt{n})_{\rm lab}}. \tag{6.10}$$

We assumed that the relative current drop $\Delta I/I$ and aspect ratio ξ are the same for both systems. If the identification of the acceleration mechanism is correct, then the assumption of the same relative current drop in the pinch columns with the same aspect ratio is natural. We emphasize that this is an assumption.

The laboratory experiments allow one to verify the scaling (6.10) by comparing the energies of accelerated electrons between pinches of various currents and plasma densities. This would offer an experimental test of the scaling. We are not aware of such experimental comparisons made to this date.

To get some impression of the parameters involved, we present in Table IX a comparison of some generic midsize pinch and a plasma jets described by Reipurth *et al.* (2002) and visible in the lower part of Fig. 1.

If the scalings presented above can be supported by a more thorough analysis, one can predict that the pinches associated with currents flowing along the central part of a young star jet may serve as a source of synchrotron radiation by the GeV-range electrons.

VII. MAGNETIC RECONNECTION

Magnetic reconnection is one of the most basic processes affecting many astrophysical phenomena. Pulsed-power devices open up the possibility to study this process in collisional resistive plasmas in well-characterized environments. After a brief general introduction we describe the first steps in the development of relevant experimental platforms.

Magnetic reconnection is a phenomenon by which the global topology of the magnetic field can be changed by localized redistribution of the electric current. The idea of reconnection can be traced back to ground-breaking works by Parker (1957) and Dungey (1958); in a cartoon form, it is illustrated by Fig. 46.

Imagine two magnetic flux tubes as shown in Fig. 46(a) immersed in an ambient plasma and initially separated by some distance in the direction normal to the figure. Imagine then that the motion of the ambient plasma brings the tubes closer in this direction, and they "touch" each other. Then, in the contact zone, the components of the magnetic field directed oppositely to each other would annihilate, and the configuration would change to that shown in Fig. 46(b). Remarkably, the local rearrangement of the field in a contact zone leads to a global change of the topology: points 1 and 2 that were not initially connected along the magnetic field lines become connected. This global change may give rise to a number of secondary processes. In particular, the electron heat conductivity between points 1 and 2 takes the parallel form. The other important consequence is that the field tension causes a "sling-shot" effect and may lead to straightening of the flux tubes. This cartoon picture may actually be realized in the stellar convective zones. In other settings, in particular, in the solar corona, the geometry may be more complex.

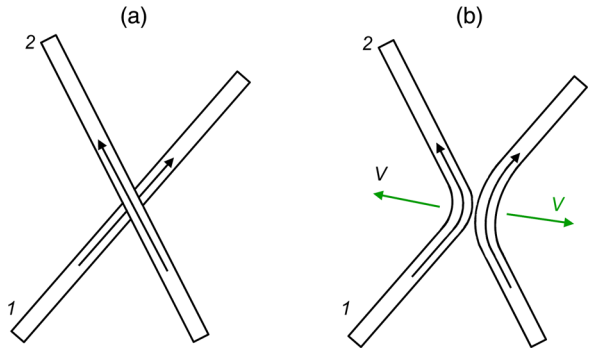

FIG. 46. Magnetic reconnection of two magnetic flux tubes immersed in an ambient slowly moving plasma.

Besides its ability to change the topology of the system, magnetic reconnection can also occur very rapidly, on time scales much shorter than the resistive diffusion time in the initial configuration. In a number of situations, the reconnection process involves small spatial scales associated with collisionless instabilities driven by the plasma current. The plasma turbulence that starts at the largest-scale magnetic islands, produced by the resistive tearing instability (Furth, Killeen, and Rosenbluth, 1963), cascades to scales as small as the anomalous skin depth (Drake, Shay, and Swisdak, 2008; Yamada, Kulsrud, and Ji, 2010; Yamada, Yoo, and Myers, 2016).

Magnetic reconnection is a mechanism underlying solar and stellar flares and is thought to be a significant player in a number of astrophysical phenomena: accretion disks; the interaction between accretion disks and the central object, in determining the thermal balance of the interstellar gas, and as an injection mechanism for particle acceleration (Zweibel and Yamada, 2009, and references therein).

In the case where initial plasma pressure is small compared to the magnetic pressure ($\beta \ll 1$)—a case typical, for example, in the solar flares—the magnetic field initially has a nearly force-free geometry and the plasma current is almost exactly parallel to the magnetic field. In this case the rapid dissipation of the magnetic field causes strong plasma heating, so that plasma pressure in the reconnection zone becomes comparable to the magnetic pressure. In the simplest geometry that is often used in the physics analyses of reconnection, one starts

with a planar situation where the field has initially only a z component, the current has only a y component, and all the parameters depend only on x. An array of instabilities then can occur starting from purely resistive tearing modes and going down to various current-driven collisionless microinstabilities.

In a more realistic version, one may have a situation where there is a uniform "guiding" magnetic field in the z direction and, overlaid with it, a "reconnecting component" that is directed along y and changes sign as a function of x (being, say, positive at $x > 0$ and negative at $x < 0$). Here the reconnection would release only the energy of the reconnecting component (Furth, Killeen, and Rosenbluth, 1963; Drake, Shay, and Swisdak, 2008; Zweibel and Yamada, 2009; Yamada, Kulsrud, and Ji, 2010; Yamada, Yoo, and Myers, 2016).

Studies of magnetic reconnection in a $\beta \ll 1$ plasma are best suited for magnetic confinement devices. In these devices one can create and control magnetic configurations in the regimes where the plasma manifests its collisionless properties. The efficacy of this approach has been demonstrated, in particular, in experiments of the Princeton Plasma Physics Laboratory group (Yamada, Kulsrud, and Ji, 2010; Yamada, Yoo, and Myers, 2016).

But reconnection effects may also be important in $\beta \geq 1$ plasmas. These are likely to be quite common in many astrophysical settings where flows dominate the energetics but the fields can still play important roles. In these cases, the plasma heating becomes a subdominant effect, but there still remain two other important effects: (1) change of the magnetic topology and (2) dissipation of magnetic energy leading to slowing down and even destroying the magnetic dynamo. Z pinches could naturally create plasmas of high beta and high collisionality and therefore open up a window to the processes not easily covered by the magnetic confinement facilities. High-beta reconnection regimes have also been produced with high-power lasers (Nilson *et al.*, 2006; Fiksel *et al.*, 2014; Rosenberg *et al.*, 2015).

In considering laboratory studies and astrophysical phenomena, it is important to note that magnetic reconnection is a multifaceted phenomenon involving a tremendous range of scales, from global scales (thousands of kilometers in the stellar convective zones and parsecs in galactic accretion disks) to microscopic scales as small as micrometers (anomalous skin depth) in stellar interiors. The global scales are described by the MHD equations, whereas the processes in the reconnection zones are described by small-scale, sometimes kinetic, instabilities. One can introduce a large number of dimensionless parameters characterizing the relative role of all these processes. The most basic ones are the plasma beta and the plasma collisionality characterized by the ratio of the ion skin depth to the ion mean-free path. For one particular example these are shown in Table X.

Next we focus on what pulsed-power facilities have contributed and can contribute to *collisional* reconnection studies. An example comes from an experimental platform (Suttle *et al.*, 2016, 2018; Hare *et al.*, 2017a, 2017b, 2018) based on the use of the MAGPIE pulsed-power facility. This platform offers significant flexibility in controlling the parameters of the inflowing magnetized plasma flows. It also offers the opportunity to vary the dimensionless parameters characterizing the reconnection process, such as the Lundquist number ($S = \mu_0 L v_A/\eta$) and plasma β.

The overall experimental setup is shown in Fig. 47; the details will be discussed later in this section. The basic element of this experiment is the generation of a cylindrically diverging, magnetized plasma flow using the inverse wire array Z-pinch configuration (discussed in Sec. II.A). The magnetic reconnection setup involves two inverse arrays positioned side by side and driven in parallel by a 1.4 MA, 500 ns current pulse. The arrays produce radially divergent plasma flows which advect azimuthal magnetic fields. When the flows collide between the two arrays, the magnetic fields they carry are antiparallel and magnetic reconnection occurs with formation of a long-lasting current sheet in which the magnetic field is annihilated. The 2D magnetic reconnection configuration that forms is sustained in a quasistationary state by incoming plasma flows for more than 20 hydrodynamic crossing times.

This system manifests a number of interesting features briefly discussed later and has been thoroughly characterized by a variety of diagnostics which provided detailed measurements of all of the key plasma parameters. Thomson scattering was used to measure spatial variations of the directed flow velocities, as well as the ion and electron temperatures. The magnetic field distribution in the reconnection plane was evaluated by laser polarimetry. The line-integrated density was obtained by the imaging laser interferometry, as illustrated in Figs. 47(b) and 47(c). As particle mean-free paths are much shorter than the global scale of the experiment, one can use the hydrodynamic picture of the flow. In the geometry of Fig. 47, the plasmas come along the x axis from the left and right to interact in the y-z plane, where the radial flow stagnates. The plasma then flows out predominantly along the y direction, and some plasma expansion can also occur in the z direction at the top and the bottom edges of the reconnection layer.

For further discussion, we present in Table X some important characteristics of the plasma in a reconnection layer formed from Al or carbon plasma flows, including the derived dimensionless reconnection parameters. These characteristics change in space and time; the numbers given in the table roughly correspond to a central point of the layer at $t = 215$ ns.

The formation of the reconnection layer in Al and C plasmas has many features which are common for both materials: the layer thickness is comparable to the ion skin depth ($\delta/d_i \sim 1$); the incoming plasma flows are redirected and accelerated in the y direction to velocities $V_y > v_A$; the plasma is strongly heated, and the ion temperature significantly exceeds both the electron temperature ($T_i \sim ZT_e$, with $Z = 6$–7) and the kinetic energy of the incoming ions. Measurements show that the conversion of the magnetic energy provides a significant contribution to the overall energy balance, ~50% for carbon (Hare *et al.*, 2017a). The mechanism responsible for the preferential ion heating in these experiments is still under investigation. The observed relation between the electron and the ion temperatures in the reconnection layer $T_i \sim ZT_e$ and the large "current" drift velocity, comparable to the ion sound speed, suggests that the

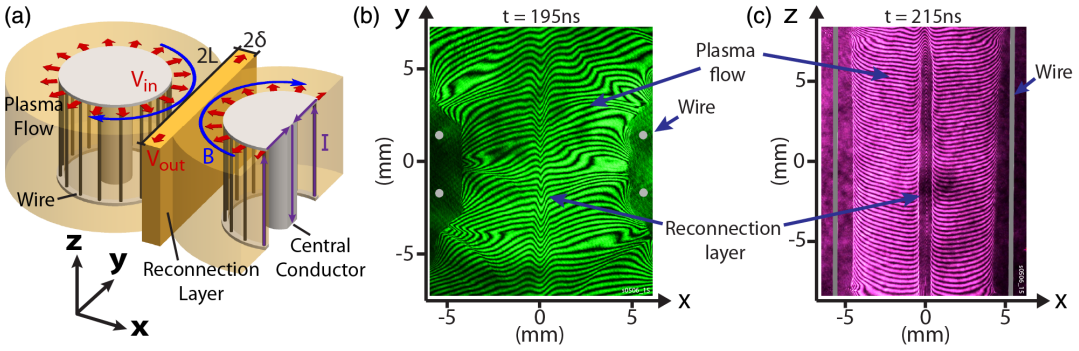

FIG. 47. (a) Experimental configuration of the reconnection experiment (with cut away in the right wire array to show the current path). The current is applied in parallel to the two inverse wire arrays, producing magnetized plasma flows which collide to create a reconnection layer. Raw interferometry images of the reconnection layer along the (b) z direction and along the (c) y direction. In this figure, we use a Cartesian coordinate system shown in (a) with the origin in the midpoint of the annihilation layer. From Suttle *et al.*, 2018.

kinetic plasma effects could be responsible for the heating. The spatially resolved measurements of the plasma velocity and temperatures performed with Thomson scattering (Fig. 48), combined with polarimetry measurements of the distribution of the magnetic field (similar to Fig. 49), allow calculation of the electric field in the reconnection layer (Fig. 48). For steady-state resistive MHD reconnection, the variation of the convective electric field ($V_x \times B_y$) should be balanced by the variation in the resistive term ($\eta_{\mathrm{Sp}} J_z$). Measurements show, however, that the resistive component with Spitzer-Braginskii resistivity is a factor of ~10 smaller than necessary to support the reconnecting electric field.

There are also important differences in the behaviors of the reconnection layers formed in Al and C plasmas, arising from the differences in the inflow parameters (Mach numbers) and in the radiative cooling rates. First, the inflows are super-Alfvénic ($M_A = 2.5$) for Al, but sub-Alfvénic for carbon ($M_A = 0.7$). The stagnation of the Al flows lead to formation

TABLE X. Characteristic plasma parameters in the magnetic reconnection layer. From Hare *et al.*, 2018 and Suttle *et al.*, 2018.

Parameter	Symbol	Carbon plasma ($A = 6$, $Z = 6$)	Aluminum plasma ($A = 27$, $Z = 7$)
Physical parameters			
Electron density (cm^{-3})	n_e	6×10^{17}	1×10^{18}
Electron temperature (eV)	T_e	100	40
Ion temperature (eV)	T_i	600	300
Magnetic field (T)	B_0	3	2
Layer half length (mm)	L	7	7
Layer half thickness (mm)	δ	0.6	0.3
Inflow velocity (km/s)	V_0	50	50
Outflow velocity (km/s)	V_{out}	130	100
Derived plasma parameters			
Alfvén speed (km/s)	v_A	70	20
Sound speed (km/s)	C_S	85	45
Ion skin depth (mm)	$d_i = c/\omega_{pi}$	0.4	0.35
Ion-ion m.f.p. (mm)	λ_{ii}	3×10^{-3}	3×10^{-3}
Electron-ion energy equilibration time (ns)	$\tau_{\mathrm{ei}}{}^{(E)}$	140	40
Radiative cooling time (ns)	τ_{rad}	600	5
Magnetic diffusivity (cm^2/s)	D_M	10^4	5×10^4
Electron-ion relative velocity (km/s)	$u_e = B_0/\mu_0 \delta e n_e$	40	30
Dimensionless parameters			
Lundquist number	S	120	10
Inflow thermal beta	$\beta_{\mathrm{th}} = 2\mu_0 p/B_0^2$	0.4	1
Dynamic beta	$\beta_{\mathrm{dyn}} = 2\mu_0 \rho V^2/B_0^2$	1	10
Mach number	$M_A = V_0/v_A$	0.7	2.5
Dimensionless layer thickness	δ/d_i	1.5	0.85
Ion skin depth to ion-ion m.f.p. ratio	$d_i/\lambda_{\mathrm{ii}}$	130	110
Dimensionless layer length	L/δ	>10	>20

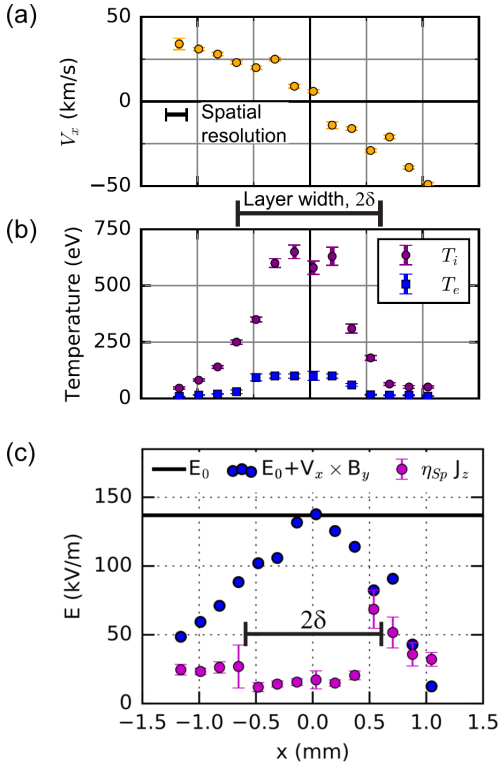

FIG. 48. Spatial profiles of the (a) inflow velocity and the (b) electron and ion temperatures measured by Thomson scattering in the reconnection layer for carbon plasma. (c) Components of the reconnecting electric field. From Hare *et al.*, 2017b.

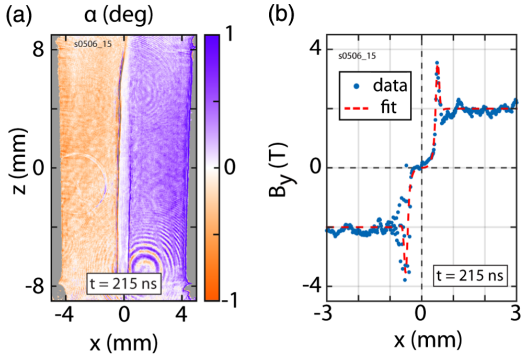

FIG. 49. The (a) measured Faraday rotation angle and the (b) reconstructed profile of the y component of the magnetic field, showing a pileup of the magnetic field at the boundary of the reconnection layer. From Suttle *et al.*, 2018.

of two shocks whose separation sets the thickness of the hot plasma zone. Polarimetry measurements of magnetic field distribution (presented in Fig. 49) show an increase (pileup) of field at the layer boundary by a factor of 2 with respect to the field in the incoming flow and a rapid decrease of field in the layer consistent with magnetic flux annihilation. Secondly, there is a significant difference in the importance of radiative cooling of plasma in the reconnection layer. Cooling is significant for Al ($\tau_{\rm rad} \sim 5$ ns), but negligible for carbon ($\tau_{\rm rad} \sim 600$ ns). As a result, much higher electron temperatures were observed in the case of carbon ($T_e = 100$ eV for C versus 40 eV for Al), with a corresponding increase of the Lundquist number to $S = 120$ compared with ∼10 in Al.

Measurements of the layer structure in the reconnection (x-y) plane showed that it is fairly uniform and steady in the case of Al, but highly unstable in the case of C. In the latter case the layer rapidly breaks up into a chain of plasmoids which are visible in the electron density maps (Fig. 50) and in multiframe self-emission images (Hare *et al.*, 2017a). Measurements with miniature magnetic probes (Hare *et al.*, 2018) also indicate the presence of an O-point magnetic field structure as expected in a plasmoid. It is interesting to note that plasmoids in these experiments were observed at a relatively small Lundquist number of $S \sim 100$. This is however consistent with theoretical predictions for the semicollisional regime of plasmoid instability (Comisso *et al.*, 2016; Loureiro and Uzdensky, 2016), including the observed number of plasmoids and the characteristic growth time of the instability.

As Table X shows, the plasma in this experiment is strongly collisional with the ion mean-free path being shorter than their gyroradius and the electron mean-free path being comparable with their gyroradius. This means that the platform used is suitable for the reconnection studies in the poorly explored regimes of high plasma collisionality. In particular, a significant contribution of unmagnetized (i.e., strong) Nernst effect may eventually become identifiable.

In general, highly collisional reconnection regimes are of significant interest for magnetic field generation in stellar convective zones [e.g., see Sec. V in Ryutov (2015)], where the collisionless effects are absent, but filamentation (tearing) instabilities (Furth, Killeen, and Rosenbluth, 1963) are still possible and may interfere with dynamo activity (Loureiro and Boldyrev, 2017). Direct observations of reconnection processes in stellar interiors are not possible and experimental results characterizing reconnection under such conditions would be helpful for benchmarking codes describing such

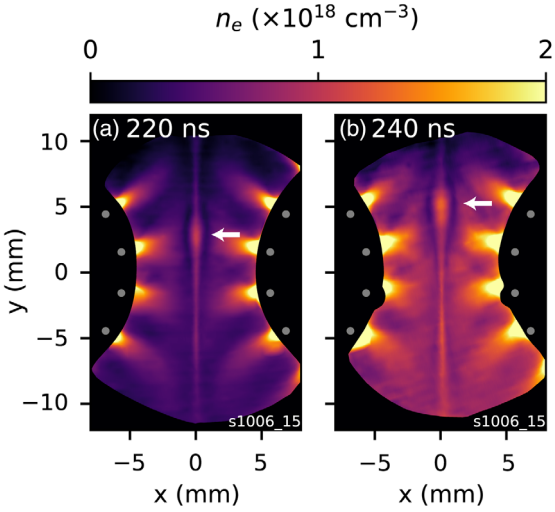

FIG. 50. Electron density maps obtained from laser interferometry (in the x-y plane) in the same experiment with a delay of 20 ns, showing a reconnection layer at $x = 0$ which extends across the entire field of view. Arrows indicate a plasmoid moving in the $+y$ direction with velocity $V_y = 130$ km/s. From Hare *et al.*, 2018.

phenomena. Table X illustrates the level of detailed information available on plasma parameters in experiments, which together with the information on the formation and evolution of spatial structures in the reconnection layer, can be used for comparison with simulations. The relevant information regarding the tearing modes may also be obtained in experiments with thin metal foils with magnetic fields having opposite directions on the two sides of the foil (Zier *et al.*, 2012). In this setting one should eliminate contamination from magneto-Rayleigh-Taylor instability, which can develop if the fields on the opposite sides of the foil are not quite equal in magnitude.

VIII. SUMMARY AND OUTLOOK

This review discusses achievements made in the area of experimental modeling of dynamical astrophysical phenomena via pulsed-power techniques. The merit of these techniques is their capability to produce well-controlled plasma flows of desired geometries: jets, diverging or converging blast waves, rotating plasma disks, or combinations of these structures. One of the advantages of pulsed-power techniques is their intrinsic ability to introduce and control magnetic fields in the system. Plasma parameters can be controlled to change the plasma collisionality, the role of radiation, and ionization degree. Such control allows researchers to tailor the experiment in the best way for studying specific astrophysical phenomena. One characteristic example is the study of magnetic-tower jets (Sec. III), where experimental studies provide support for the plausibility of models discussed in the astrophysical literature. Both the general morphology and dynamical characteristics of magnetic-tower jets have now been reproduced in experiments. Other similar examples are discussed in this review.

In astrophysical environments hydrodynamic flows typically have very high Reynolds numbers. These are well in excess of the Reynolds numbers accessible in numerical simulations and limited by the numerical viscosity. Pulsed-power experiments allow researchers to, at least partially, bridge this gap. They allow one to reach Reynolds numbers of the order of 10^5, thereby providing necessary conditions for entering regimes with developed, high Re turbulence. The magnetic Reynolds number that characterizes the entraining of the magnetic field by the plasma flow ranges in the pulsed-power experiments from a few tens to a few hundreds, allowing access to the early stages of the field evolution in a turbulent plasma.

Progress in developing dedicated diagnostic instrumentation has opened up the possibility of resolving fine structures appearing within global flows: turbulent vortices [see, e.g., Fig. 15(c)], multiple closely spaced shocks [see, e.g., Fig. 9(b)], and magnetic reconnection current sheets (see, e.g., Fig. 50). These features are often not resolved in astrophysical images and their role is inferred only through MHD simulations. The scaled laboratory counterparts described in our review allow one to make direct comparisons between the numerical and real flows that have been experimentally produced and characterized in the laboratory.

As was recognized early in the laboratory astrophysics studies, hydrodynamic flows with subdominant dissipative processes allow scaling over a tremendous range of spatial and temporal scales, provided the hydrodynamic description holds over this whole range. The similarity (called Euler similarity, see a summary in the Appendix) is dynamical, i.e., it covers the whole spatiotemporal evolution of the system from some initial state, onward for several dynamical times. In this regard the Euler similarity is different from the similarities sometimes used to find the scaling of some particular characteristics of the system (say, the friction force acting on the body, or the plasma confinement time in the fusion confinement experiments). In the Euler similarity we deal with the *entire dynamical process*. Importantly, the shocks and turbulence are covered by the Euler similarity as well. This critical similarity holds for the MHD flows too allowing one to make meaningful comparisons between astrophysical systems and their laboratory counterparts, including the presence of shocks.

Interestingly, Euler similarity may manifest itself in comparing two *laboratory experiments* of different scales. An example was discussed in Sec. V.C, where very similar shock structures were observed in two experiments with the global scales differing by 2–3 orders of magnitude (∼1 m vs ∼1 mm). This (albeit unintended) synergy between laboratory experiments of disparate spatial scales provides additional support to the soundness of the general concept of scaling astrophysical structures to manageable laboratory models.

A promising development of recent years is the generation of an analog of an accretion disk, where a rotating plasma disk is contained in the radial direction by the ram pressure of the incoming flow. The images of these disks reveal a rapid inward plasma transport occurring on time scales much faster than classical diffusion time, possibly indicating the development of turbulent viscosity.

The generation of fast, suprathermal particles is a feature manifested by a number of pulsed-power facilities, most notably, Z pinches. Particles with the energies orders of magnitude greater than applied voltages have been observed in such experiments for decades. It is believed that their generation is related to disruptions of the pinch current by the sausage and kink instabilities, although details of related particle acceleration processes have not been fully understood.

A recent development in this area is an experimental detection of high-energy ions in tower jets (Sec. III.B). The ion energy reaches here 3 MeV, way above the values usually observed in Z pinches and attributed, as mentioned, to the ion compression in the necking area. We speculate that these ions get to high energy as they are confined in a larger magnetic structure of the tower jet and experience the second- or first-order Fermi acceleration when bouncing in the whole cocoon.

Pulsed-power facilities with relatively dense and cold plasmas may offer an excellent platform for studies of resistive reconnection not involving development of microturbulence, anomalous resistivity, and nonfluid effects. These regimes, beside their conceptual importance, may be the only ones available in the stellar convective zones where plasma becomes nearly nonideal and the standard separation of scales between collisionless and collisional processes loses its relevance. Such reconnection can still be fast, accelerated by the development of the hydrodynamic turbulence on the

appropriate scales [cf. the plasmoid model, see, e.g., Loureiro and Uzdensky (2016)].

The results summarized in this review have mostly been obtained on modest pulsed-power facilities that can be deployed in university-scale laboratories. The multiplicity of these facilities made possible a rapid progress and cross-checking of the results. The key factor that is also within the reach of the university laboratories is development and fielding of novel, inventive diagnostics. We anticipate a continuous flow of physics information needed for the development of comprehensive models of astrophysical phenomena and a strengthening of the interaction between astrophysicists and practitioners of pulsed-power experiments.

ACKNOWLEDGMENTS

We acknowledge many helpful discussions with D. J. Ampleford, S. N. Bland, G. C. Burdiak, J. P. Chittenden, A. Ciardi, R. P. Drake, M. G. Haines (deceased), G. N. Hall, J. D. Hare, P. Hartigan, A. J. Harvey-Thompson, L. A. Pickworth, T. Ray, B. A. Remington, L. G. Suttle, F. Suzuki-Vidal, and G. F. Swadling. S. L. and A. F. acknowledge support by the DOE Award No. DE-SC-0001063. S. L. acknowledges support by EPSRC Grant No. EP/N013379/1 and by the DOE Award No. DE-F03-02NA00057. D. R. is grateful to Imperial College (London) for its kind hospitality during D. R.'s visit in the fall of 2016. Work at Lawrence Livermore National Laboratory was performed under the auspices of the U.S. Department of Energy under Contract No. DE-AC52 07NA27344.

APPENDIX: SIMILARITY CONSIDERATIONS

When establishing connections between a laboratory experiment and its astrophysical counterpart a natural question arises as to how one relates phenomena occurring on the enormous spatial and temporal scales of astrophysical objects to their laboratory models with the size of less than a centimeter and a time scale of less than a microsecond. In discussing this issue we focus on hydrodynamical and magnetohydrodynamical phenomena.

There is a large number of publications on scaling techniques and among them comprehensive texts by Bridgman (1963), Barenblatt (1979), Sedov (1993), and Durst (2007). In conjunction with laboratory astrophysics these issues were discussed by Arnett (2000), Ryutov and Remington (2002), Koepke (2008), and Hartigan *et al.* (2009).

It goes without saying that, to build a meaningful laboratory experiment, one needs to have at least a general idea of the processes governing the observed natural phenomena. Then one can attempt to build a laboratory model replicating the same processes. Pulsed-power technology is most suitable for imitating effects governed by MHD, hence the focus on this class of effects in our review.

An ability of the laboratory experiment to reach a morphological similarity with astrophysical images is encouraging and helpful: it signifies the correct identification of the underlying processes. (To be more precise, attaining a morphological similarity is a necessary condition for the correct identification.)

In what follows in this Appendix we present a summary of similarity issues for the MHD systems. We present a brief outline of the general approach and refer the interested reader to the publications containing more detailed analyses.

The similarity conditions for the hydrodynamical and magnetohydrodynamical phenomena were reviewed by Ryutov, Drake, and Remington (2000) and Ryutov and Remington (2002). Here we present a brief summary of a so-called Euler similarity. We start from a set of ideal MHD equations for a polytropic gas,

$$\frac{\partial \rho}{\partial t} + \nabla \cdot \rho \boldsymbol{v} = 0, \tag{A1}$$

$$\rho\left(\frac{\partial \boldsymbol{v}}{\partial t} + \boldsymbol{v} \cdot \nabla \boldsymbol{v}\right) = -\nabla p - \frac{\boldsymbol{B} \times \nabla \times \boldsymbol{B}}{\mu}, \tag{A2}$$

$$\frac{\partial \boldsymbol{B}}{\partial t} = \nabla \times \boldsymbol{v} \times \boldsymbol{B}, \tag{A3}$$

$$\frac{\partial p}{\partial t} + \boldsymbol{v} \cdot \nabla p = -\gamma p \nabla \cdot \boldsymbol{v}, \tag{A4}$$

where ρ and $\boldsymbol{v}$ are mass density and velocity, p is the pressure, and $\boldsymbol{B}$ is the magnetic field. There are no dissipative processes included in these equations (no viscosity, heat conductivity, and electrical resistivity); the role of dissipative processes is discussed later in this Appendix. The composition here is assumed to be uniform. MHD shocks with the standard relations between the downstream and upstream parameters on the shock transitions are allowed (Ryutov, Drake, and Remington, 2000).

Initial conditions for the set of equations (A1)–(A4) read

$$\rho_{t=0} = \rho^* f\left(\frac{\boldsymbol{r}}{L^*}\right), \qquad p_{t=0} = p^* g\left(\frac{\boldsymbol{r}}{L^*}\right),$$
$$\boldsymbol{v}_{t=0} = v^* \boldsymbol{h}\left(\frac{\boldsymbol{r}}{L^*}\right), \qquad \boldsymbol{B}_{t=0} = B^* \boldsymbol{k}\left(\frac{\boldsymbol{r}}{L^*}\right). \tag{A5}$$

We present them in a way suitable for subsequent use in dimensionless form. In particular, L^* is a characteristic scale of the problem, and ρ^* is a characteristic density. The function f is dimensionless and characterizes initial shape of the density distribution. The same relates to the rest of the initial conditions in Eq. (A5).

One can now introduce dimensionless representation of the set (A1)–(A4) by normalizing the variables $(\boldsymbol{r}, t)$ and unknown functions $(\rho, \boldsymbol{v}, p, \boldsymbol{B})$ using the same set of scale parameters:

$$\boldsymbol{r}' = \boldsymbol{r}/L^*, \qquad t' = t\sqrt{p^*/\rho^*}/L, \qquad \rho' = \rho/\rho^*,$$
$$p' = p/p^*, \qquad \boldsymbol{v}' = \boldsymbol{v}\sqrt{\rho^*/p^*}, \qquad \boldsymbol{B}' = \boldsymbol{B}/\sqrt{\mu p^*}. \tag{A6}$$

Substituting these relations into Eqs. (A1)–(A4) we reduce the governing equations to dimensionless form:

$$\frac{\partial \rho'}{\partial t'} + \nabla' \cdot \rho' \boldsymbol{v}' = 0,$$
$$\rho' \left(\frac{\partial \boldsymbol{v}'}{\partial t'} + \boldsymbol{v}' \cdot \nabla' \boldsymbol{v}' \right) = -\nabla' p' - \boldsymbol{B}' \times \nabla' \times \boldsymbol{B}',$$
$$\frac{\partial \boldsymbol{B}'}{\partial t'} = \nabla' \times \boldsymbol{v}' \times \boldsymbol{B}',$$
$$\frac{\partial p'}{\partial t'} + \boldsymbol{v}' \cdot \nabla' p' = -\gamma p' \nabla \cdot \boldsymbol{v}'. \tag{A7}$$

Likewise, the initial conditions (A6) become

$$\rho'_{t=0} = f(\boldsymbol{r}'), \qquad p'_{t=0} = g(\boldsymbol{r}'),$$
$$\boldsymbol{v}'_{t=0} = v^* \boldsymbol{h}(\boldsymbol{r}'), \qquad \boldsymbol{B}'_{t=0} = \sqrt{2/\beta}\boldsymbol{k}(\boldsymbol{r}'), \tag{A8}$$

where

$$\mathrm{Eu} \equiv v^* \sqrt{\rho^*/p^*}, \qquad \beta = 2\mu p^*/B^{*2} \tag{A9}$$

are two dimensionless parameters characterizing the problem.

The usefulness of this approach is in its universality: the set of dynamical equations (A7) does not contain any parameters characterizing the initial state. If the initial state in the simulation experiment has been chosen so as to have the initial state to be geometrically similar to that of the natural one [i.e., the functions f, g, $\boldsymbol{h}$, and $\boldsymbol{k}$ in Eq. (A8) are the same] and two dimensionless parameters (A9), Eu and β, are the same, then any two initially geometrically similar systems evolve in exactly the same way, despite possible enormous differences in the dimensional factors p^*, ρ^*, v^*, B^*, and L^*. Both systems may experience compression, recompression, shock formation, or transition to the turbulent state, and all this will be covered by the same set of equations (A7). This universality makes the Euler similarity so attractive for laboratory astrophysics.

The similarity is quite broad, imposing only two constraints, the constancy of Eu and β, on five parameters (p^*, ρ^*, v^*, B^*, and L^*) that define the system. In some cases, the number of constraints becomes even lower. For a purely hydrodynamical ($B = 0$), systems initially at rest [$\boldsymbol{v}(t = 0) = 0$] its further evolution remains similar for all geometrically similar initial states, without any constraints on p^*, ρ^*, and L^*.

It goes without saying that the set of Eqs. (A7) and (A8) contains all other, more specific similarities allowed by ideal hydrodynamics. In particular, if the system is spherically symmetric and a short-pulse point source of energy creates a highly heated zone in the otherwise cold gas, a self-similar Sedov-Taylor blast-wave solution is recovered (Tang and Wang, 2009). If the system contains (or develops) shear flows, it may generate fluid turbulence with the inertial cascading to smaller scales and the Kolmogorov-Obukhov similarity solution in the inertial range is established (Ryutov and Remington, 2003; Zhou, 2017a, 2017b). These are just two examples of many similarity solutions that can be found within the Euler similarity.

We emphasize that the Euler similarity is "tailored" to describe nonsteady-state processes (e.g., jet formation, development of Rayleigh-Taylor instabilities of accelerated interfaces, evolution of supernova remnants, interaction of shocks with clumps, etc). In this regard it is different from similarities designed to find characteristics of systems maintained in a quasisteady state, such as scaling for the viscous drag in Reynolds similarity, or plasma confinement scaling in fusion devices (Connor and Taylor, 1977).

Now we briefly discuss the role of dissipative processes: viscosity, thermal conductivity, magnetic diffusivity, and mutual diffusion of components in systems with variable composition. Those are characterized by the dimensionless parameters relating the rate of dissipation to the fluid advection rate. This yields familiar constraints on the Reynolds number Re, Peclet number Pe, magnetic Reynolds number Re_M, and mass Peclet number Pe_m:

$$\mathrm{Re} = L^* v/\nu, \qquad \mathrm{Pe} = L^* v/\chi,$$
$$\mathrm{Pe}_{\mathrm{mass}} = L^* v/D, \qquad \mathrm{Re}_{\mathrm{magn}} = L^* v/D_{\mathrm{magn}}, \tag{A10}$$

where L^* is a characteristic length scale, and ν, χ, D, and D_{magn} are, respectively, the kinematic viscosity, thermal diffusivity, mutual diffusion coefficient for a two-component system, and magnetic diffusivity. If all of these dimensionless numbers are much larger than unity, the role of the corresponding dissipation process is not important for the global scale motion. In astrophysical settings these conditions are normally satisfied to a very large degree due to a large scale of the astrophysical systems. In the laboratory, however, special care has to be taken to choose the experimental parameters that yield large values of these numbers although these are not necessarily the same as in real astrophysical systems. If they are large, then the motion on the global scales is not affected by dissipation.

One can expand the Euler similarity to include radiative cooling of the matter. In the case where radiative power per unit volume is a power law of p and ρ,

$$Q_{\mathrm{rad}} = A p^{\alpha_1} \rho^{\alpha_2}, \tag{A11}$$

one additional constraint has to be imposed (Ryutov *et al.*, 2001): a parameter $AL^* p^{*(\alpha_1 - 3/2)} \rho^{*(\alpha_2 - 1/2)}$ has to be kept constant between the two systems. In a simpler model, where the radiative loss is characterized by some cooling time τ, $Q_{\mathrm{rad}} = p/(\gamma - 1)\tau$, the similarity is observed if a parameter $(\tau/L)\sqrt{p^*/\rho^*}$ is invariant between the two systems.

Adding other dissipative processes to the set of Eqs. (A1)–(A4) leads to the appearance of additional constraints. A detailed analysis of these issues was presented by Falize, Michaut, and Bouquet (2009, 2011). Assuming that the radiative thermal diffusivity can be represented as a power-law function of p and ρ, one can find similarities for the diffusive radiative transport. For the situations where dynamic equations have to take into account too many dissipative processes (e.g., all four transport processes are important and have different dependences on the density and temperature), establishing a meaningful similarity may become impossible as the number of independent constraints exceeds the number of dimensional characteristics of the system, p^*, ρ^*, v^*, B^*, and L^*.

Scaled experiments play an important role in validation and verification of astrophysical codes used for a detailed description of astrophysical phenomena: the ensuing MHD flows are notoriously difficult for simulations. Provided the scalability can be established, numerical simulations of the laboratory experiment with controlled initial conditions (which one can vary on the shot-to-shot basis) and numerous diagnostics, establish a firm base for the code validation and verification. It is this area where considerable effort has been spent during the past decade (Calder *et al.*, 2002, 2004; Stehle *et al.*, 2009; Kuranz *et al.*, 2010, 2018).

In some cases, where a strongly reduced model is used, the similarity is easy to find. An example is scaling of the maximum energy of particles accelerated by the sausage instability of a current-carrying plasma column (Sec. VI.C). Applying such similarity to the set of laboratory experiments with varying input parameters (say, the current or geometrical dimensions) one can test the model itself, before attempting to apply it to astrophysics.

If one gets to collisionless regimes, then other types of similarities may show up that enter the problem via the Vlasov equations for the electron and ion distribution functions and Maxwell equations. An example of the corresponding similarity is that for the collisionless shocks formation in two counterstreaming plasmas (Ryutov *et al.*, 2012). This similarity covers both electrostatic and electromagnetic mechanisms. It allows also for scaling from hydrogen plasmas (as in astrophysical settings) to plasmas of heavier elements (such as carbon or beryllium) often used in the laboratory experiments because of the fabrication issues of the initial setup.

As a general rule one may say that the simpler the set of equations is (with a smaller number of parameters characterizing the system), the easier it is to find a similarity. It must, however, be verified that the same physics (the same set of equations) work for both laboratory and astrophysical systems. For example, if the radiation transport is negligibly small in the astrophysical system, the parameters of the laboratory experiments have to be chosen so as to make radiative transport negligible.

REFERENCES

Agra-Amboage, V., *et al.*, 2011, "Sub-arcsecond [Fe II] spectro-imaging of the DG Tauri jet Periodic bubbles and a dusty disk wind?," Astron. Astrophys. **532**, A59.

Aleksandrov, V. V., G. S. Volkov, E. V. Grabovski, A. N. Gritsuk, Ya. N. Laukhin, K. N. Mitrofanov, G. M. Oleinik, I. N. Frolov, and A. P. Shevel'ko, 2016, "Study of the formation, stability, and X-ray emission of the Z-pinch formed during implosion of fiber arrays at the Angara-5-1 facility," Plasma Phys. Rep. **42**, 1024.

Ampleford, D. J., A. Ciardi, S. V. Lebedev, S. N. Bland, S. C. Bott, J. P. Chittenden, G. N. Hall, A. Frank, and E. Blackman, 2007, "Jet Deflection by a Quasi-Steady-State Side Wind in the Laboratory," Astrophys. Space Sci. **307**, 29–34.

Ampleford, D. J., *et al.*, 2005, "Formation of working surfaces in radiatively cooled laboratory jets," Astrophys. Space Sci. **298**, 241–246.

Ampleford, D. J., *et al.*, 2008, "Supersonic radiatively cooled rotating flows and jets in the laboratory," Phys. Rev. Lett. **100**, 035001.

Ampleford, D. J., *et al.*, 2010, "Bow shocks in ablated plasma streams for nested wire array z-pinches: a laboratory astrophysics testbed for radiatively cooled shocks," Phys. Plasmas **17**, 056315.

Arnett, D., 1996, *Supernovae and Nucleosynthesis* (Princeton University Press, Princeton).

Arnett, D., 2000, "The relevance of HED lasers to astrophysics," Comptes Rendus de l'Academie des Sciences Serie IV, Physique Astrophysique, **1**, 767–771.

Bacciotti, F., R. Mundt, T. P. Ray, J. Eisloffel, J. Solf, and M. Camezind, 2000, "Hubble space telescope STIS spectroscopy of the optical outflow from DG Tauri: structure and kinematics on subarcsecond scales," Astrophys. J. **537**, L49.

Bacciotti, F., T. P. Ray, R. Mundt, J. Eisloffel, and J. Solf, 2002, "Hubble Space Telescope/STIS Spectroscopy of the Optical Outflow from DG Tauri: Indications for Rotation in the Initial Jet Channel," Astrophys. J. **576**, 222–231.

Bai, X.-N., 2014, "Hall-effect-controlled gas dynamics in protoplanetary disks. I. Wind solutions at the inner disk," Astrophys. J. **791**, 137.

Bailey, J. E., *et al.*, 2007, "Iron-plasma transmission measurements at temperatures above 150 eV," Phys. Rev. Lett. **99**, 265002.

Bailey, J. E., *et al.*, 2015, "A higher-than-predicted measurement of iron opacity at solar interior temperatures," Nature (London) **517**, 56.

Bakshaev, Yu. L., *et al.*, 2014, "Generation and anisotropy of neutron emission from a condensed Z-pinch," Plasma Phys. Rep. **40**, 437–450.

Balbus, S. A., 2011, "A turbulent matter," Nature (London) **470**, 475–476.

Balbus, S. A., and J. F. Hawley, 1991, "A powerful local shear instability in weakly magnetized disks. I—Linear analysis. II—Nonlinear evolution," Astrophys. J. **376**, 214.

Balbus, S. A., and P. Henri, 2008, "On the magnetic Prandtl number behavior of accretion disks," Astrophys. J. **674**, 408–414.

Bamba, A., R. Yamazaki, M. Ueno, and K. Koyama, 2003, "Small-scale structure of the SN 1006 shock with Chandra observations," Astrophys. J. **589**, 827.

Barenblatt, G. I., 1979, "Similarity, self-similarity, and intermediate asymptotics" (Consultants Bureau, New York/London).

Begelman, M. C., 1998, "Instability of Toroidal Magnetic Field in Jets and Plerions," Astrophys. J. **493**, 291.

Bellan, P. M., 2000, *Spheromaks* (Imperial College Press, London).

Bellan, P. M., 2018a, "Experiments and models of MHD jets and their relevance to astrophysics and solar physics," Phys. Plasmas **25**, 055601.

Bellan, P. M., 2018b, "Experiments relevant to astrophysical jets," J. Plasma Phys. **84**, 755840501.

Bellan, P. M., S. You, and S. C. Hsu, 2005, "Simulating astrophysical jets in laboratory experiments," Astrophys. Space Sci. **298**, 203.

Benford, G., 1978, "Current-carrying beams in astrophysics: models for double radio sources and jets," Mon. Not. R. Astron. Soc. **183**, 29–48.

Bennett, M. J., *et al.*, 2015, "Formation of radiatively cooled, supersonically rotating, plasma flows in Z-pinch experiments: Towards the development of an experimental platform to study accretion disk physics in the laboratory," High Energy Density Phys. **17**, 63.

Bland, S. N., *et al.*, 2005, "Effect of Radial-Electric-Field Polarity on Wire-Array Z-Pinch Dynamics," Phys. Rev. Lett. **95**, 135001.

Blondin, J. M., B. A. Fryxell, and A. Konigl, 1990, "The structure and evolution of radiatively cooling jets," Astrophys. J. **360**, 370–386.

Bocchi, M., B. Ummels, J. P. Chittenden, S. V. Lebedev, A. Frank, and E. G. Blackman, 2013, "Numerical simulations of z-pinch experiments to create supersonic differentially rotating plasma flows," Astrophys. J. **767**, 84.

Bosch-Ramon, V., and F. M. Rieger, 2012, "Exploring Particle Acceleration in Gamma-Ray Binaries," *Astroparticle, Particle, Space Physics and Detectors For Physics Applications—Proceedings of the 13th ICATPP Conference*, edited by Giani Simone *et al.* (World Scientific Publishing Co. Pte. Ltd., Singapore), pp. 219–225.

Braginski, S. I., 1965, "Transport processes in a plasma," in *Reviews of Plasma Physics*, edited by M. A. Leontovich (Consultants Bureau, New York), p. 205.

Branch, D., and J. C. Wheeler, 2017, *Supernova Explosions* (Springer, New York), Sec 9.5.

Bridgman, P. W., 1963, *Dimensional Analysis* (Yale University Press, New Haven).

Burdiak, G. C., *et al.*, 2013, "The production and evolution of multiple converging radiative shock waves in gas-filled cylindrical liner z-pinch experiments," High Energy Density Phys. **9**, 52.

Burdiak, G. C., *et al.*, 2014, "Radiative precursors driven by converging blast waves in noble gases," Phys. Plasmas **21**, 033302.

Burdiak, G. C., *et al.*, 2015, "Cylindrical liner Z-pinch experiments for fusion research and high-energy-density physics," J. Plasma Phys. **81**, 365810301.

Burdiak, G. C., *et al.*, 2017, "The structure of bow shocks formed by the interaction of pulsed-power driven magnetised plasma flows with conducting obstacles," Phys. Plasmas **24**, 072713.

Bott-Suzuki, S. C., *et al.*, 2015, "Investigation of radiative bow-shocks in magnetically accelerated plasma flows," Phys. Plasmas **22**, 052710.

Calder, A., *et al.*, 2002, "On validating an astrophysical simulation code," Astrophys. J. Suppl. Ser. **143**, 201.

Calder, A., *et al.*, 2004, "Validating astrophysical simulation codes," Comput. Sci. Eng. **6**, 10–20.

Campbell, E. M., 1991, "Recent results from the Nova program at LLNL," Laser Part. Beams **9**, 209.

Canto, J., and A. Raga, 1995, "The dynamics of a jet in a supersonic side wind," Mon. Not. R. Astron. Soc. **277**, 1120.

Canto, J., G. Tenorio-Tagle, and M. Rozyczka, 1988, "The formation of interstellar jets by the convergence of supersonic conical flows," Astron. Astrophys. **192**, 287.

Chittenden, J. P., S. V. Lebedev, C. A. Jennings, S. N. Bland, and A. Ciardi, 2004, "X-ray generation mechanisms in three-dimensional simulations of wire array Z-pinches," Plasma Phys. Controlled Fusion **46**, B457–B476.

Ciardi, A., D. J. Ampleford, S. V. Lebedev, and C. Stehle, 2008, "Curved Herbig-Haro jets: simulations and experiments," Astrophys. J. **678**, 968–973.

Ciardi, A., S. V. Lebedev, J. P. Chittenden, and S. N. Bland, 2002, "Modeling of supersonic jet formation in conical wire array Z-pinches," Laser Part. Beams **20**, 255.

Ciardi, A., Sergey V. Lebedev, Adam Frank, Francisco Suzuki-Vidal, Gareth N. Hall, Simon N. Bland, Adam Harvey-Thompson, Eric G. Blackman, and Max Camenzind, 2009, "Episodic magnetic bubbles and jets: astrophysical implications from laboratory experiments," Astrophys. J. **691**, L147–L150.

Ciardi, A., *et al.*, 2007, "The evolution of magnetic tower jets in the laboratory," Phys. Plasmas **14**, 056501.

Ciardi, Andrea, and Patrick Hennebelle, 2010, "Outflows and mass accretion in collapsing dense cores with misaligned rotation axis and magnetic field," Mon. Not. R. Astron. Soc. Lett. **409**, L39–L43.

Coffey, D., F. Bacciotti, J. Woitas, T. P. Ray, and J. Eisloffel, 2004, "Rotation of jets from young stars: new clues from the Hubble space telescope imaging spectrograph," Astrophys. J. **604**, 758.

Coffey, D., C. Dougados, S. Cabrit, J. Pety, and F. Bacciotti, 2015, "A Search for Consistent Jet and Disk Rotation Signatures in RY Tau," Astrophys. J. **804**, 2.

Comisso, L., M. Lingam, Y.-M. Huang, and A. Bhattacharjee, 2016, "General theory of the plasmoid instability," Phys. Plasmas **23**, 100702.

Connor, J. W., and J. B. Taylor, 1977, "Scaling laws for plasma confinement," Nucl. Fusion **17**, 1047.

Cuneo, M. E., *et al.*, 2006, "Compact single and nested tungsten-wire-array dynamics at 14–19 MA and applications to inertial confinement fusion," Phys. Plasmas **13**, 056318.

Dougados, C., S. Cabrit, C. Lavalley-Fouquet, and F. Menard, 2000, "T Tauri stars microjets resolved by adaptive optics," Astron. Astrophys. **357**, L61.

Drake, J. F., M. A. Shay, and M. Swisdak, 2008, "The Hall fields and fast magnetic reconnection," Phys. Plasmas **15**, 042306.

Drake, R. P., 1999, "Laboratory experiments to simulate the hydrodynamics of supernova remnants and supernovae," J. Geophys. Res. **104**, 14505–14515.

Drake, R. P., 2006, *High-Energy-Density Physics.* (Springer, Berlin/Heidelberg).

Dungey, J. W., 1958, *Cosmic Electrodynamics* (Cambridge University Press, London, UK).

Durst, F., 2007, *Fluid Mechanics* (Springer, New York), Chap. 7.

Falcon, R. E., G. A. Rochau, J. E. Bailey, T. A. Gomez, M. H. Montgomery, D. E. Winget, and T. Nagayama, 2015, "Laboratory Measurements of White Dwarf Photospheric Spectral Lines: Hβ," Astrophys. J. **806**, 214.

Falize, E., C. Michaut, and S. Bouquet, 2009, "Scaling laws for radiating fluids: the pillar of laboratory astrophysics," Astrophys. Space Sci. **322**, 107.

Falize, E., C. Michaut, and S. Bouquet, 2011, "Similarity properties and scaling laws of radiation hydrodynamic flows in laboratory astrophysics," Astrophys. J. **730**, 96.

Farley, D. R., K. G. Estabrook, S. G. Glendinning, S. H. Glenzer, B. A. Remington, K. Shigemori, J. M. Stone, R. J. Wallace, G. B. Zimmerman, and J. A. Harte, 1999, "Radiative Jet Experiments of Astrophysical Interest Using Intense Lasers," Phys. Rev. Lett. **83**, 1982.

Federrath, Christoph, *et al.*, 2014, "Modeling jet and outflow feedback during star cluster formation," Astrophys. J. **790**, 128.

Fermi, E., 1949, "On the Origin of the Cosmic Radiation," Phys. Rev. **75**, 1169.

Ferreira, J., C. Dougados, and S. Cabrit, 2006, "Which jet launching mechanism(s) in T Tauri stars?," Astron. Astrophys. **453**, 785–796.

Fiksel, G., W. Fox, A. Bhattacharjee, D. H. Barnak, P.-Y. Chang, K. Germaschewski, S. X. Hu, and P. M. Nilson, 2014, "Magnetic Reconnection between Colliding Magnetized Laser-Produced Plasma Plumes," Phys. Rev. Lett. **113**, 105003.

Fleischer, R. L., P. B. Price, and R. M. Walker, 1965, "Ion explosion spike mechanism for formation of charged-particle tracks in solids," J. Appl. Phys. **36**, 3645.

Foster, J. M., *et al.*, 2005, "High-energy-density laboratory astrophysics studies of jets and bow shocks," Astrophys. J. **634**, L77–L80.

Fox, W., G. Fiksel, A. Bhattacharjee, P.-Y. Chang, K. Germaschewski, S. X. Hu, and P. M. Nilson, 2013, "Filamentation instability of counterstreaming laser-driven plasmas," Phys. Rev. Lett. **111**, 225002.

Frank, A., B. Balick, and M. Livio, 1996, "A mechanism for the production of jets and ansae in planetary nebulae," Astrophys. J. **471**, L53.

Frank, A., *et al.*, 2014, "Jets and Outflows from Star to Cloud: Observations Confront Theory," in *Protostars and Planets VI*, edited by H. Beuther, R. S. Klessen, C. P. Dullemond, and T. Henning (University of Arizona Press, Tucson), pp. 451–474.

Furth, H. P., J. Killeen, and M. N. Rosenbluth, 1963, "Finite-Resistivity Instabilities of a Sheet Pinch," Phys. Fluids **6**, 459.

Ghavamian, P., P. F. Winkler, J. C. Raymond, and K. S. Long, 2002, "The optical spectrum of the SN 1006 supernova remnant revisited," Astrophys. J. **572**, 888.

Goodson, A. P., K. H. Böhm, and R. M. Winglee, 1999, "Jets from accreting magnetic young stellar objects. I. Comparison of observations and high-resolution simulation results," Astrophys. J. **524**, 142.

Goodson, A. P., and R. M. Winglee, 1999, "Jets from accreting magnetic young stellar objects. Ii. Mechanism physics," Astrophys. J. **524**, 159.

Goodson, A. P., R. M. Winglee, and K. H. Böhm, 1997, "Time-dependent accretion by magnetic young stellar objects as a launching mechanism for stellar jets," Astrophys. J. **489**, 199.

Gourdain, P.-A., I. C. Blesener, J. B. Greenly, D. A. Hammer, P. F. Knapp, B. R. Kusse, and P. C. Schrafel, 2010, "Initial experiments using radial foils on the Cornell Beam Research Accelerator pulsed power generator," Phys. Plasmas **17**, 012706.

Gourdain, P.-A., J. B. Greenly, D. A. Hammer, B. R. Kusse, S. A. Pikuz, C. E. Seyler, T. C. Shelkovenko, and P. F. Knapp, 2012, "Magnetohydrodynamic instabilities in radial foil configuration," Phys. Plasmas **19**, 022701.

Gourdain, P.-A., and C. E. Seyler, 2013, "Impact of the Hall Effect on High-Energy-Density Plasma Jets," Phys. Rev. Lett. **110**, 015002.

Gourdain, P.-A., and C. E. Seyler, 2014, "Modeling of strongly collimated jets produced by high energy density plasmas on COBRA," Plasma Phys. Controlled Fusion **56**, 035002.

Gregori, G., *et al.*, 2012, "Generation of scaled protogalactic seed magnetic fields in laser-produced shock waves," Nature (London) **481**, 480.

Haines, M., 1983, "Ion-beam formation in an $m = 0$ unstable z-pinch," Nucl. Instrum. Methods Phys. Res. **207**, 179–185.

Haines, M. G., 2011, "A review of the dense Z-pinch," Plasma Phys. Controlled Fusion **53**, 093001.

Hansen, E. C., A. Frank, P. Hartigan, and S. V. Lebedev, 2017, "The Shock Dynamics of Heterogeneous YSO Jets: 3-D Simulations Meet Multi-Epoch Observations," Astrophys. J. **837**, 143.

Hardee, P. E., 1982, "Helical and pinching instability of supersonic expanding jets in extragalactic radio sources," Astrophys. J. **257**, 509–526.

Hare, J. D., *et al.*, 2017a, "Anomalous Heating and Plasmoid Formation in a Driven Magnetic Reconnection Experiment," Phys. Rev. Lett. **118**, 085001.

Hare, J. D., *et al.*, 2017b, "Formation and Structure of a Current Sheet in Pulsed-Power Driven Magnetic Reconnection Experiments," Phys. Plasmas **24**, 102703.

Hare, J. D., *et al.*, 2018, "An experimental platform for pulsed-power driven magnetic reconnection," Phys. Plasmas **25**, 055703.

Hartigan, P., 2005, "Laboratory experiments of stellar jets from the perspective of an observer," Astrophys. Space Sci. **298**, 99.

Hartigan, P., A. Frank, J. M. Foster, B. H. Wilde, M. Douglas, P. A. Rosen, R. F. Coker, B. E. Blue, and J. F. Hansen, 2011, "Fluid dynamics of stellar jets in real time: third epoch Hubble Space Telescope images of HH 1, HH 34, and HH 47," Astrophys. J. **736**, 29.

Hartigan, P., *et al.*, 2009, "Laboratory experiments, numerical simulations, and astronomical observations of deflected supersonic jets: application to HH 110," Astrophys. J. **705**, 1073.

Hartigan, Patrick, Adam Frank, Peggy Varniére, and Eric G. Blackman, 2007, "Magnetic fields in stellar jets," Astrophys. J. **661**, 910–918.

Hartquist, T. W., and J. E. Dyson, 1996, "Flows in Clumpy Planetary Nebulae," Astrophys. Space Sci. **245**, 263–273.

Harvey-Thompson, A. J., S. V. Lebedev, S. N. Bland, J. P. Chittenden, G. N. Hall, A. Marocchino, F. Suzuki-Vidal, S. C. Bott, J. B. A. Palmer, and C. Ning, 2009, "Quantitative analysis of plasma ablation using inverse wire array Z pinches," Phys. Plasmas **16**, 022701.

Hillas, A. M., 1984, "The origin of ultra-high-energy cosmic rays," Annu. Rev. Astron. Astrophys. **22**, 425.

Hsu, S. C., and P. M. Bellan, 2002, "A laboratory plasma experiment for studying magnetic dynamics of accretion discs and jets," Mon. Not. R. Astron. Soc. **334**, 257–261.

Huarte-Espinosa, M., A. Frank, E. G. Blackman, A. Ciardi, P. Hartigan, S. V. Lebedev, and J. P. Chittenden, 2012, "On the structure and stability of magnetic tower jets," Astrophys. J. **757**, 66.

Huntington, C., *et al.*, 2015, "Observation of magnetic field generation via the Weibel instability in interpenetrating plasma flows," Nat. Phys. **11**, 173–176.

Jones, T. W., D. Ryu, and I. L. Tregillis, 1996, "The Magnetohydrodynamics of Supersonic Gas Clouds: MHD Cosmic Bullets and Wind-swept Clumps," Astrophys. J. **473**, 365.

Kadomtsev, B. B., 1965, "Plasma Stability" in *Reviews of Plasma Physics*, edited by M. A. Leontovich (Consultants Bureau, NY), Vol. 2, p. 153.

Kalantar, D. H., 1993, Ph.D. dissertation (Cornell University).

Kane, J. O., D. Arnett, B. A. Remington, S. G. Glendinning, J. Castor, R. Wallace, A. Rubenchik, and B. A. Fryxell, 1997, "Supernova-relevant hydrodynamic instability experiments on the Nova laser," Astrophys. J. Lett. **478**, L75–L78.

Käpylä, P. J., A. Brandenburg, M. J. Korpi, J. E. Snellman, and R. Narayan, 2010, "Angular momentum transport in convectively unstable shear flows," Astrophys. J. **719**, 67–76.

Kato, Y., M. R. Hayashi, and R. Matsumoto, 2004, "Formation of Semirelativistic Jets from Magnetospheres of Accreting Neutron Stars: Injection of Hot Bubbles into a Magnetic Tower," Astrophys. J. **600**, 338.

Klein, R. I., K. S. Budil, T. S. Perry, and D. R. Bach, 2003, "The interaction of supernova remnants with interstellar clouds: Experiments on the Nova laser," Astrophys. J. **583**, 245–259.

Klein, R. I., C. F. McKee, and P. Colella, 1994, "On the hydrodynamic interaction of shock waves with interstellar clouds. 1: Nonradiative shocks in small clouds," Astrophys. J. **420**, 213–236.

Klir, D., *et al.*, 2016, "Deuterium z-pinch as a powerful source of multi-MeV ions and neutrons for advanced applications," Phys. Plasmas **23**, 032702.

Knudson, M. D., M. P. Desjarlais, A. Becker, R. W. Lemke, K. R. Cochrane, M. E. Savage, D. E. Bliss, T. R. Mattsson, and R. Redmer, 2015, "Direct observation of an abrupt insulator-to-metal transition in dense liquid deuterium," Science **348**, 1455.

Knudson, M. D., D. L. Hanson, J. E. Bailey, C. A. Hall, J. R. Asay, and W. W. Anderson, 2001, "Equation of state measurements in liquid deuterium to 70 GPa," Phys. Rev. Lett. **87**, 225501.

Koepke, M. E., 2008, "Interrelated laboratory and space plasma experiments," Rev. Geophys. **46**, RG3001.

Königl, Arieh, 2010, "On the interpretation of the apparent existence of a preferred magnetic field in extragalactic jet sources," Mon. Not. R. Astron. Soc. Lett. **407**, L79–L83.

Kuranz, C., R. P. Drake, M. J. Grosskopf, B. Fryxell, A. Budde, J. F. Hansen, A. R. Miles, T. Plewa, N. Hearn, and J. Knauer, 2010, "Spike morphology in blast-wave-driven instability experiments," Phys. Plasmas **17**, 052709.

Kuranz, C. C., *et al.*, 2018, "How high energy fluxes may affect Rayleigh–Taylor instability growth in young supernova remnants," Nat. Commun. **9**, 1564.

Kurlsrud, R. M., R. Cen, J. P. Ostriker, and D. Ryut, 1997, "The protogalactic origin for cosmic magnetic fields," Astrophys. J. **480**, 481–491.

Landau, L. D., and E. M. Lifshitz, 1984, *Electrodynamics of Continuous Media* (Pergamon Press, New York).

Landau, L. D., and E. M. Lifshitz, 1987, *Fluid Mechanics* (Pergamon Press, New York).

Lebedev, S. V., R. Aliaga-Rossel, S. N. Bland, J. P. Chittenden, A. E. Dangor, M. G. Haines, and I. H. Mitchell, 1999, "The dynamics of wire array Z-pinch implosions," Phys. Plasmas **6**, 2016.

Lebedev, S. V., D. Ampleford, A. Ciardi, S. N. Bland, J. P. Chittenden, M. G. Haines, A. Frank, E. G. Blackman, and A. Cunningham, 2004, "Jet deflection via crosswinds: laboratory astrophysical studies," Astrophys. J. **616**, 988–997.

Lebedev, S. V., F. N. Beg, S. N. Bland, J. P. Chittenden, A. E. Dangor, M. G. Haines, K. H. Kwek, S. A. Pikuz, and T. A. Shelkovenko, 2001, "Effect of discrete wires on the implosion dynamics of wire array Z pinches," Phys. Plasmas **8**, 3734.

Lebedev, S. V., I. H. Mitchell, R. Aliaga-Rossel, S. N. Bland, J. P. Chittenden, A. E. Dangor, and M. G. Haines, 1998, "Azimuthal structure and global instability in the implosion phase of wire array Z-pinch experiments," Phys. Rev. Lett. **81**, 4152.

Lebedev, S. V., *et al.*, 2002, "Laboratory astrophysics and collimated stellar outflows: The production of radiatively cooled hypersonic plasma jets," Astrophys. J. **564**, 113.

Lebedev, S. V., *et al.*, 2005a, "Production of radiatively cooled hypersonic plasma jets and links to astrophysical jets," Plasma Phys. Controlled Fusion **47**, B465–B479.

Lebedev, S. V., *et al.*, 2005b, "Magnetic tower outflows from a radial wire array Z-pinch," Mon. Not. R. Astron. Soc. **361**, 97–108.

Lebedev, S. V., *et al.*, 2014, "The formation of reverse shocks in magnetized high energy density supersonic plasma flows," Phys. Plasmas **21**, 056305.

Lee, C.-F., P. T. P. Ho, Z. Y. Li, N. Hirano, Q. Zhang, and H. Shang, 2017, "A rotating protostellar jet launched from the innermost disk of HH 212," Nature Astronomy **1**, 0152.

Longair, M. S., 2011, *High Energy Astrophysics* (Cambridge University Press, Cambridge, UK).

Loureiro, N. F., and S. Boldyrev, 2017, "Role of Magnetic Reconnection in Magnetohydrodynamic Turbulence," Phys. Rev. Lett. **118**, 245101.

Loureiro, N. F., and D. A. Uzdensky, 2016, "Magnetic reconnection: from the Sweet-Parker model to stochastic plasmoid chains," Plasma Phys. Controlled Fusion **58**, 014021.

Lovelace, R. V. E., H. Li, A. V. Koldoba, G. V. Ustyugova, and M. M. Romanova, 2002, "Poynting jets from accretion disks," Astrophys. J. **572**, 445.

Lynden-Bell, D., 1996, "Magnetic collimation by accretion discs of quasars and stars," Mon. Not. R. Astron. Soc. **279**, 389.

Lynden-Bell, D., 2003, "On why discs generate magnetic towers and collimate jets," Mon. Not. R. Astron. Soc. **341**, 1360.

Madlener, D., S. Wolf, A. Dutrey, and S. Guilloteau, 2012, "The circumstellar disk of HH 30: Searching for signs of disk evolution with multi-wavelength modeling," Astron. Astrophys. **543**, A81.

Mandt, M. E., R. E. Denton, and J. F. Drake, 1994, "Transition to whistler mediated magnetic reconnection," Geophys. Res. Lett. **21**, 73.

Matzen, M. K., *et al.*, 1999, "Fast z-pinches as dense plasma, intense x-ray sources for plasma physics and fusion applications," Plasma Phys. Controlled Fusion **41**, A175–A184.

Mckee, C. F., and E. G. Zweibel, 1992, "On the virial-theorem for turbulent molecular clouds," Astrophys. J. **399**, 551–562.

McKinney, Jonathan C., and Roger D. Blandford, 2009, "Stability of relativistic jets from rotating, accreting black holes via fully three-dimensional magnetohydrodynamic simulations," Mon. Not. R. Astron. Soc. Lett. **394**, L126–L130.

Mereghetti, S., 2008, "The strongest cosmic magnets: soft gamma-ray repeaters and anomalous X-ray pulsars," Astron. Astrophys. Rev. **15**, 225.

Merritt, E. C., A. L. Moser, S. C. Hsu, Colin S. Adams, John P. Dunn, A. M. Holgado, and M. A. Gilmore, 2014, "Experimental evidence for collisional shock formation via two obliquely merging supersonic plasma jets," Phys. Plasmas **21**, 055703.

Metzger, B. D., B. Margalit, D. Kasen, and E. Quataert, 2015, "The diversity of transients from magnetar birth in core collapse supernovae," Mon. Not. R. Astron. Soc. **454**, 3311.

Moffatt, H. K., 1978, *Magnetic Field Generation in Electrically Conducting Fluids* (Cambridge University Press, Cambridge).

Moll, R., 2010, "Large jets from small-scale magnetic fields," Astron. Astrophys. **512**, A5.

Moser, A. L., and P. M. Bellan, 2012, "Magnetic reconnection from a multiscale instability cascade," Nature (London) **482**, 379.

Moser, A. L., and S. C. Hsu, 2015, "Experimental characterization of a transition from collisionless to collisional interaction between head-on-merging supersonic plasma jets," Phys. Plasmas **22**, 055707.

Nakamura, M., and D. L. Meier, 2004, "Poynting flux-dominated jets in decreasing density atmospheres. I. The nonrelativitic current-driven Kink instability and the formation of 'Wiggled' structures," Astrophys. J. **617**, 123–154.

Nakamura, Masanori, Hui Li, and Shengtai Li, 2007, "Stability properties of magnetic tower jets," Astrophys. J. **656**, 721–732.

Nicolaï, Ph., *et al.*, 2008, "Studies of supersonic, radiative plasma jet interaction with gases at the Prague Asterix Laser System facility," Phys. Plasmas **15**, 082701.

Nilson, P. M., *et al.*, 2006, "Magnetic Reconnection and Plasma Dynamics in Two-Beam Laser-Solid Interactions," Phys. Rev. Lett. **97**, 255001.

Norman, M. L., L. Smarr, K. H. A. Winkler, and M. D. Smith, 1982, "Structure and Dynamics of Supersonic Jets.," Astron. Astrophys. **113**, 285.

Ostriker, J. P., and C. F. McKee, 1988, "Astrophysical blast waves," Rev. Mod. Phys. **60**, 1.

Parker, E. N., 1957, "Sweet's mechanism for merging magnetic fields in conducting fluids," J. Geophys. Res. **62**, 509–520.

Pascoli, G., and L. Lahoche, 2010, "A Magnetohydrodynamic Model for the AGB Star: Preplanetary Nebula Symbiosis," Publ. Astron. Soc. Pac. **122**, 1334–1340.

Pikuz, S. A., T. A. Shelkovenko, and D. A. Hammer, 2015a, "X-Pinch. Part I," Plasma Phys. Rep. **41**, 291–342.

Pikuz, S. A., T. A. Shelkovenko, and D. A. Hammer, 2015b, "X-Pinch. Part II," Plasma Phys. Rep. **41**, 445–491.

Poludnenko, A. Y., K. K. Dannenberg, R. P. Drake, A. Frank, J. Knauer, D. D. Meyerhofer, M. Furnish, J. R. Asay, and S. Mitran, 2004, "A laboratory investigation of supersonic clumpy flows: experimental design and theoretical analysis," Astrophys. J. **604**, 213.

Prager, S. C., R. Rosner, H. T. Ji, and F. Cattaneo, 2010, *Research Opportunities in Plasma Astrophysics* (Princeton Plasma Physics Laboratory, Princeton, NJ) [http://www.pppl.gov/conferences/2010/WOPA/index.html].

Pringle, E. J., 1981, "Accretion Discs in Astrophysics," Annu. Rev. Astron. Astrophys. **19**, 137.

Pudritz, R. E., R. Quyed, C. Fendt, and A. Brandenburg, 2007, in *Protostars and Planets V*, edited by B. Reipurth, D. Jewitt, and K. Keil (University of Arizona Press, Tucson), p. 277.

Raga, A. C., E. M. de Gouveia Dal Pino, A. Noriega-Crespo, P. D. Mininni, and P. F. Velázquez, 2002, "Jet/cloud collision, 3D gasdynamic simulations of HH 110," Astron. Astrophys. **392**, 267–276.

Reipurth, B., and J. Bally, 2001, "Herbig-Haro flows: probes of early stellar evolution," Annu. Rev. Astron. Astrophys. **39**, 403–55.

Reipurth, B., S. Heathcote, J. Morse, P. Hartigan, and J. Bally, 2002, "Hubble Space Telescope images of the HH 34 jet and bow shock: structure and proper motions," Astron. J. **123**, 362.

Remington, B. A., R. P. Drake, and D. D. Ryutov, 2006, "Experimental astrophysics with high-power lasers and Z pinches," Rev. Mod. Phys. **78**, 755–807.

Remington, B. A., *et al.*, 1997, "Supernova hydrodynamics experiments on the Nova laser," Phys. Plasmas **4**, 1994.

Robey, H. F., *et al.*, 2001, "An experimental testbed for the study of hydrodynamic issues in supernovae," Phys. Plasmas **8**, 2446–2453.

Rochau, G. A., J. E. Bailey, R. E. Falcon, G. P. Loisel, T. Nagayama, R. C. Mancini, I. Hall, D. E. Winget, M. H. Montgomery, and D. A. Liedahl, 2014, "ZAPP: The Z Astrophysical Plasma Properties collaboration," Phys. Plasmas **21**, 056308.

Rochau, G. A., *et al.*, 2008, "Radiating shock measurements in the z-pinch dynamic hohlraum," Phys. Rev. Lett. **100**, 125004.

Rodriguez, R., *et al.*, 2012, "Determination and analysis of plasma parameters for simulations of radiative blast waves launched in clusters of xenon and krypton," Plasma Phys. Controlled Fusion **54**, 045012.

Romanova, M. M., A. Kulkarni, M. Long, R. V. E. Lovelace, J. V. Wick, G. V. Ustyugova, and A. V. Koldoba, 2006, Adv. Space Res. **38**, 2887.

Romanova, M. M., G. V. Ustyugova, A. V. Koldoba, and R. V. E. Lovelace, 2004, "Three-dimensional Simulations of Disk Accretion to an Inclined Dipole. II. Hot Spots and Variability," Astrophys. J. **610**, 920–932.

Rosenberg, M. J., C. K. Li, W. Fox, A. B. Zylstra, C. Stoeckl, F. H. Séguin, J. A. Frenje, and R. D. Petrasso, 2015, "Slowing of Magnetic Reconnection Concurrent with Weakening Plasma Inflows and Increasing Collisionality in Strongly Driven Laser-Plasma Experiments," Phys. Rev. Lett. **114**, 205004.

Rosner, R., and D. A. Hammer, 2010, *Basic Research Needs for High Energy Density Laboratory Physics* (US Department of Energy, Washington, DC), http://www.science.energy.gov/fes/news-and-resources/workshop-reports/.

Ross, J. S., *et al.*, 2012, "Characterizing counter-streaming interpenetrating plasmas relevant to astrophysical collisionless shocks," Phys. Plasmas **19**, 056501.

Ross, J. S., *et al.*, 2017, "Transition from Collisional to Collisionless Regimes in Interpenetrating Plasma Flows on the National Ignition Facility," Phys. Rev. Lett. **118**, 185003.

Ryutov, D. D., 2011, "Using Intense Lasers to Simulate Aspects of Accretion Discs and Outflows in Astrophysics," Astrophys. Space Sci. **336**, 21.

Ryutov, D. D., 2015, "Characterizing the Plasmas of Z-Pinches (Mini-Tutorial)," IEEE Trans. Plasma Sci. **43**, 2363.

Ryutov, D. D., M. S. Derzon, and M. K. Matzen, 2000, "The physics of fast Z pinches," Rev. Mod. Phys. **72**, 167.

Ryutov, D. D., R. P. Drake, J. Kane, E. Liang, B. A. Remington, and W. M. Wood-Vasey, 1999, "Similarity criteria for the laboratory simulation of supernova hydrodynamics," Astrophys. J. **518**, 821.

Ryutov, D. D., R. P. Drake, and B. A. Remington, 2000, "Criteria for scaled laboratory simulations of astrophysical MHD phenomena," Astrophys. J. Suppl. Ser. **127**, 465.

Ryutov, D. D., N. L. Kugland, H.-S. Park, C. Plechaty, B. A. Remington, and J. S. Ross, 2012, "Basic scalings for collisionless shock experiments," Plasma Phys. Controlled Fusion **54**, 105021.

Ryutov, D. D., and B. A. Remington, 2002, "Scaling astrophysical phenomena to high-energy-density laboratory experiments," Plasmas Phys. Controlled Fusion **44**, B407–B423.

Ryutov, D. D., and B. A. Remington, 2003, "A 'perfect' hydrodynamic similarity and effect of the Reynolds number on the global scale motion," Phys. Plasmas **10**, 2629–2632.

Ryutov, D. D., B. A. Remington, H. F. Robey, and R. P. Drake, 2001, "Magnetohydrodynamic scaling: from astrophysics to the laboratory," Phys. Plasmas **8**, 1804.

Sagdeev, R. Z., and C. F. Kennel, 1991, "Collisionless shock waves," Sci. Am. **264**, 106.

Savin, D. W., *et al.*, 2012, "The impact of recent advances in laboratory astrophysics on our understanding of the cosmos," Rep. Prog. Phys. **75**, 036901.

Sawai, H., K. Kotake, and S. Yamada, 2005, "Core-Collapse Supernovae with Nonuniform Magnetic Fields," Astrophys. J. **631**, 446–455.

Sedov, L., 1993, *Similarity and Dimensional Methods in Mechanics* (CRC Press, Boca Raton, FL), 10th ed.

Severnyi, A. B., 1959, "On the Appearance of Cosmics Rays in the Pinch Effect in Solar Flares," Sov. Astron. **3**, 887.

Shakura, N. I., and R. A. Sunyaev, 1973, "Black Holes in Binary Systems. Observational Appearance," Astron. Astrophys. **24**, 337.

Shelkovenko, T. A., S. A. Pikuz, C. L. Hoyt, A. D. Cahill, L. Atoyan, D. A. Hammer, I. N. Tilikin, A. R. Mingaleev, V. M. Romanova, and A. V. Agafonov, 2016, "A source of hard X-ray radiation based on hybrid X pinches," Phys. Plasmas **23**, 103303.

Shigemori, K., *et al.*, 2000, "Experiments on radiative collapse in laser-produced plasmas relevant to astrophysical jets," Phys. Rev. E **62**, 8838.

Shumlak, U., B. A. Nelson, and B. Balick, 2007, "Plasma Jet Studies via the Flow Z-Pinch," Astrophys. Space Sci. **307**, 41–45.

Shumlak, U., B. A. Nelson, E. L. Claveau, E. G. Forbes, R. P. Golingo, M. C. Hughes, R. J. Oberto, M. P. Ross, and T. R. Weber, 2017, "Increasing plasma parameters using sheared flow stabilization of a Z-pinch," Phys. Plasmas **24**, 055702.

Stehle, C., *et al.*, 2009, "Scaling stellar jets to the laboratory: The power of simulations," Laser Part. Beams **27**, 709.

Stone, J. M., and M. L. Norman, 1993a, "Numerical simulations of protostellar jets with nonequilibrium cooling.1. Method and 2-dimensional results," Astrophys. J. **413**, 198.

Stone, J. M., and M. L. Norman, 1993b, "Numerical simulations of protostellar jets with nonequilibrium cooling .2. Models of pulsed jets," Astrophys. J. **413**, 210.

Suttle, L. G., *et al.*, 2016, "Structure of a Magnetic Flux Annihilation Layer Formed by the Collision of Supersonic, Magnetized Plasma Flows," Phys. Rev. Lett. **116**, 225001.

Suttle, L. G., *et al.*, 2018, "Ion heating and magnetic flux pile-up in a magnetic reconnection experiment with super-Alfvénic plasma inflows," Phys. Plasmas **25**, 042108.

Suzuki-Vidal, F., S. V. Lebedev, S. Bland, G. N. Hall, A. J. Harvey-Thompson, J. P. Chittenden, A. Marocchin, S. C. Bott, J. B. A.

Palmer, and A. Ciardi, 2010, "Effect of Wire Diameter and Addition of an Axial Magnetic Field on the Dynamics of Radial Wire Array Z-Pinches," IEEE Trans. Plasma Sci. **38**, 581.

Suzuki-Vidal, F., *et al.*, 2009, "Formation of episodic magnetically driven radiatively cooled plasma jets in the laboratory," Astrophys. Space Sci. **322**, 19.

Suzuki-Vidal, F., *et al.*, 2011, "Experimental Studies of Magnetically Driven Plasma Jets," Astrophys. Space Sci. **336**, 41–46.

Suzuki-Vidal, F., *et al.*, 2012, "Interaction of a supersonic, radiatively cooled plasma jet with an ambient medium," Phys. Plasmas **19**, 022708.

Suzuki-Vidal, F., *et al.*, 2013a, "Interaction of radiatively cooled plasma jets with neutral gases for laboratory astrophysics studies," High Energy Density Phys. **9**, 141.

Suzuki-Vidal, F., *et al.*, 2013b, "Observation of energetic protons trapped in laboratory magnetic-tower jets," New J. Phys. **15**, 125008.

Suzuki-Vidal, F., *et al.*, 2015, "Bow shock fragmentation driven by a thermal instability in laboratory astrophysics experiments," Astrophys. J. **815**, 96.

Suzuki-Vidal, Francisco, *et al.*, 2010, "Generation of episodic magnetically driven plasma jets in a radial foil Z-pinch," Phys. Plasmas **17**, 112708.

Swadling, G. F., *et al.*, 2013, "Oblique shock structures formed during the ablation phase of aluminium wire array z- pinches," Phys. Plasmas **20**, 022705.

Szego, Karoly, *et al.*, 2015, *The Magnetodiscs and Aurorae of Giant Planets* (Springer, New York).

Takezaki, Taichi, Kazumasa Takahashi, Toru Sasaki, Takashi Kikuchi, and Nob Harada, 2016, "Accelerated ions from pulsed-power-driven fast plasma flow in perpendicular magnetic field," Phys. Plasmas **23**, 062904.

Tang, S., and Q. D. Wang, 2009, "Scalability of supernova remnant simulations," Mon. Not. R. Astron. Soc. **397**, 2106.

Tassis, K., and T. C. Mouschovias, 2004, "Ambipolar-diffusion timescale, star formation timescale, and the ages of molecular clouds: Is there a discrepancy?," Astrophys. J. **616**, 283.

Thompson, M. J., 2006, Ed., *An Introduction to Astrophysical Fluid Dynamics* (Imperial College Press, London), Chapters 8 and 9.

Trubnikov, B. A., 1990, "On the possible generation of cosmic rays in plasma pinches," Sov. Phys. Usp. **33**, 1061.

Trubnikov, B. A., 1992, "A new hypothesis of cosmic ray generation in plasma pinches," IEEE Trans. Plasma Sci. **20**, 898–904.

Uzdensky, D. A., and A. I. MacFadyen, 2006, "Stellar Explosions by magnetic towers," Astrophys. J. **647**, 1192–1212.

Uzdensky, D. A., and A. I. MacFadyen, 2007, "Magnetically dominated jets inside collapsing stars as a model for gamma-ray bursts and supernova explosions," Phys. Plasmas **14**, 056506.

Valenzuela, C., G. W. Collins IV, T. Zick, J. Narkis, I. Krasheninnikov, and F. N. Beg, 2015, "Counter-propagating plasma jet collision and shock formation on a compact current driver," High Energy Density Phys. **17**, 140–145.

Velikhov, E. P., 1959, "Stability of an ideally conducting liquid flowing between cylinders rotating in a magnetic field," Sov. Phys. JETP **36**, 995–998.

Vishniac, E. T., 1983, "The dynamic and gravitational instabilities of spherical shocks," Astrophys. J. **274**, 152–167.

Walters, W., 1998, *Fundamentals of Shaped Charges* (CMC Press, Baltimore, MD).

Wardle, M., 2004, "Star formation and the Hall effect," Astrophys. Space Sci. **292**, 317–323.

Wheeler, J. Craig, David L. Meier, and James R. Wilson, 2002, "Asymmetric Supernovae from Magnetocentrifugal Jets," Astrophys. J. **568**, 807.

White, M. C., *et al.*, 2014, "Multi-epoch subarcsecond [Fe II] spectroimaging of the DG Tau outflows with NIFS—II. On the nature of the bipolar outflow asymmetry," Mon. Not. R. Astron. Soc. **442**, 28–42.

Woosley, S., 2010, "Bright Supernovae From Magnetar Birth," Astrophys. J. Lett. **719**, L204.

Xu, Qiang, *et al.*, 2017, "The magnetically driven plasma jet produces a pressure of 33 GPa on PTS," Phys. Plasmas **24**, 010701.

Xu, Xiaojun, Yi Wan, Fengsi Wei, Xueshang Feng, Xiaohua Deng, Yonghui Ma, Meng Zhou, Ye Pang, and Hon-Cheng Wong, 2015, "Direct evidence for kinetic effects associated with solar wind reconnection," Sci. Rep. **5**, 8080.

Yamada, M., R. Kulsrud, and H. Ji, 2010, "Magnetic reconnection," Rev. Mod. Phys. **82**, 603–664.

Yamada, M., J. Yoo, and C. Myers, 2016, "Understanding the dynamics and energetics of magnetic reconnection in a laboratory plasma: Review of recent progress on selected fronts," Phys. Plasmas **23**, 055402.

Yamanaka, C., *et al.*, 1981, "Nd-doped phosphate glass laser systems for laser-fusion research," IEEE J. Quantum Electron. **17**, 1639.

Yirak, K., A. Frank, and A. J. Cunningham, 2010, "Self-convergence of Radiatively Cooling Clumps in the Interstellar Medium," Astrophys. J. **722**, 412–424.

You, S., J. von der Linden, E. S. Lavine, E. G. Carroll, A. Card, M. Quinley, and M. Azuara-Rosales, 2018, "The Mochi LabJet Experiment for Measurements of Canonical Helicity Injection in a Laboratory Astrophysical Jet," Astrophys. J. Suppl. Ser. **236**, 29.

Yusef-Zadeh, F., J. W. Hewitt, and W. Cotton, 2004, "A 20 centimeter survey of the galactic center region. i. detection of numerous linear filaments," Astrophys. J. Suppl. Ser. **155**, 421.

Yusef-Zadeh, F., M. Morris, and D. Chance, 1984, "Large, highly organized radio structures near the galactic-center," Nature (London) **310**, 557.

Zhai, X., and P. M. Bellan, 2016, "A hybrid Rayleigh-Taylor-current-driven coupled instability in a magnetohydrodynamically collimated cylindrical plasma with lateral gravity," Phys. Plasmas **23**, 032121.

Zhou, Ye, 2017a, "Rayleigh-Taylor and Richtmyer-Meshkov instability induced flow, turbulence, and mixing, I," Phys. Rep. **720–722**, 1–136.

Zhou, Ye, 2017b, "Rayleigh–Taylor and Richtmyer–Meshkov instability induced flow, turbulence, and mixing, II," Phys. Rep. **723–725**, 1–160.

Zier, J. C., *et al.*, 2012, "Magneto-Rayleigh-Taylor experiments on a MegaAmpere linear transformer driver," Phys. Plasmas **19**, 032701.

Zweibel, E. G., 2002, "Ambipolar drift in a turbulent medium," Astrophys. J. **567**, 962–970.

Zweibel, E. G., and M. Yamada, 2009, "Magnetic Reconnection in Astrophysical and Laboratory Plasmas," Annu. Rev. Astron. Astrophys. **47**, 291.